STUDIES ON MORPHODYNAMICS IN SHALLOW RIVERS WITH EFFECTS OF VEGETATION AND LARGE WOOD USING COMPUTATIONAL MODELS

By

Taeun Kang

Dissertation submitted for partial fulfillment of the requirements for the degree of Doctor of Philosophy

Examination Committee:

Prof. Yasuyuki Shimizu
Prof. Norihiro Izumi
Prof. Hideto Kon
Prof. Ichiro Kimura

Hokkaido University
Graduate School of Engineering
September 2018

DEDICATION

Then you will know the truth, and the truth will set you free.

John, 8:32

ABSTRACT

Many studies have been conducted to understand the effects of vegetation. However, the effects of vegetation (immobile vegetation type) in curved channels and the effects of large wood (L/D> 10, L: stem length, D: stem diameter; mobile vegetation type) in braiding channels are insufficiently studied. These vegetation types are important factors that can significantly alter bar formation, channel braiding and generation of thalweg in rivers. To expand our understanding of the interaction between bed morphology and both vegetation types, we investigated responses of bed morphology through a numerical model and a laboratory experiment.

In the first part, the study on effects of immobile vegetation, simulations were conducted using a two-dimensional, depth-averaged river flow and river morphology model to investigate the effect of vegetation growth and degree of flow discharge on a shallow meandering channel. To consider the effects of these factors, it was assumed that vegetation growth stage is changed by water flow and bed erosion. The non-uniformity of the vegetation growth was induced by the non-uniform and unsteady profile of the water depth due to the irregular shape of the bed elevation and the unsteady flow model reliant on hydrographs to evaluate three types of peak discharges: moderate flow, annual average maximum flow, and extreme flow. To compare the effects of non-uniformly growing vegetation, the change in channel patterns was quantified using the Active Braiding Index (ABI), which indicates the average number of channels with flowing water at a given cross-section, and the Bed Relief Index (BRI), which quantifies the degree of irregularity of the cross-sectional shape. Two types of erosion were identified: local erosion (due to increased flow velocity near a vegetation area) and global erosion (due to the discharge approaching peak and the large depth of the channel). This paper demonstrates that the growth of vegetation increases both the ABI and BRI when peak discharge is lower than the annual average discharge, whereas the growth of vegetation reduces the BRI when peak discharge is extreme. However, under extreme discharge, the ABI decreases because global erosion is dominant. The conclusions from this study help to deepen the understanding of the interactions between curved river channels and vegetation.

In the second part, the study on the effects of large wood deposition (mobile vegetation type), the large wood deposition patterns were analyzed in shallow flows, considering the effect of large wood root wad, by means of laboratory experiments and computer simulations. In this part, we first conducted a laboratory experiment to develop the large wood dynamic model. For the computations, we used the depth-averaged two-dimensional model Nays2DH on iRIC to simulate shallow flows. A newly developed large wood simulation model was combined with the shallow flow model. The laboratory

tests were performed by changing several hydraulic parameters: flow discharge, channel slope, and anisotropic bed friction. In shallow water with a depth similar to the diameter of large wood, the root wad decreased the draft for wood motion (the depth at which large wood contacts the river bed) by lifting the head of large wood. The experimental results showed that the large wood tends to move toward the side walls and deposit on the bed after passing an obstacle. Computational results reasonably showed that the proposed coupling model reproduced the fundamental and physical aspects of the phenomena.

Through the laboratory experiment, we attained reasonable reproducibility of the large wood dynamic model. Then we applied this model to practical experiments: Welber et al. (2013) and Bertoldi et al. (2014), which are based on observation data of the Tagliamento River, Italy. In this study, we modified Exner's equation to consider the bed morphology with large wood deposition, and we improved the detailed motion of large wood due to transition of projection area and anisotropic bed friction considering three angles: stemwise direction, streamwise direction and wood particle pass direction. From the simulation results, we quantitatively calculated the ABI, BRI, and mean values of the deposition position and deposition angle. We then analyzed the relationship between the bed morphology responses and the wood deposition patterns in terms of the root wad effect and input supply. The proposed model reproduces the prominent features of the flume experiment, indicating that the present numerical approach can clarify and predict the behavior of large pieces of wood in accordance with the bed morphology.

<This dissertation is a modified and revised form of the following original journals and proceedings>

Journal

1. Kang, T., Kimura, I and Shimizu, Y., Responses of bed morphology to hydrological events with effect of vegetation, Journal of Japan Society of Civil Engineers, Vol. 72, No. 2 (Applied Mechanics), Vol. 19, pp. I_601-I_612, 2016.
2. Kang, T., Kimura I and Shimizu Y., Studies on river flows at harp bends with a weak secondary flow using 2D and 3D CFD models. Journal of Japan Society of Civil Engineers, Ser., B1 (Hydraulic Engineering), Vol. 73, No. 4, pp. I_612-I_618, 2017.
3. Kang, T., Kimura I and Shimizu Y., Study on advection and deposition of driftwood affected by root in shallow flows, Journal of Japan Society of Civil Engineers, Ser., B1 (Hydraulic Engineering), Vol. 74, No. 4, pp. I_757-I_762, 2018.
4. Kang, T., Kimura I and Shimizu Y., Responses of bed morphology to vegetation growth and flood discharge at a sharp river bend, Water, Vol. 10, No. 2, pp. 223, 2018, doi:10.3390/w10020223.
5. Kang, T., Kimura I and Shimizu Y., Responses of bed morphology to large wood deposition using a computational hydrodynamic model, Japan Society of Civil Engineers, 2018. (Accepted)
6. Kang, T., Kimura I and Shimizu Y., Responses of bed morphology and driftwood deposition pattern in braided river: Computational hydrodynamic modeling. Earth Surface Processes and Landforms, 10th symposium on Symposium on River, Coastal and Estuarine Morphodynamics Special Issue. 2018. (Submitted with acceptance abstract from RCEM committees)

Conference

7. Kang, T., Kimura, I and Shimizu, Y., Responses of bed morphology to hydrological events with effect of vegetation, Journal of Japan Society of Civil Engineers, Vol. 72, No. 2 (Applied Mechanics), Vol. 19, pp. I_601-I_612, 2016.
8. Kang, T., Kimura I and Shimizu Y., Studies on river flows at harp bends with a weak secondary flow using 2D and 3D CFD models. Journal of Japan Society of Civil Engineers, Ser., B1 (Hydraulic Engineering), Vol. 73, No. 4, pp. I_612-I_618, 2017.

9. Kang, T., Kimura, I and Shimizu, Y., Study on the bed morphology depending on diverse flood event with vegetation effects in extreme shallow channel, Proceeding of 4th International Symposium of Shallow Flows, Eindhoven, Netherlands, June, 2017.
10. Kang, T., Kimura, I and Shimizu, Y., Studies on weak secondary flows in sharply curved bends using 3D CFD model, Proceeding of 10th Symposium on River, coastal and estuarine morphodynamics, Padova, Italy, pp. 203, Sep., 2017.
11. Kang, T., Kimura I and Shimizu Y., Study on advection and deposition of driftwood affected by root in shallow flows, Journal of Japan Society of Civil Engineers, Ser., B1 (Hydraulic Engineering), Vol. 74, No. 4, pp. I_757-I_762, 2018.

TABLE OF CONTENTS

LIST OF TABLES

LIST OF FIGURES

CHAPTER 1

INTRODUCTION

1.1 BACKGROUND AND CHALLENGES

River beds are changed by many factors such as river flow, ground water flow, sediment, vegetation, wildlife, and human beings. The main factors of bed morphology are river flow and sediment. Many researchers have studied such factors so that our understanding of river flow and sediment could be extensively enhanced. Through their contributions, we therefore could control river flow and sediment to mitigate flood events and could effectively manage water resources for human life. Vegetation also is essential factor in river morphodynamics. Vegetation continually affects the natural river system. In particular, some researchers have presented the argument that vegetation frequently affects channels through it reinforces a channel bank and reduces the number of active channels by inducing changes in sediment transport (Gran and Paola, 2001; Braudrick et al., 2009; Tal and Paola, 2010; Murray and Paola, 2003; Bennett et al., 2002). On the contrary, another researchers presented that the vegetation area alters channel beds to increase bed erosion. This bed erosion may cause scour erosion and the generation of a number of threads channels and thalweg (Coulthard, 2005; Kim et al., 2015; Kang et al., 2018). It also leads to changes in the pattern of bar formation and bank erosion.

Most researchers have considered immobile vegetation types to study on bed morphology and water flow with vegetation effect. Immobile vegetation mainly indicates static motion, which means that change in the vegetation area is mainly due to the colonization process. In viewing the flood scale in the short-term (one flood event), some researchers have considered vegetation without growth (e.g., Kim et al., 2015; Iwasaki et al., 2016a). In cases of long-term channel migration (more than one flood events), researchers have taken note of vegetation effects from time changes in the growing stage and the colonization process with decay (e.g., Crosato and Saleh, 2011; Kang et al., 2018). In particular, the vegetation growth and colonization play many diverse roles in river environments beyond simply disturbing the flood flow path, and growing vegetation affects different interactions between water flow and bed morphology (Kang et al., 2018).

In the past, torrential flow due to flood events has frequently occurred in the world due to climate change. This torrential flow, an unsteady flow, makes us face the limitation of our knowledge to predict flood events; torrential flow has been shown to cause enormous damage to humans. Thus, the importance in consideration of this unsteady flow has steadily increased. The vegetation effect by unsteady flow is

different from steady flow (Perucca et al., 2007; Ye et al., 2013). Accordingly, some researchers have pointed out that we should consider separately the rising stage and recession stage of unsteady flow because the bed morphology with each stage shows different bed changes; especially, the recession stage is important for mitigation of disasters such as bank erosion. Moreover, unsteady flow shows more complicated flow characteristics due to secondary flow of the first kind in a curved channel (**Figure 1.1(a)**). In this case, it is important to consider the sediment transport in the lateral direction because this secondary flow of the first kind is dominant due to the unbalanced pressure in the lateral direction induced by centrifugal force. In such conditions, if we consider the growing vegetation effect together with the curved channel, it should be one of the challenging tasks for researchers (for part 1).

Recently, along with immobile vegetation studies, studies related to mobile vegetation types also actively have increased. The study of large wood dynamics is familiar as well as immobile vegetation, and its importance increasingly has been noted in the field related to disaster mitigation due to debris flow and torrential flow with large wood.

Large wood ($l/d > 10$; l: length of wood, d: diameter of wood) is one mobile vegetation type. Rivers transport the large wood, and their deposition affects the river morphology by causing local scouring and the deposition of bed materials (**Figure 1.1(b)**). Such large wood enhances habitat diversity in the river environment and may initiate the formation of islands as a mid-channel bar in the bed morphology (Keller and Swanson, 1979; Nakamura and Swanson, 1993; Abbe and Montgomery, 1996; Gurnell and Petts, 2002; Swanson, 2003; van der Nat et al., 2003; Gurnell et al., 2005; Brooks et al., 2006; Cardenas, 2012). The deposition patterns of large wood can change in response to input processes, channel morphology, and hydrological parameters, including flood events (Montgomery, 2003). Past research has shown that the relative influence of these factors changes along the river system (Gurnell et al., 2002; Collins et al., 2012; Keller and Swanson, 1979; Gurnell et al., 2000a; Gurnell, 2013), resulting in distinct downstream trends in the manner of large wood accumulation (Keller and Swanson, 1979; Gurnell et al., 1995; Marcus et al., 2002; Comiti et al., 2006). The ratio of the log length to channel width is a key parameter in determining large wood deposition patterns (Gurnell and Sweet, 1998); these patterns are also influenced by parameters such as the drag force, water level, bed friction, and presence of obstacles.

Such large wood deposition is obviously associated with wood motion. The motion of large wood has been investigated by many researchers. Representatively, Braudrick and Grant (2000) and Braudrick et al. (2001) laid out the basic framework for describing large wood mobility and entrainment in rivers. Their work has allowed several researchers to undertake studies related to large wood transport dynamics (Haga et al., 2002; Bocchiola et al., 2002, 2006; Kramer and Wohl, 2017). These studies have successfully

predicted the relationship between wood characteristics (wood size, flow discharge, area of river basin) and the hydrodynamic and resistance forces, and have also extended the scope of transport systems.

The increase in experimental and observational research (e.g., Haga et al., 2002; Gurnell, 2003; Moulin and Piégay, 2004; Wohl and Goode, 2008; Seo and Nakamura, 2009; Cadol and Wohl, 2010; Curran, 2010; Iroume et al., 2010; Merten et al., 2010; Mao et al., 2013; Kramer and Wohl, 2017; Thévenet et al., 1998; Lassettre et al., 2008), as well as the enhanced importance of predicting and managing the stability of wood pieces and jams (Richmond and Fausch, 1995; Dixon and Sear, 2014; Davidson et al., 2015), has led to the active development of numerical models of large wood transport. For instance, hydrodynamic models of rivers have been combined with large wood transport models, such as the Iber-wood two-dimensional (2-D) hydrodynamic model (Ruiz-Villanueva et al., 2014a, 2014b, 2016) and the NaysCUBE (Kimura, 2012) three-dimensional (3-D) Reynolds-averaged Navier–Stokes (RANS) model (Kitazono et al., 2016; Kimura and Kitazono, 2017). Both of these models address wood transport using a Lagrangian method, whereby the water flow is coupled with the wood transport at every time step. The Iber-wood model considers the wood shape to be a simple cylinder. In contrast, the NaysCUBE large wood model applies a particle-based method to consider the impinging motion of large wood using a discrete element method (DEM). These studies have clarified the mechanism of large wood motion in deep water flows (where the water depth is greater than the wood diameter) and have reproduced the large wood motion well. However, these models overlook the bed morphology and large wood deposition factors such as the root-wad effect and anisotropic bed friction, although the effect of the wood on bed morphology is most relevant when being transported in shallow flows. Thus, clarifying such phenomena by coupling floating and deposition motions with bed morphology is crucial in enhancing our understanding of large wood behavior in rivers as well as the role of large wood floating advection on the permanent bed (for part 2).

To deal with two challenges in bed morphology with both types of vegetation (growing vegetation and large wood; immobile and mobile vegetation, respectively), these challenges should be independently approached in two parts. For the first challenge (immobile vegetation effect), bed morphology with vegetation effect should be studied based on a 2-D hydrodynamics model and observation data. In particular, it is necessary to review the previous studies associated with vegetation effect and to improve the previous model to consider both of vegetation growth and colonization in a curved channel with unsteady flow. For the second challenge (mobile vegetation effect), a model should be developed to study large wood dynamics. Thus, a laboratory experiment should be conducted to test the reproducibility of the

developed model, and then this model should be applied to practical experiments on the basis of observation data.

(a) vegetation area in the curved shallow channel, Korea (Kang, 2016)

(b) stored large wood due to shallow flow in the braiding channel, Italy (Google earth, 2018)

Figure 1.1 Vegetation and Large wood.

1.2 STUDY OBJECTIVES

This work is to investigate bed morphological phenomena with vegetation colonization and large wood deposition patterns. Observation data (for topography data of meandering channel), laboratory experiments (for large wood with root wad effect) and numerical simulations (for non-uniformly growing vegetation model and large wood dynamic model using two dimensional depth averaged model) were employed as methods.

The objective of the research is to provide a better understanding of morphological response to bed morphology with non-uniformly growing vegetation colonization and large wood dynamics in shallow river. To accomplish the overall aim, the following procedure was proposed:

Part 1 (Growing vegetation: immobile type vegetation)

1) Investigating responses of bed morphology (generation of threads channels, thalweg and point bar in curved channel under the unsteady flows) by vegetation with colonization and decay using 2D numerical model.

2) Assessing morphological response to a colonization of growing vegetation in curved channel by means of channel quantification (active braiding index and bed relief index).

Part 2 (Large wood: mobile type vegetation)

3) Developing 2D computational large wood dynamic model in consideration of anisotropic bed friction coefficient, root wad effect, critical draft for wood motion.

4) Examining large wood deposition motion with respect to interactions between channel slope and flow discharge using laboratory experiments and numerical simulations.

5) Analyzing responses of bed morphology with large wood deposition patterns by means of channel quantification (active braiding index and bed relief index) based on laboratory experiments and numerical simulations.

1.3 LAYOUT OF THIS DISSERTATION

Chapter 2: In this chapter, we conducted simulations using a two-dimensional, depth-averaged river flow and river morphology model to investigate the effect of vegetation growth and degree of flow discharge on a shallow meandering channel. To consider the effects of these factors, it was assumed that vegetation growth stage is changed by water flow and bed erosion. The non-uniformity of the vegetation

colonization by growth was induced by the non-uniform and unsteady profile of the water depth due to the irregular shape of the bed elevation and the unsteady flow model reliant on hydrographs to evaluate three types of peak discharges: moderate flow, annual average maximum flow, and extreme flow. To compare the effects of non-uniform growing vegetation, the change in channel patterns was quantified using the Active Braiding Index (ABI), which indicates the average number of channels with flowing water at a cross section and the Bed Relief Index (BRI), which quantifies the degree of irregularity of the cross-sectional shape. Two types of erosion were identified: local erosion (due to increased flow velocity near a vegetation area) and global erosion (due to the discharge approaching peak and the large depth of the channel). This chapter demonstrated that the growth of vegetation increases both the ABI and BRI when the peak discharge is lower than the annual average discharge, whereas the growth of vegetation reduces the BRI when the peak discharge is extreme. However, under extreme discharge, the ABI decreases because global erosion is dominant. The conclusions from this chapter help to deepen the understanding of the interactions between curved river channels and vegetation.

Chapter 3: This chapter developed a computational model for large wood deposition patterns in shallow flows considering the effect of root wad based on laboratory experiments. For the computations, we used the depth-averaged two-dimensional model, Nays2DH, on iRIC to simulate shallow flows. A newly developed large wood simulation model was combined with the shallow flow model. The laboratory tests were performed by changing several hydraulic parameters: discharge, channel slope, and anisotropic bed friction. In shallow water with a depth similar to the large wood diameter, the root effect draft for wood motion (the depth at which the large wood contacts the river bed) by lifting up the head of large wood. The experimental results showed two different patterns of motions: the large wood tends to move toward the side walls and deposit on the bed after passing an obstacle. In the experiment, the root wad of the large wood significantly affected the large wood motion. The computational results reasonably showed that the proposed coupling model reproduced the fundamental and physical aspects of the phenomena.

Chapter 4: This chapter develops a numerical model for simulating the hydrodynamics involved in the transport of large pieces of wood in a braided river considering the root wad effect and anisotropic bed friction. The newly developed numerical model can precisely simulate the behavior of large pieces of wood using a 2-D depth-averaged Eulerian flow model that calculates the water flow and bed morphology in generalized coordinates. A Lagrange-type wood transport model is developed and combined with the flow model, and the applicability of the combined model is determined through a comparison with experimental results. From the simulation results, we quantitatively calculate the

Active Braiding Index, Bed Relief Index, and mean values of wood deposition position, and deposition angle. We then analyze the relationship between the bed morphology responses and the wood deposition patterns in terms of the root wad effect and input supply. The proposed model reproduces the prominent features of the flume experiment, indicating that the present numerical approach can clarify and predict the behavior of large pieces of wood in accordance with the bed morphology.

Chapter 5: summarizes some conclusions withdrawn based on the results obtained and analyses done in the previous and gives some recommendations.

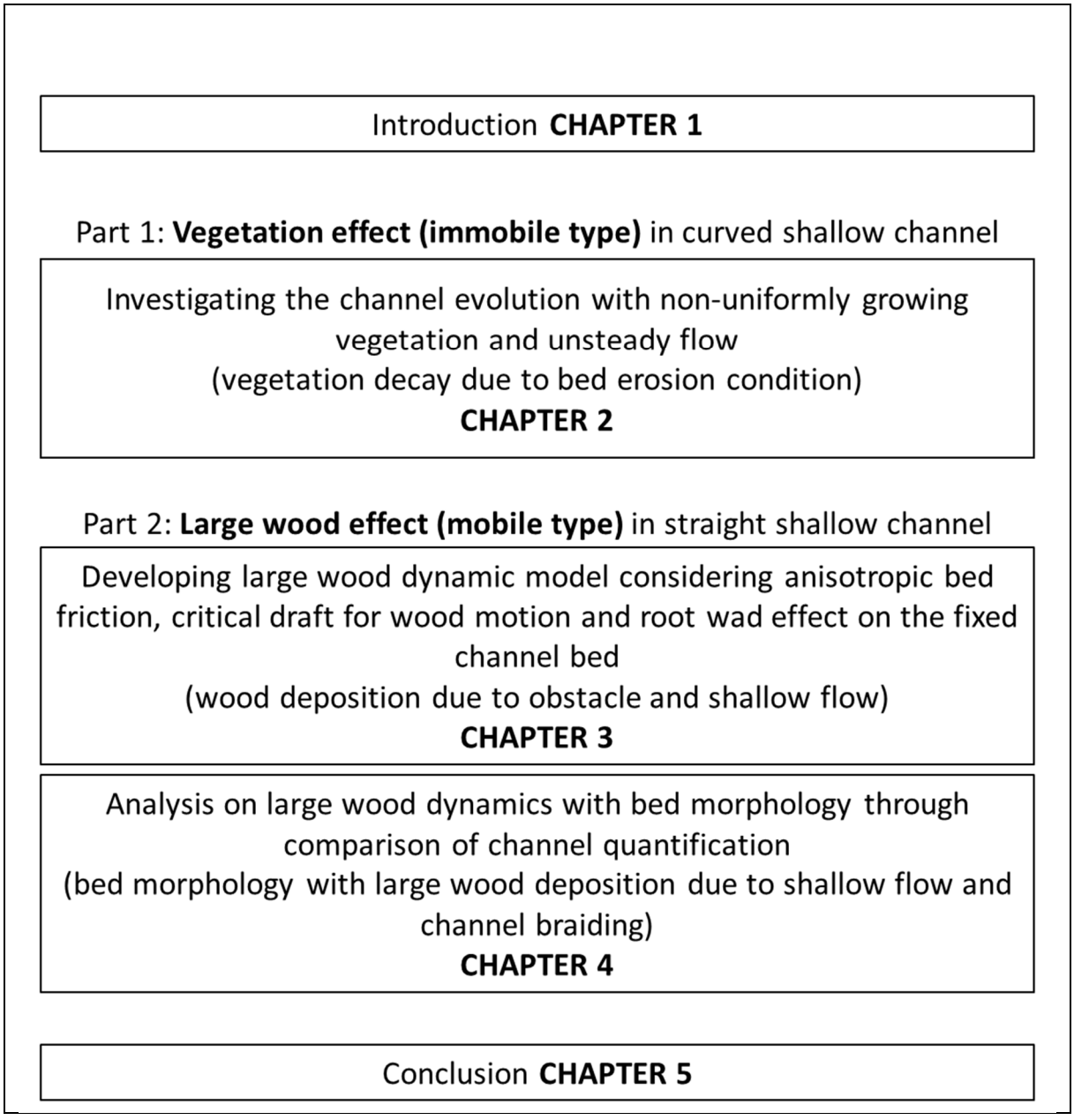

Figure 1.2 Outline for dissertation.

CHAPTER 2

RESPONSES OF BED MORPHOLOGY TO VEGETATION GROWTH AND FLOOD DISCHARGE AT A SHARP RIVER BEND: VEGETATION DECAY BY BED EROSION CONDITION

2.1 INTRODUCTION

Channel meander and vegetation growth are important factors influencing river morphology. Vegetation, in particular, is one of the main friction factors in shallow water flow. An area of vegetation alters river flow profiles by contributing to the increase in the water depth, decrease in the flow velocity, and increase in the shear stress near the vegetation, among other effects.

The growth of vegetation plays many diverse roles in river environments beyond simply disturbing the flood flow path. In particular, it influences sediment transport patterns. Several researchers have described the effects of vegetation on sediment transport, which contributes to the deformation of a riverbed (Williams and Wolman, 1984; Kaufmann et al., 1999; Camporeale et al., 2013). Several experiments (Gran and Paola, 2001; Braudrick et al., 2009; Jang and Shimizu, 2007; Tal and Paola, 2010; van Dijk et al., 2013), numerical simulations (Murray and Paola, 2003; Perucca et al., 2007; Iwasaki et al., 2016a), and field studies (Gurnell et al., 2006; Eekhout et al., 2014; Gurnell and Grabowski 2015) have shown that vegetation influences changes in channel flow and sediment transport.

Vegetation frequently affects the meandering of channels because vegetation reinforces the channel bank and reduces the number of active channels by inducing changes in sediment transport (Gran and Paola, 2001; Braudrick et al., 2009; Tal and Paola, 2010; Murray and Paola, 2003; Bennett et al., 2002). The relationship between vegetation and channel meander is therefore one of the most important factors in understanding the morphology of rivers (Jang and Shimizu, 2007; Hicken 1984; Smith 1976; Ikeda and Izumi, 1990; Millar and Qucik, 1993; Huang and Nanson, 1997; Millar, 2000; Bertoldi et al., 2011).

Until now, many field studies related to the interaction between vegetation effect and bed morphology have been actively carried out and these have provided useful data for a developing model of the vegetation effect in river alteration (Gurnell et al., 2006; Eekhout et al., 2014; Gurnell and

Grabowski, 2015; Abernethy and Rutherfurd, 2001). By employing such field survey data, conceptual models and statistical models that can consider diverse parameters such as flow discharge, sediment, and channel form have been proposed and the relationship among vegetation, water flow, and bed morphology have been presented for river bed change by riparian vegetation (Gurnell et al., 2006; Eekhout et al., 2014; Gurnell and Grabowski, 2015) investigated the importance of potential vegetation effect under the dynamics of bed morphology for river management and restoration. Abernethy and Rutherfurd (2001) studied the relation between the root characteristics and bank stabilization, and their results specifically show how the stability of the bank is affected by root profile.

In the past several years, numerical simulations and experiments have been conducted to investigate the effects of vegetation on open channel flows (Van De Wiel and Darby, 2004; Wu, 2005; Vargas-Luna et al., 2015). In particular, two-dimensional computations have been mainly used for such studies, because it is obvious that two-dimensional computations are more efficient than three-dimensional types if the grid spatial resolution in the horizontal plane are the same. For example, Tsujimoto (1999) surveyed river-bed deformation by means of a depth-averaged two-dimensional numerical model with added vegetation terms in the momentum and turbulent flow equations. The results demonstrate that the length of a vegetated free bar increases with exposure to an increased frequency of flood events. Crosato and Saleh (2011) simulated the long-term deformation of a river bed for varying degrees of vegetation density in the flood plain using a two-dimensional numerical model. It was found that a braided channel develops more readily when there is no vegetation; with sufficient density, vegetation contributes to the formation of a single thread channel.

Many researchers have conducted experiments to study the effects of vegetation on river channels through uniformly distributed seeding and growing (Gran and Paola, 2001; Braudrick et al., 2009; Jang and Shimizu, 2007; Tal and Paola, 2010; Perona et al., 2012). These studies demonstrate that a river bank with settled vegetation is sufficiently protected from erosion. Moreover, the number of thread channels decreases and the ratio of channel width to water depth decreases due to the effects of the vegetation, which contributes to the maintenance of the meandering channel. However, these previous studies considered only conditions of steady flow, which exclude, by definition, flood plain inundations, and only local erosion in the low channel is dominant. In Korea, vegetation growth is generally highly active during flood season (spring to summer), indicating that the effects of vegetation on the behavior of a river subject to flood conditions are critical considerations in understanding river morphology. Considering this research background, we investigated the effects of vegetation on river morphology using numerical methods. In most of the existing numerical investigations in the literature, the non-

uniform growth of vegetation in response to unsteady flow was not investigated as most studies assumed static vegetation. Consequently, most published research insufficiently explained changes to river bed morphology in response to the changes in vegetation growth that accompany flood events. Van Dijk et al. (2013) also pointed out that it is important to consider the distribution of vegetation because most experimental studies investigate small-scale bed morphology using uniform seed deposition; however, vegetation distribution is likely disrupted by flood events in the river channel.

Therefore, it is necessary to consider the process of non-uniform vegetation growth under conditions of unsteady flow, including growth, colonization, and decay states subject to flood events. Perucca et al. (2007) and Ye et al. (2013) suggested that the two main factors that influence the morphology of a meandering river with riparian vegetation are the degree of vegetation colonization and the alteration of flow discharge resulting from events such as floods, and droughts (Everitt, 1968; McKenney, 1995; Nanson and Beach, 1977; Rood and Mahoney, 1990; Robertson and Augspurger, 1999). However, the mechanism of bed morphology changes in response to the growth of vegetation remains unclear.

Indeed, the effect of vegetation in a meandering channel indicates a different behavioral phase than what is present in a straight channel. Garcia et al. (2012) emphasized that meandering channels have highly complex morphodynamical elements that control the ecosystems in the river basin. Therefore, it is important to include the presence of both vegetation and curved channel, because the vegetation and the meandering channel interact to maintain dynamic equilibrium.

The subject region of the present study is the Hoeryongpo, at the meander of the Nakdong river, Korea (Figure 2.1). Many researchers have shown interest in this area because of its diverse hydraulic geomorphic topography, which includes meandering channels, point bars, braided channels, and alternate bars. In particular, this area has a significantly developed point bar with a length of approximately 1 km, due to the sandy nature of the river bed. Owing to this variety of geomorphic features, this area is tremendously valuable as a subject of scientific research.

However, the Hoeryongpo meander is currently facing significant environmental changes due to shifts in flood patterns and a decrease in settlement caused because of the completion of the Yeong-ju Dam in 2016 approximately 40 km upstream of the meander. Moreover, the vegetated area has continually increased since 2009 due to severe drought, and these phenomena may result in significant changes to the bed and continue to expand the area of vegetation. If stable vegetation conditions continue to change sediment flow, accelerated by the sediment and flow reduction effects of the dam, the unique topographies present in the Hoeryongpo meander may be totally deformed and eventually disappear.

When facing these hydraulic issues, it is critical that the future effects of flood discharge and vegetation on changes in the river bed should be understood. Hence, this study investigated the effect of vegetation on river bed morphology. In particular, the growth and decay lifecycle of vegetation was quantified to account for non-uniform colonization depending on the water flow patterns. A two-dimensional numerical solver, Nays2DH (Shimizu et al., 2018) from iRIC software (2018), was used to calculate the water flow, and three different peak discharges, namely, moderate flood level, annual average maximum flood level, and extreme flood level (hereafter called moderate flood, annual average maximum flood and extreme flood or MF AMF and EF, respectively) were evaluated to analyze the interaction between bed morphology and growing vegetation depending on the degree of the river discharge.

(a) Sep. in 2003 year

(b) Sep. in 2004 year

(c) Feb. in 2005 year

(d) Nov. in 2013 year

(e) Nov. in 2015 year

(f) Apr. in 2016 year

Figure 2.1 Computational domain (dark brown area: vegetation area).

2.2 MATERIAL AND METHODS

2.2.1 Computational Conditions

The total length of the computational domain was set at 2376 m, the average channel width in this domain was 252 m, and the average bed slope was 0.0015. The Manning roughness coefficient was estimated as 0.016 s/m$^{1/3}$ from the average sediment diameter (d_m) of 1.49 mm, determined using the Manning-Strickler formula.

We used trial and error to obtain a suitable grid size. The shape of the grid was not rectangular because we adopted a curvilinear grid. The average length of the grid cell edges in the streamwise and lateral directions were 8 m and 5 m, respectively. We found that the simulation results obtained using the present grid resolution, such as flow patterns and bed changes, were almost identical to the results obtained using a finer grid resolution (mean sizes of cell edges were 4 m and 2.5 m in streamwise direction and lateral direction, respectively).

This study used three types of coordinate systems: 1) Cartesian coordinate, also called the x-y coordinates (used in the input data: topography and boundary condition, and bed relief index), 2) generalized curvilinear coordinate, also called the ξ-η coordinate (ξ and η axes fit to the grid lines), and 3) local streamline coordinates, also called the s-n coordinate (where s is streamline direction of the depth-averaged flow, and n is perpendicular to the s-axis). The computational time step was changeable by the Courant–Friedrich–Lewy (CFL) condition for reducing the CPU time (Courant et al., 1928).

The effect of vegetation was evaluated as a drag force on the momentum equations. The Ashida and Michiue's model (1972) was used to estimate the bedload flux, and a bed collapse model that considered the angle of repose was incorporated (Hasegawa, 1985). In addition, at the upstream boundary condition, the inlet velocity at each grid cell was locally calculated using the uniform flow equation based on the Manning formula, taking the bed profile and the local water depth into consideration. In detail, dummy boundary cells were provided outside the upstream end of the computational domain to set inlet boundary conditions. In addition, then the provisional flow velocities at the dummy boundary cells were calculated by the Manning formula. The slope for the Manning formula was assumed to be the average bed slope of the computational domain. Then, the provisional inflow discharge was calculated. The velocity was corrected by multiplying the provisional flow velocity by the ratio of the set discharge to the provisional discharge. Note that the transverse flow velocity at upstream boundary was always set zero. For the downstream boundary conditions, the water level was calculated through the Manning formula and gradient of the velocity component in the streamwise direction was set zero.

Table 2.1 presents the model parameters for computational condition. Each parameter is explained in subsequent sections.

Table 2.1 Main computation parameters

Parameter	Value	Model
The von Karman constant (κ)	0.4	Zero Equation
Mean diameter of bed load ($\boldsymbol{d_m}$)	1.49 mm	Sediment transport
Manning roughness coefficient ($\boldsymbol{n_m}$)	0.016 s/m$^{1/3}$	Sediment transport
Critical Shields number ($\boldsymbol{\tau_c}$)	0.0374	Sediment transport
The number of vegetation in unit area ($\boldsymbol{n_v}$)	95.34 EA	Vegetation
Coefficient of Drag force for vegetation ($\boldsymbol{C_D}$)	0.7	Vegetation
Maximum growth stage ($\boldsymbol{g_r}$)	0.21	Vegetation
Critical erosion depth of Vegetation decay (root length)	0.8 m	Vegetation
Angle of repose for bed material ($\boldsymbol{\theta_c}$)	30°	Slope failure

2.2.2 Hydrodynamic Model

This study used the Nays2DH (Shimizu et al., 2018) solver from iRIC. The Nays2DH solver employs the third order total variation diminishing-Monotonic upstream centered scheme for conservation laws (TVD-MUSCL) to solve the advection term and the central scheme for the Reynolds stress term, and a zero-equation type turbulence model based on the shallow flow equations was used.

Nays2DH solver relies on the depth-averaged momentum and continuity equations to calculate plane two-dimensional flow in a generalized curvilinear coordinate using **Equations** (2-1) - (2-11) as follows:

Continuity Equation:

$$\frac{\partial}{\partial t}\left(\frac{h}{J}\right)+\frac{\partial}{\partial \xi}\left(\frac{hU_\xi}{J}\right)+\frac{\partial}{\partial \eta}\left(\frac{hU_\eta}{J}\right)=0 \tag{2-1}$$

Momentum Equation:

$$\begin{aligned}&\frac{\partial U_\xi}{\partial t}+U_\xi\frac{\partial U_\xi}{\partial \xi}+U_\eta\frac{\partial U_\xi}{\partial \eta}+\alpha_1 U_\xi U_\xi+\alpha_2 U_\xi U_\eta+\alpha_3 U_\eta U_\eta\\&=-g\left[\left(\xi_x^2+\xi_y^2\right)\frac{\partial H}{\partial \xi}+\left(\xi_x\eta_x+\xi_y\eta_y\right)\frac{\partial H}{\partial \eta}\right]\\&-\left[C_f+g_r\left(\frac{1}{2}C_D a_v h_v\right)\right]\frac{U_\xi}{hJ}\sqrt{\left(\eta_y U_\xi-\xi_y U_\eta\right)^2+\left(-\eta_x U_\xi+\xi_x U_\xi\right)^2}+D_\xi\end{aligned} \tag{2-2}$$

$$\frac{\partial U_\eta}{\partial t} + U_\xi \frac{\partial U_\eta}{\partial \xi} + U_\eta \frac{\partial U_\eta}{\partial \eta} + \alpha_1 U_\xi U_\xi + \alpha_2 U_\xi U_\eta + \alpha_3 U_\eta U_\eta$$

$$= -g\left[\left(\eta_x \xi_x + \eta_y \xi_y\right)\frac{\partial H}{\partial \xi} + \left(\eta_x^2 + \eta_y^2\right)\frac{\partial H}{\partial \eta}\right] \tag{2-3}$$

$$-\left[C_f + g_r\left(\frac{1}{2} C_D a_v h_v\right)\right]\frac{U_\eta}{hJ}\sqrt{\left(\eta_y U_\xi - \xi_y U_\eta\right)^2 + \left(-\eta_x U_\xi + \xi_x U_\eta\right)^2} + D_\eta$$

where, x and y are the component of Cartesian coordinate, respectively; ξ and η are the component of curvilinear coordinate, respectively; t is time; u and v are depth-averaged velocity components in the x and y directions, respectively; g is gravitational acceleration; H is water surface level; h is water depth; h_v is minimum value of water depth and height of vegetation; D_ξ and D_η are turbulence viscosity terms in the direction of ξ and η, respectively; C_D is drag coefficient of vegetation (=0.7 as rigid cylinder shape); α_v is area of interception by vegetation per unit volume; g_r is vegetation growth stage; U_ξ and U_η are contra-variant components of velocity vectors in direction of ξ and η, respectively. Those vectors are transformed from **Equation** (2-5) and **Equation** (2-4), which are obtained by Chain rule for partial differentiations.

$$\xi_x = \frac{\partial \xi}{\partial x}, \quad \xi_y = \frac{\partial \xi}{\partial y}, \quad \eta_x = \frac{\partial \eta}{\partial x}, \quad \eta_y = \frac{\partial \eta}{\partial y},$$

$$x_\xi = \frac{\partial x}{\partial \xi}, \quad x_\eta = \frac{\partial x}{\partial \eta}, \quad y_\xi = \frac{\partial y}{\partial \xi}, \quad y_\eta = \frac{\partial y}{\partial \eta} \tag{2-4}$$

$$U_\xi = \xi_x u + \xi_y v, \quad U_\eta = \eta_x u + \eta_y v \tag{2-5}$$

where, ξ_x, ξ_y, η_x, η_y, x_ξ, x_η, y_ξ, y_η are the component of matrix between Cartesian coordinate and curvilinear coordinate. To transform between Cartesian coordinate and curvilinear coordinate, Jacobian of coordinate transformation (J) and parameters for the transformation of the velocity components (α_1 - α_6) are given as **Equations** (2-6)-(2-8).

$$J = \frac{1}{x_\xi y_\eta - x_\eta y_\xi} \tag{2-6}$$

$$\alpha_1 = \xi_x \frac{\partial^2 x}{\partial \xi^2} + \xi_y \frac{\partial^2 y}{\partial \xi^2}, \quad \alpha_2 = 2\left(\xi_x \frac{\partial^2 x}{\partial \xi \partial \eta} + \xi_y \frac{\partial^2 y}{\partial \xi \partial \eta}\right), \quad \alpha_3 = \xi_x \frac{\partial^2 x}{\partial \eta^2} + \xi_y \frac{\partial^2 y}{\partial \eta^2} \tag{2-7}$$

$$\alpha_4 = \eta_x \frac{\partial^2 x}{\partial \xi^2} + \eta_y \frac{\partial^2 y}{\partial \xi^2}, \quad \alpha_5 = 2\left(\eta_x \frac{\partial^2 x}{\partial \xi \partial \eta} + \eta_y \frac{\partial^2 y}{\partial \xi \partial \eta}\right), \quad \alpha_6 = \eta_x \frac{\partial^2 x}{\partial \eta^2} + \eta_y \frac{\partial^2 y}{\partial \eta^2} \tag{2-8}$$

The turbulent viscosity terms (D_ξ and D_η) can be expressed as follows:

$$D_\xi = \left(\xi_x \frac{\partial}{\partial \xi} + \eta_x \frac{\partial}{\partial \eta}\right)\left[\nu_t \left(\xi_x \frac{\partial U_\xi}{\partial \xi} + \eta_x \frac{\partial U_\xi}{\partial \eta}\right)\right] + \left(\xi_y \frac{\partial}{\partial \xi} + \eta_y \frac{\partial}{\partial \eta}\right)\left[\nu_t \left(\xi_y \frac{\partial U_\xi}{\partial \xi} + \eta_y \frac{\partial U_\xi}{\partial \eta}\right)\right] \tag{2-9}$$

$$D_\eta = \left(\xi_x \frac{\partial}{\partial \xi} + \eta_x \frac{\partial}{\partial \eta}\right)\left[\nu_t \left(\xi_x \frac{\partial U_\eta}{\partial \xi} + \eta_x \frac{\partial U_\eta}{\partial \eta}\right)\right] + \left(\xi_y \frac{\partial}{\partial \xi} + \eta_y \frac{\partial}{\partial \eta}\right)\left[\nu_t \left(\xi_y \frac{\partial U_\eta}{\partial \xi} + \eta_y \frac{\partial U_\eta}{\partial \eta}\right)\right] \tag{2-10}$$

where, ν_t is kinematic turbulent viscosity coefficient.

In **Equations** (2-2) and (2-3), C_f is the riverbed shear coefficient, which is calculated by **Equation** (2-11) with Manning roughness coefficient (n_m) as follows:

$$C_f = \frac{g n_m^2}{h^{1/3}} \tag{2-11}$$

To consider the turbulent flow, a zero-equation model is used for a wide and shallow water channel as given in **Equation** (2-12):

$$\nu_t = \frac{\kappa}{6} A_c u_* h + B_c \tag{2-12}$$

where, ν_t is the eddy viscosity coefficient; κ is the von Karman constant (0.4); u_* is the friction velocity; and A_c and B_c are user defined parameters for the eddy viscosity coefficient (the default values of A_c and B_c are 1 and 0, respectively).

2.2.3 Vegetation Model

The vegetation model has been developed by many researchers (Jang and Shimizu, 2007; Iwasaki et al., 2012; Shimizu et al., 2018; Shimizu et al., 2000) and it is mostly handles vegetation effect and bed morphology (Jang and Shimizu, 2007; Iwasaki et al., 2016a; Shimizu et al., 2000; Kim et al., 2012). In the Hoeryongpo meander, the reed (Phragmites), shown in **Figure 2.2(a)**, is the dominant species of the vegetation. The reed is a perennial plant with a primary growing time of approximately 3 months (**Figure 2.2(c)(d)**) (National Wetlands Center, 2018). Using **Figure 2.2(c)**, we calculated the average growth length as 2.38 m. Its root length is usually 80 cm according to measurement data in this field. As the current study considered only the flood event season, the average germination time of 6 days was neglected. In addition, vegetation shape was assumed to be a rigid cylinder, such that the drag coefficient of vegetation C_D was set to 0.7.

The vegetation growth increases the drag force on the channel flow. It inherently hebetates bed erosion and captures the sediment by reducing the flow velocity on the vegetation area; however, bed erosion around the vegetation area is activated by increasing the flow velocity (Gran and Paola, 2001;

Tal and Paola, 2010; Murray and Paola, 2003; Vargas-Luna, 2015). In addition, roots of vegetation stabilize their colony and suppress the motion of sediment by spatial root distribution, which enhances the tensile strength of the soil (Abernethy and Rutherfurd, 2001). However, in the present vegetation model, we assumed that vegetation is never buried and the effects of root in stabilizing the bed and reducing the sediment transport were neglected. Only the effect of the drag force on the flow was considered.

In this study, it is assumed that if the growth stage (g_r) is 0, 0% of the total possible vegetation drag force is applied to the flow calculation, indicating no vegetation is present in the cell, and while the growth stage (g_r) is 1, 100% of the vegetation drag force is applied to the flow calculation in each grid cell, indicating fully adult vegetation in the cell.

In the river basin, the growth of vegetation can be influenced by diverse factors, such as the duration of daylight, water flow, and temperature. This means that, for the purposes of this study, it is necessary to simplify the growth factor such that it directly relates the vegetation growth to water flow. We assumed that vegetation begins to grow during the flood season (June to August) and we set the simulation time as 450 h. The time of vegetation growth was 3 months, so that we assumed that the growth stage linearly increases and then reaches a value of 0.2 (**Figure 2.2(b)**) at the end of the simulation (450 h/3 month = 0.21). The decay process of the vegetation is assumed to change depending on the change in the river bed elevation with respect to the root length. As the length of a reed root is approximately 0.8 m (root growth is neglected), it was assumed that a river bed erosion more than 0.8 m eliminates the vegetation in that area, after which the growth stage (g_r) becomes 0.

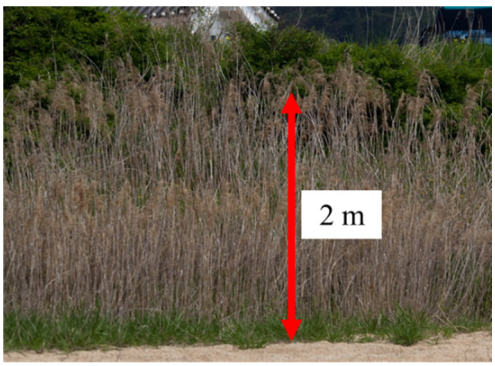

(a) sample of reed

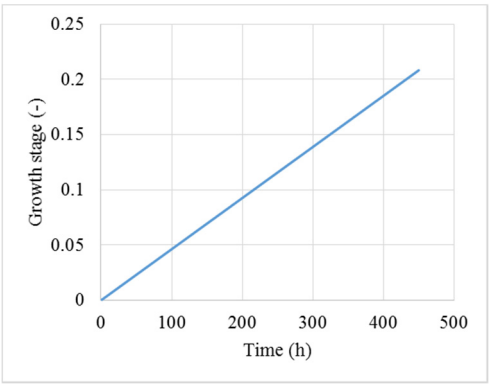

(b) growth stage (simulation time: 450h)

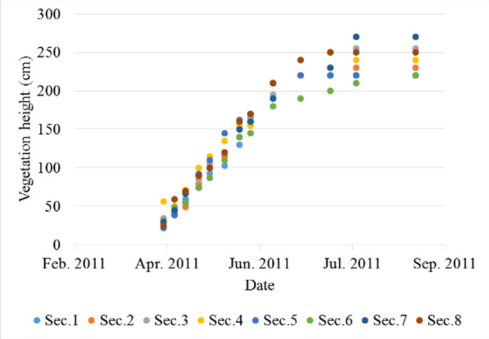

(c) measured vegetation growth

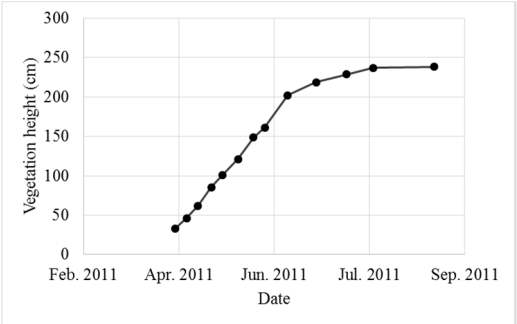

(d) averaged data from measured data

Figure 2.2 Vegetation species and growth stage. (Sec. is the measured section in Seokchon, Korea (National Wetlands Center, 2018))

The effect of vegetation density on the drag force of the channel was also considered. In this relationship, the vegetation density is defined as the area of flow interception by vegetation per unit volume (a_v), which is assigned to each computational cell as given by **Equation** (2-13) (Shimizu et al., 2000):

$$a_v = \frac{n_v D_v}{S_v^2} \tag{2-13}$$

where, n_v is the number of vegetation in the unit area, D_v is the average diameter of stalks or trunks, and S_v is the sampling grid width (S_v is 1 m in this study). According to the KICT report (2015), the average number (n_v/S_v^2) of overall vegetation in this study area in July is 95.34 EA/m^2. Moreover, since the subject vegetation consists primarily of reeds, D_v was assumed to be a small value of 0.01 m. As a result, the value of a_v in the study area was estimated as 1 m^{-1}.

(a) study area (2003 year)

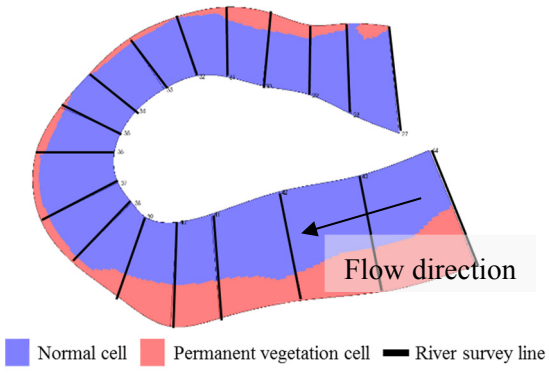

(b) permanent vegetation area (red color)

Figure 2.3 Permanent vegetation area.

In all simulations, two types of vegetation were used: a permanent type and a non-uniform growth type. The permanent vegetation area (shown in **Figure 2.3(b)**) was assumed as such because this vegetation area had been strongly established along the river bank for more than 10 years (see **Figure 2.3(a)**). Even after annual flood events, the vegetation in this area remained. Therefore, this vegetation area can be regarded as one of the constant factors of the topography. If vegetation in this area is neglected in the simulation, the main flow channel grows wider, the flow velocity shifts into a different phase, and the point bar fails to develop.

The non-uniform growth type of vegetation was also considered. This type of vegetation can grow non-uniformly depending on the water depth in its computational grid. If the water depth is greater than 0.1 m, the growth of vegetation is suspended. If the water depth again becomes smaller than 0.1 m, the growth of vegetation restarts from the current growth stage.

We used trial and error to adjust the initial condition of permanent vegetation. This study area has large point bar, which is main location for vegetation colonization, thus, it is important to reproduce this point bar for present study. Therefore, we considered four Cases to place the permanent vegetation area: around expected point bar area (Case 1), near the inner bank (Case 2), absent of permanent vegetation (Case 3) and near the outer bank and flood plain (Case 4). Case 1 can generate the point bar, but it is too artificial. Case 2 and Case 3 can generate the point bar near the inner bank, but another point bar is generated near the outer bank as much as point bar near the inner bank, so these Cases are inadequate to reproduce the survey data. Case 4 can generate the point bar well, thus, we employed its permanent vegetation area.

The initial growth stage (g_r) of permanent vegetation was determined to be 1, and its growth stage does not change. The initial growth stage of non-uniform vegetation growth (g_r) was 0, and its growth stage increases depending on the simulation time.

2.2.4 Non-Equilibrium Secondary Flow Model for Sediment Transport of Bed Load

In a curved channel, it is important to consider the sediment transport in the lateral direction because this secondary flow of the first kind is dominant due to the unbalanced pressure in the lateral direction induced by the centrifugal force. In general, the velocity near the bed is evaluated using the Engelund model (1974), and the direction of bedload transport is estimated using a secondary flow equilibrium model with Hasegawa's equation (1985). However, this equilibrium model does not consider the lag between the streamline curvature and the development of the secondary flow.

On the other hand, a non-equilibrium model (Onda et al., 2006; Kimura et al., 2007; Iwasaki et al., 2016a; Hosoda et al., 2001; Kalkwijk and De Vriend, 1980) can consider the lag between the secondary flow and the streamline curvature. The transport of the depth-averaged vorticity in the streamwise direction is calculated using the vorticity transport equation, which is associated with the secondary flow of the first kind. The equilibrium secondary flow model only considers the presence of secondary flow, whose strength is in proportion to the streamline curvature, neglecting the development and decay processes of the secondary flow due to change in the curvature of the streamline. The non-equilibrium model can consider the presence of lag, which means delay in the adjustment of the secondary flow to change in the streamline curvature. Hence, results obtained using the equilibrium and non-equilibrium secondary flow models exhibit different tendencies, especially in a sharp meandering channel such as this study area. Therefore, we employed a non-equilibrium model with following Equations:

First, equilibrium secondary flow model in the local streamline coordinates (called *s*-*n* coordinate) of the depth averaged flow field is expressed as follows:

$$u_n^b = u_s^b N \frac{h}{r} \tag{2-14}$$

$$u_s = u\cos\theta_s + v\sin\theta_s \,,\quad u_n = -u\sin\theta_s + v\cos\theta_s \tag{2-15}$$

where s and n are the component of streamwise and transverse direction in the *s*-*n* coordinate, respectively; u_s^b and u_n^b : streamwise and transverse and flow velocity near the bed in the *s*-*n* coordinate, respectively; u and v are x and y direction for flow velocity in Cartesian coordinate, respectively; u_s and u_n are streamwise and transverse direction for flow velocity in *s*-*n* coordinate, respectively; h is water depth; θ_s is angle between streamwise flow vector in *s*-*n* coordinate and *x*-axis of Cartesian coordinate; N is the coefficient associated with the secondary flow velocity profile in the depthwise direction. N is commonly set at 7 (Engelund, 1974). The local streamline curvature of the depth-averaged flow filed ' r ' is calculated as **Equation** (2-16) (Jang and Shimizu, 2005):

$$\frac{1}{r} = \frac{1}{V^3}\left[u\left(u\frac{\partial v}{\partial x} - v\frac{\partial u}{\partial x}\right) + v\left(u\frac{\partial v}{\partial y} - v\frac{\partial u}{\partial y}\right)\right] \tag{2-16}$$

where, V is the absolute flow velocity ($\sqrt{u^2+v^2}$).

The depth averaged vorticity equation for the streamwise direction (*s*-axis in *s*-*n* coordinate) should be employed into the model as **Equation** (2-17), to consider the non-equilibrium secondary flow (Hosoda et al., 2001; Onda et al., 2006; Kimura et al., 2007; Iwasaki et al., 2016b). It is defined that the

streamwise and transverse components of the velocity profile in the depthwise direction as **Equation** (2-18).

$$\frac{\partial}{\partial t}\left(u_n^s - u_n^b\right) + \frac{\partial}{\partial x}\left(u^s u_n^s - u^b u_n^b\right) + \frac{\partial}{\partial y}\left(v^s u_n^s - v^b u_n^b\right) + \frac{1}{r}\left(u_s^s u_s^s - u_s^n u_s^n\right) = \frac{\partial}{\partial z}\left(\nu_t \frac{\partial u_n^s}{\partial z}\right) - \frac{\partial}{\partial z}\left(\nu_t \frac{\partial u_n^b}{\partial z}\right) \tag{2-17}$$

$$\bar{u}_s(\psi) = \bar{V} f_s(\psi),\ \bar{u}_n(\psi) = \bar{A}_n f_n(\psi),\ \psi = \frac{z}{h} \tag{2-18}$$

where, the superscripts *s* and *b* denote values at the water surface and bed surface, respectively; $\bar{u}_s$ and $\bar{u}_n$ are depth averaged velocity of direction of streamwise and transverse, respectively; *z* is defined as the depthwise coordinate; A_n is the intensity of secondary flow induced by streamline curvature (r); $\bar{A}_n$ and $\bar{V}$ are mean value of A_n and V in depthwise direction, respectively; f_s and f_n are functions of the depthwise coordinate that describing the distribution of the streamwise and transverse velocity components, respectively; By applying the depthwise profile functions derived by Engelund (1974) to **Equation** (2-16), **Equation** (2-18) can be written as **Equation** (2-19).

$$\begin{aligned}\frac{\partial}{\partial t}\left(\lambda_{an} - A_n\right) + \frac{\partial}{\partial x}\left(u^s u_n^s - u^b u_n^b\right) + \frac{\partial}{\partial y}\left(v^s u_n^s - v^b u_n^b\right) + \frac{1}{r}\left(u_s^s u_s^s - u_s^n u_s^n\right) \\ = A_n \frac{V}{C_{s1}^3 h}\left(C_s^2 + \frac{7}{12}C_s + \frac{1}{12}\right)\end{aligned} \tag{2-19}$$

in **Equation** (2-19), the velocity vectors u_s^b, u_s^s, u_n^s, u_n^n in *s*-*n* coordinate are defined as **Equation** (2-20).

$$\begin{aligned}u_s^b = V\frac{C_s}{C_{s1}},\quad u_s^s = V\frac{C_s + 0.5}{C_{s1}},\quad u_n^b = A_n \frac{C_s}{\alpha^2 C_{s1}^2}\left(\frac{2}{45}C_s + \frac{4}{315}\right), \\ u_n^s = -A_n \frac{C_s}{\alpha^2 C_{s1}^2}\left(\frac{1}{180}C_s^2 + \frac{1}{56}C_s + \frac{4}{504}\right)\end{aligned} \tag{2-20}$$

$$\lambda_{an} = -\frac{1}{\alpha C_{s1}^3}\frac{V}{u_*}\left(\frac{1}{12}C_s^2 + \frac{11}{360}C_s + \frac{1}{504}\right),\ C_{s1} = \alpha\frac{V}{\tilde{u}_*},\ C_s = C_{s1} - \frac{1}{3},\ \alpha = \frac{\kappa}{6} \tag{2-21}$$

where, u_s^s and u_n^s are streamwise and transverse components for flow velocity at the water surface in the *s*-*n* coordinate, respectively; u_* is the friction velocity; κ is the von Kármán constant. **Equation** (2-21) regards the transverse flow velocity near the bed and it should be in accordance with **Equation** (2-16), so that the **Equations** (2-16) and (2-21) are able to be transformed into **Equation** (2-22), as follows:

$$u_s^b N\frac{h}{r} = A_n \frac{u_s^b}{V}\frac{1}{\alpha^2 C_{s1}}\left(\frac{2}{45}C_s + \frac{4}{315}\right) \tag{2-22}$$

where, the intensity of secondary flow A_n is assumed that if a curved channel has the equilibrium state of a flow under the uniform curvature, **Equation** (2-22) can be transformed as following:

$$A_n = V\frac{h}{r} \tag{2-23}$$

Therefore, the **Equation** (2-22) is able to be applied into Equation (2-23) as follows:

$$N = \frac{1}{\alpha^2 C_{s1}}\left(\frac{2}{45}C_s + \frac{4}{315}\right) \tag{2-24}$$

Consequently, the coefficient N is determined from the depthwise profile of secondary flow, and it can be affected by the velocity coefficient near the bed. If the value of α is 0.077. Using non-equilibrium secondary flow model, the sediment transport is calculated considering lag between curvature of stream lines and the development of the secondary flow.

2.2.5 Sediment Transport Model

To calculate the bed level change and the sediment transport of the bedload considering non-equilibrium secondary flow model, we used the Ashida and Michiue formula (1972) and the Exner equation to calculate the critical Shields number τ_c (=0.0374 in this study area), and we used the Iwagaki equation (1956) to calculate the Shields number τ as shown in follows:

$$\frac{\partial z_b}{\partial t} + \frac{1}{1-\lambda_p}\left[\frac{\partial q_{bx}}{\partial x} + \frac{\partial q_{by}}{\partial y}\right] = 0 \tag{2-25}$$

$$q_{bs} = 17\tau_c^{3/2}\left(1-\frac{\tau_c}{\tau}\right)\left(1-\sqrt{\frac{\tau_c}{\tau}}\right)\sqrt{s_g g d_m^3}\,,\ q_{bn} = q_{bs}\left[\frac{u_n^b}{V} - a_q\left(\frac{\tau_c}{\tau}\right)^{\gamma_q}\frac{\partial z_b}{\partial n}\right] \tag{2-26}$$

$$q_{bx} = q_{bs}\cos\theta_s - q_{bn}\sin\theta_s\,,\ q_{by} = q_{bs}\sin\theta_s + q_{bn}\cos\theta_s \tag{2-27}$$

Note that **Equation** (2-25) is in Cartesian coordinate and **Equations** (2-26) are in *s-n* coordinate. **Equation** (2-27) indicates transformation between Cartesian coordinate and *s-n* coordinate. Where, q_{bs} and q_{bn} are sediment discharge flux of streamwise and transverse direction in *s-n* coordinate, respectively; q_{bx} and q_{by} are sediment discharge flux of x and y direction in Cartesian coordinate, respectively; a_q and γ_q are model constants; z_b is bed elevation; n is the component of *s-n* coordinate; τ is Shields number; τ_c is critical Shields number; λ_p is the porosity of the river bed; s_g is specific gravity of sediment ($\approx$1.65); d_m is mean diameter the sediment particle; g is gravitational acceleration;

u_n^b is the flow velocity near the bed of transverse direction in *s*-*n* coordinate; V is depth-averaged absolute flow velocity in Cartesian coordinate.

2.2.6 Slope Failure Model

A slope failure model was employed in this study, which is consistent with several existing research studies (Jang and Shimizu, 2005; Jang and Shimizu, 2007; Iwasaki et al., 2012; Iwasaki et al., 2016a). In the present model, slope failure was considered at each two adjacent grid cells. If the bed slope at two adjacent cells exceed the angle of repose, sand from the higher cell is moved to the lower cell to satisfy the slope, just as the angle of repose. This adjustment is applied at the entire computational domain. This sweep is repeated until all bed slopes at the two adjacent cells become smaller than the angle of repose. In this process, the total volume of bed material is conserved. In this study, the angle of repose is 30° because almost the entire riverbed consists of sand, which has an angle of repose (θ_c) of approximately 30°. Slope failure model is as follows:

$$\Delta\zeta_0 = L(\tan\theta - \tan\theta_c)(1+\frac{A_0}{A_1})^{-1} \quad \Delta\zeta_1 = L(\tan\theta - \tan\theta_c)(1+\frac{A_1}{A_0})^{-1} \qquad (2\text{-}28)$$

where, θ is the current bed slope; φ is the angle of repose; L is the grid cell width; ζ_0 and ζ_1 are the bed elevations at two adjacent cells; $\Delta\zeta_0$ and $\Delta\zeta_1$ are the bank and bed elevation changes, respectively; and A_0 and A_1 are the width of two adjacent cells.

2.2.7 Hydrograph Characteristic Shape

To account for the diverse conditions of a flood event, a hydrograph characteristic shape, which can reflect a typical hydrograph for this location, is required. The observed river discharge data consists of several types of hydrographs, such as annual average maximum flood discharge, extremely big discharge, and moderate scale flood discharge. It is, therefore, difficult to select a typical hydrograph among such diverse observation data. Moreover, we were unable to clarify the starting time and ending time in each flood event because the flood event can consecutively occur during the flood season. Thus, a simplified hydrograph characteristic shape can be assumed to evaluate the growing vegetation effect under the same hydrograph shape.

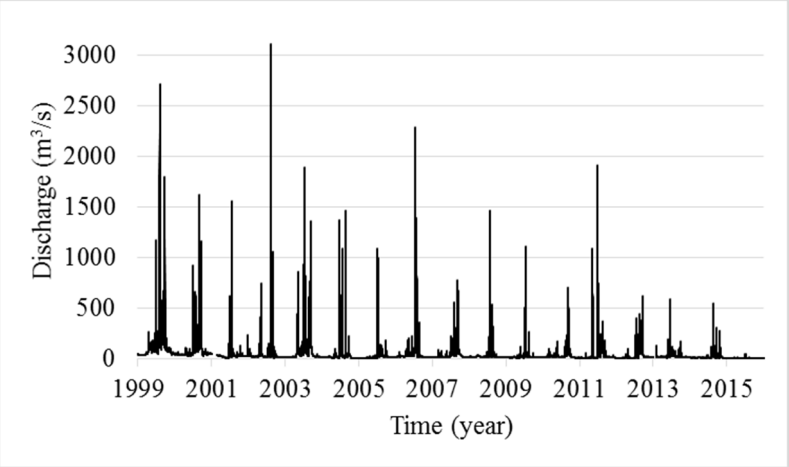

Figure 2.4 Measured discharge. (Water Resources Management Information System, http://www.wamis.go.kr/, 2018)

The process of generating the hydrograph characteristic shape is as follows:

1. Flood events, with the annual maximum peak, were selected from 15 years of measurement data (see **Figure 2**.**4**), except for the 2015, as the hydrograph for this year shows less than half of the annual averaged maximum discharge (690 m^3/s) of the other years. Thus, a total of 14 hydrographs were extracted from 15 years' data;
2. Each hydrograph was normalized using each peak discharge and then trimmed at the inflection points;
3. And then, the hydrograph characteristic shape was calculated by ensemble averaging with all of 14 normalized hydrographs. Before taking ensemble averaging, the start times of all hydrographs were adjusted so that the times to peaks become the same. We also assumed that the discharge at the start and the end of the hydrograph is the total averaged discharge for 15 years. As a result, the flood duration of the hydrograph characteristic shape becomes 150 h.

Using this hydrograph characteristic shape, hydrographs with arbitral peak discharges can be obtained easily through calculation (hydrograph characteristic shape × peak discharge) as shown in **Figure 2.5**.

We should check whether the created hydrograph with the hydrograph characteristic shape reproduces real hydrographs or not. In **Figure 2.5**, the shape of the created and observed hydrographs are compared. As shown in **Figure 2.5**, calculated hydrograph (Cal.) has a similar shape as the measured hydrograph (Obs.). Moreover, the mean value of the correlation coefficient (R^2) between the calculated

data and the observed data was estimated as 0.9505. Therefore, the hydrograph characteristic shape is useful to create a typical shaped hydrograph with arbitrary peak discharges in the study location.

To reflect the relationship between non-uniform vegetation growth and peak discharge, this study considered three discharge levels: MF (Moderate Flood) season (peak discharge: 690 m^3/s), AMF (Annual average Maximum Flood) season (peak discharge: 1381 m^3/s), and EF (Extreme Flood) season (peak discharge: 2762 m^3/s). The AMF is the annually averaged maximum peak discharge of the study area, the MF season is assumed to have half the peak discharge of AMF season, and the EF season is assumed to have twice the peak discharge of AMF season. Note that all the three general discharge magnitudes have been observed in the study area. In addition, all the durations of the flood events are unified into the duration of the normal case (150 h per one flood event) to consider the same vegetation growth time. Here, each flood event duration is 150 h, which is longer than the observed flood event in **Figure 2.5**. However, all observed discharges in **Figure 2.5** start with overlapping on the previous flood event; therefore, the real duration of the flood event is longer or similar to that of the generated hydrograph characteristic shape.

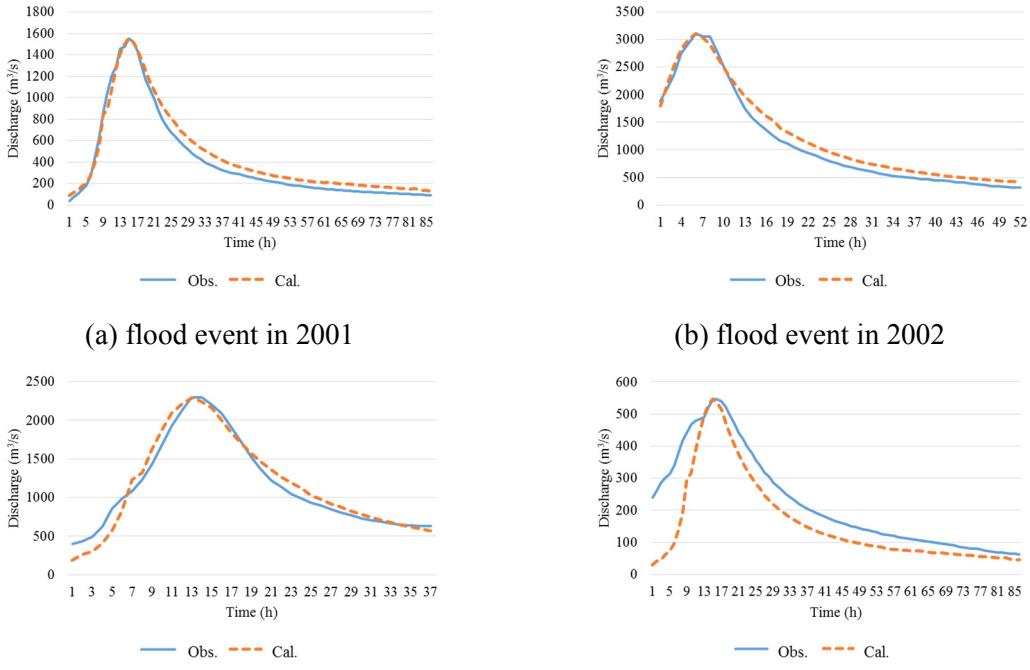

(a) flood event in 2001

(b) flood event in 2002

(c) flood event in 2006

(d) flood event in 2014

Figure 2.5 Comparison of observed and calculated flow discharge (Obs: observed discharge; Cal: reproduced discharge using hydrograph characteristic shape with peak discharge).

If the simulation is run for the AMF season (peak discharge: 1381 m^3/s), the final channel pattern should match the surveyed data (see Section 2.3), because the river bed and topography have been in a state of morphological equilibrium (maintaining a point bar shape in this study) for a long period of time. It is difficult to determine the number of flood events attaining morphological equilibrium. Therefore, in this study, we arbitrarily selected the number of flood events (three times), referring the annual averaged frequency of typhoon (three times/year in Korea) (National Typhoon Center, 2010). We tried to check the validity of the number of flood events. For this, we introduced autocorrelation ratio (C_r) of the bed profile between the current bed profile and the previous bed profile (before 6 hours, which is arbitrarily selected, and is enough long to cause bed elevation change and is much shorter than the period of one flood event). The autocorrelation ratio (Gran and Paola, 2001) was calculated using **Equation**s (2-29)–(2-32) as follows:

$$C_r = \frac{\mathrm{cov}(z_b, z_p)}{\sqrt{\mathrm{var}(z_p)\mathrm{var}(z_b)}} \tag{2-29}$$

$$\mathrm{cov}(z_p, z_b) = \frac{1}{nt}\sum (z_{pj} - \bar{z}_{pm})(z_{bj} - \bar{z}_{bm}) \tag{2-30}$$

$$\mathrm{var}(z_p) = \frac{1}{nt}\sum_{j}^{nt} (z_{pj} - \bar{z}_{pm})^2 \tag{2-31}$$

$$\mathrm{var}(z_b) = \frac{1}{nt}\sum_{j}^{nt} (z_{bj} - \bar{z}_{bm})^2 \tag{2-32}$$

where, C_r is the autocorrelation ratio, z_p is the previous bed profile, z_b is the bed elevation (current bed profile), j is the cross sectional grid index in the Cartesian coordinate; nt is the total number of cross sectional grids, $\bar{z}_{pm}$ is the averaged previous bed elevation in each cross section, and $\bar{z}_{bm}$ is the averaged current bed elevation at each cross section. If the autocorrelation ratio (C_r) reaches 1, the channel is totally stable (no bed changing), while if this ratio reaches to 0, the channel is totally unstable (extreme bed changing) (Gran and Paola, 2001; Jang and Shimizu, 2007). The autocorrelation ratio (C_r) was calculated at every grid cross section at every 1 h. Then, all values of the autocorrelation ratio (C_r) over the entire computational domain were averaged.

Figure 2.6(a)–(c) shows the temporal changes in the autocorrelation ratio (C_r) and **Figure 2.6(d)** shows the hydrograph characteristic shapes with the three different peaks. In **Figure 2.6(a)–(c)**, the correlation ratio (C_r) becomes minimum when peak discharge occurs. We found that the amplitude of variations of C_r becomes mostly stable after the three flood events. In **Figure 2.6(c)** (EF case), the amplitude is still decreasing after the third flood event, but the slope of change becomes suddenly milder.

It indicates that those bed shapes can be assumed to reach the periodically quasi-equilibrium state. The results imply that the hydrograph including three flood events will cause no serious problems to consider the effects of vegetation.

In all, six simulation cases of three flood discharges each were run in this study. The total duration of the flood event was set as 450 h in all simulation cases. Non-uniform vegetation growth and permanent vegetation growth were considered for each discharge case, as presented in **Table 2.2**.

Table 2.2 Simulation conditions depending on discharge.

No.	Peak Discharge (m^3/s)	Total Flood Duration (h)	Growing Vegetation	Permanent Vegetation
Run-1	690	450	No	Yes
Run-2	1381	450	No	Yes
Run-3	2762	450	No	Yes
Run-4	690	450	Yes	Yes
Run-5	1381	450	Yes	Yes
Run-6	2762	450	Yes	Yes

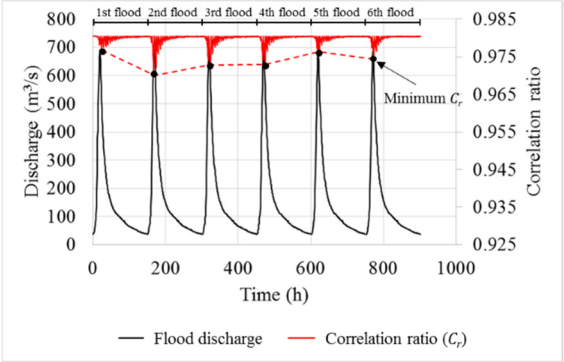

(a) correlation of bed changing (peak discharge: 690 m^3/s)

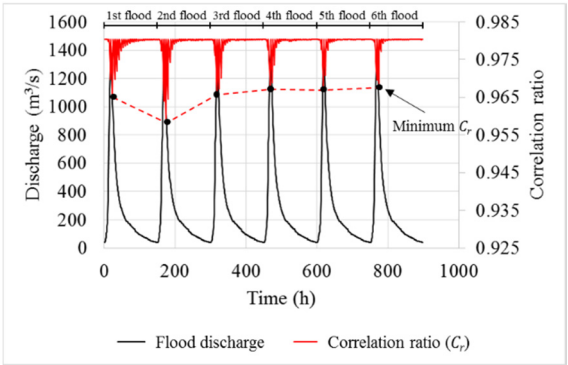

(b) correlation of bed changing (peak discharge: 1381 m^3/s)

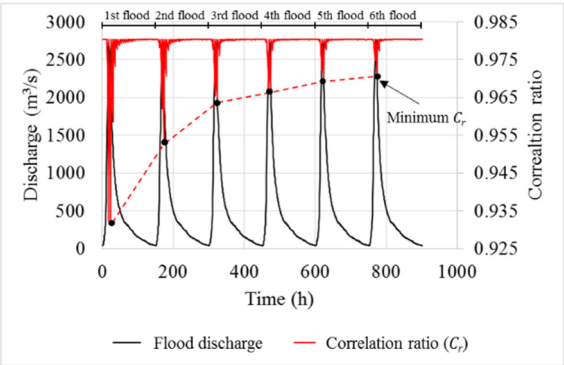

(c) correlation of bed changing (peak discharge: 2762 m^3/s)

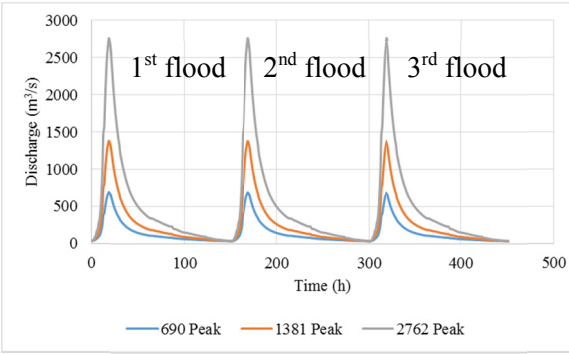

(d) hydrograph characteristic shape. ("Peak" is the peak discharge (m^3/s))

Figure 2.6 Hydrographs of simulation results.

2.2.8 Verification of Simulation

When conducting the simulation, the flat-bed state was set as the initial bed, which has a constant slope (0.0015). This is because this study investigated the responses of bed morphology on growing vegetation effect by comparing several cases (e.g., change in the peak discharge and the presence of vegetation growth effect). To consider the vegetation growth time, the duration of the flood event should be limited and unified, so that we employed the hydrograph characteristic shape (duration is 450 h).

The final simulated channel shape was compared with observed data to verify the model. For these simulation results, a standard hydrograph (see **Figure 2.3**) with peak discharge of a 1381 m^3/s was used. The verification case did not consider the growing vegetation in order to reflect the environment of the present study area. **Figure 2.7** shows the simulated and observed bed elevation of the grid cross sections (the end of the downstream grid is at $i = 319$). The number of measurement points was 11. **Figure 2.7(a),(b)** show a comparison of the observed and simulated cross sections located at a part of the inlet straight channel. **Figure 2.7(c)–(f)** shows the observed and simulated bed elevations along grid cross sections at the meandering part. The bed elevation near the inner bank is higher than that near the outer bank, because point bar is developed near the inner bank. Moreover, secondary flow of the first kind occurs and erodes the river bed near the outer bank during flood event such that the bed elevation near the outer bank is lower.

Figure 2.7(d) shows that the outer bank totally collapsed because this model used the slope failure model (Section 2.1.5) and the angle of repose was 30°. Thus, if the river bed adjacent to the bank is highly eroded, the bank elevation (initially rectangular in this study) can be decreased (Iwasaki et al., 2016a) or the meander amplification is activated. In this study, the river is surrounded by artificial bank and mountain, such that the bank failure does not occur; however, this model cannot consider such bank profile.

The differences of bed elevation between simulation result and observation data are 2–3 m, which may come from some of uncertainties, such as, irregularities on non-uniform grain size, permanent vegetation area and surveyed topography. Nevertheless, the simulated channel profile shows a similar pattern with the observed channel profile. Moreover, averaged correlation coefficient (R^2) between channel profiles in the simulation and observation was 0.63. These results show the adequacy of the present computational setup.

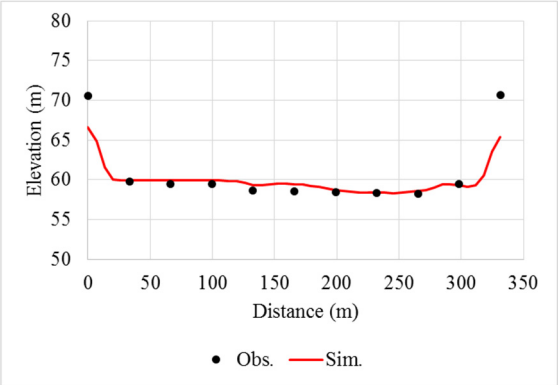

(a) upstream area (at i = 50)

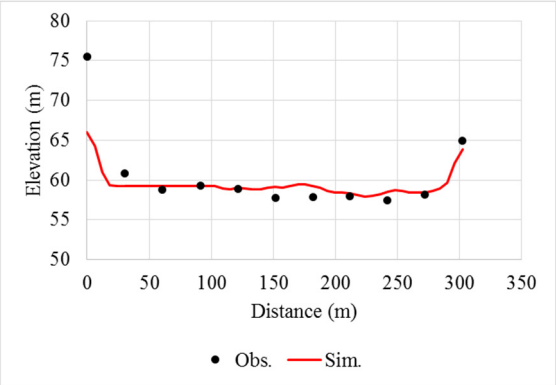

(b) upstream area (at i = 100)

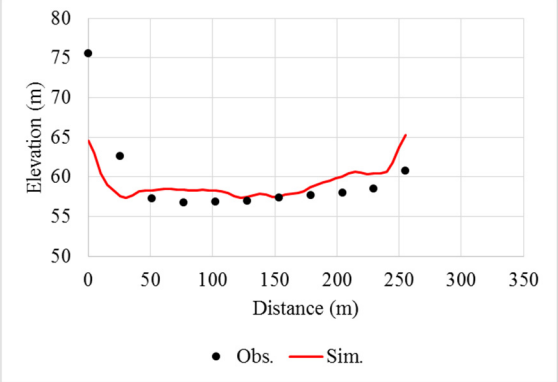

(c) middle stream area (at i = 150)

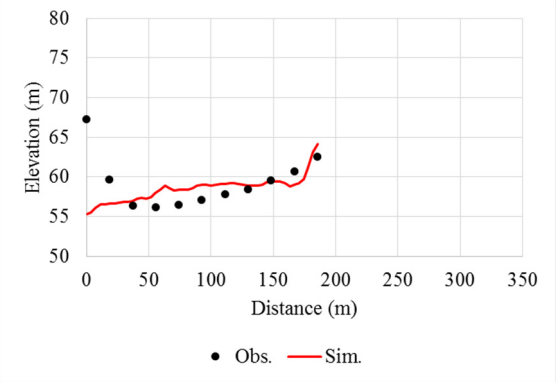

(d) middle stream area (at i = 200)

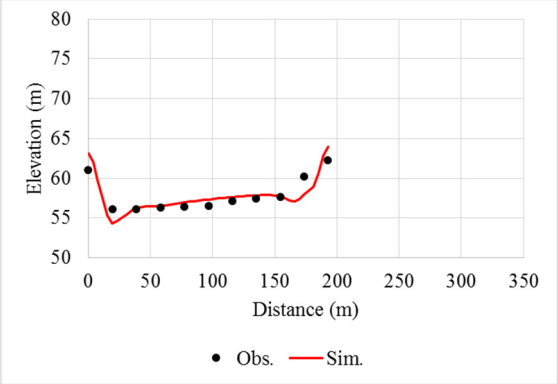

(e) downstream area (at i = 250)

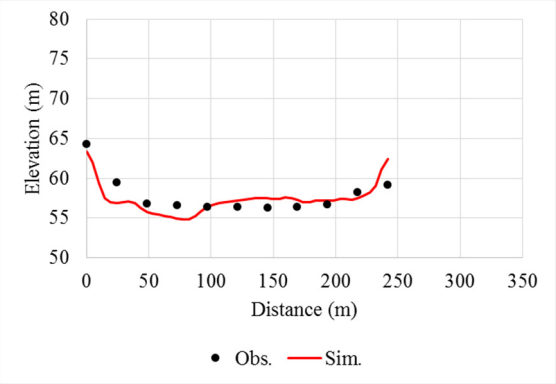

(f) downstream area (at i = 300)

Figure 2.7 Comparison of cross sections (*i* = longitudinal grid) "Distance (m)" indicates the distance from the inner bank (distance = 0 m).

2.2.9 Channel Pattern Quantification

2.2.9.1. Braiding Index

The braiding index is a useful indicator for evaluating the magnitude of channel braiding. This index has been studied using two different methods (Egozi and Ashmore, 2008). One method considers the total sinuosity, while the other method considers the channel count. In this study, the channel count method proposed by Bertoldi, et al. (2009) was used as it calculates the braiding index simply and intuitively. This method employs the total braiding index (TBI) and the active braiding index (ABI). Essentially, the TBI counts the total number of channels at each cross section as shown in **Figure 2.8**, while the ABI counts only the active channels (channels with a Shields number larger than the critical Shields number). Compared with the ABI, the use of the TBI is insufficient to explain the state of spatial sediment transport. Therefore, this study uses the ABI to quantify changes in the channel pattern. If the ABI is large, the river has many thread channels, while if the ABI is small, the river has few channels; a river with an ABI of 1 has only an active single channel.

The cross sections are well defined in 1-D modelling. However, they are not clear for 2-D modelling because it is difficult to clarify the main flow direction. Thus, we considered the grid cross section based on river survey data (**Figure 2.3(b)**) to evaluate the ABI and the BRI.

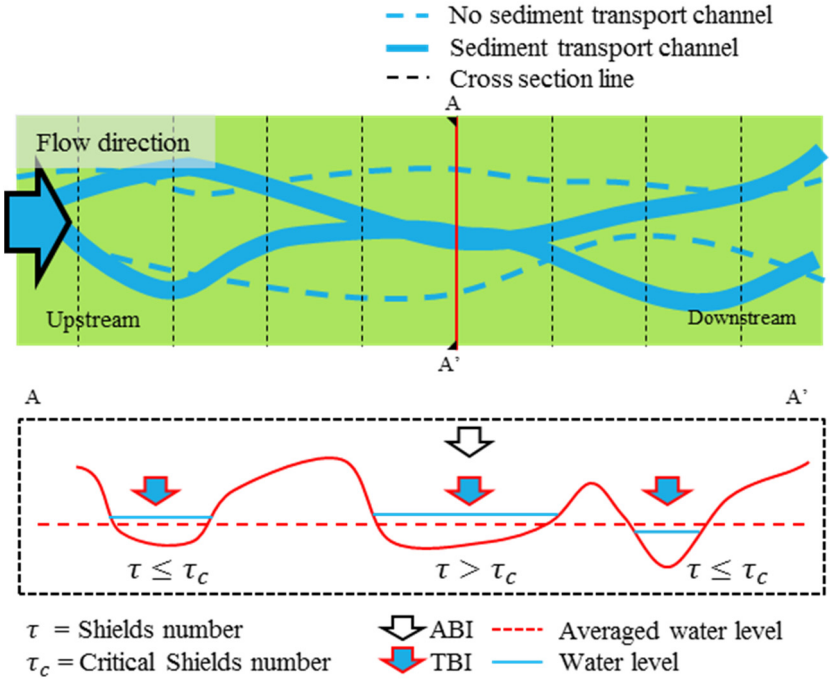

Figure 2.8 Concept of braiding index (cross section A-A' has ABI = 1 and TBI = 3).

2.2.9.2. Bed Relief Index

The bed relief index (BRI) (Hoey and Sutherland, 1991) indicates the magnitude of relief for a river bed. It can be used to evaluate the amount of bed variation and the flatness of the bed level (**Figure 2.9(a)**). In particular, this index the relative depth of the thalweg in consideration of each mean value of the cross-sectional bed elevation: the BRI increases as the thalweg depth increases. The BRI is calculated using **Equation** (2-33):

$$\mathrm{BRI} = \left\{ \sum_{j=1}^{nt-1} \left[\left(z_{bj} - \bar{z}_{bm} \right) \right]^2 \left[y_{j+1} - y_j \right] \right\} / (y_{nt} - y_1) \qquad (2\text{-}33)$$

where, y_j is cross-sectional grid point at j (y direction) in the Cartesian coordinate, $[y_{j+1} - y_j]$ is the distance between grid points j and $j+1$ (m), and z_{bj} is the elevation at y_j.

Figure 2.9(b) shows cross sections for different BRI values. At the same average elevation, if the BRI is 0, the channel has a totally flat-bed; as the BRI increases, the channel has a more uneven bed.

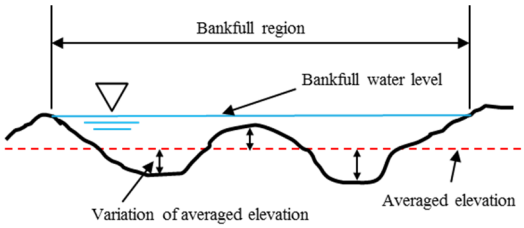

(a) concept of BRI on the cross section

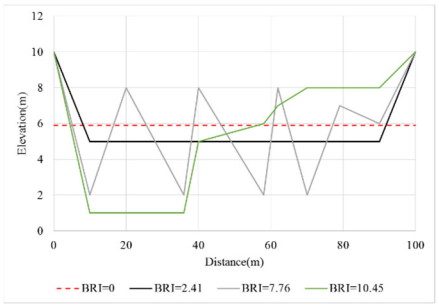

(b) diverse BRI cases on the cross sections at the same average elevation (5.9 m)

Figure 2.9 Concept of BRI.

2.3 RESULTS AND DISCUSSION

2.3.1 Local Erosion and Global Erosion

In a curved channel, the cross-stream velocity is an important factor influencing the main flow pattern. Cross-stream velocity notably increases the strength of the secondary flow of the first kind, changing the shear stresses and resulting in a diverse pattern of erosion depth (Garcia et al., 2012). Eventually, this pattern influences the growth of vegetation and subsequently the changes in bed morphology.

In this study, two types of erosion are defined: Local erosion and global erosion. Local erosion is caused by increased flow velocity near areas of vegetation (Schnauder and Sukhodolov, 2012), as shown

in **Figure 2.10(a)**. This local erosion often increases in several channel threads when water level is lower as a flood event recedes. Global erosion is caused by secondary flow of the first kind during bankfull discharge. If the flow discharge grows large enough and the channel shape is curved, the strength of the secondary flow becomes substantial, as shown in **Figure 2.10(b)**.

These two types of erosion result in different bed changes. Local erosion increases the ABI, because the number of thread channels increases. Global erosion increases the BRI, because it deepens the thalweg. Sometimes, global erosion sweeps away thread channels, decreasing the ABI. The dynamics of local and global erosion are described in detail through the formation of bar and thalweg features in the next section.

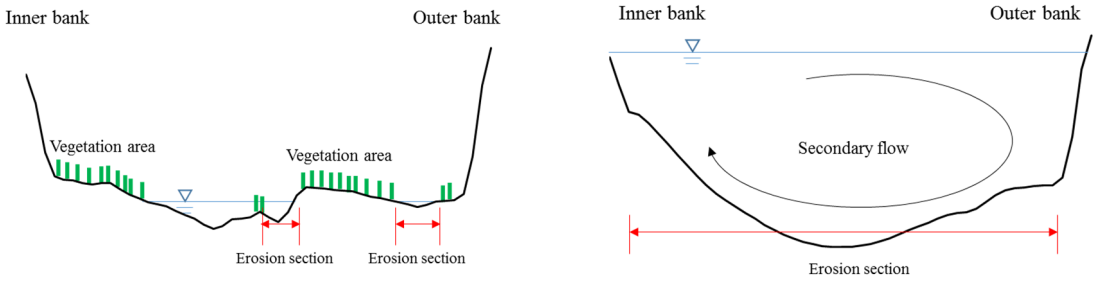

(a) local erosion (b) global erosion

Figure 2.10 Schematic diagram for the global erosion and local erosion.

2.3.2 Final Channel Patterns and Distribution of Vegetation Area

The final channel patterns are shown in **Figure 2.11**, which shows the change in the elevation (m) from the initial flat-bed condition, with a constant initial slope of 0.0015. The ranges are limited within ±0.5 m to clearly express the shifting channel patterns. In all cases shown in **Figure 2.11**, the point bar is well developed by flood discharge. Note that in these Figures, the area just downstream of the inlet maybe affected by the inlet boundary condition. Therefore, the analysis should be carried out in all areas except in this area.

The width of the upper point bar (at the entrance of the meander) increases more for the growing vegetation cases than for the no-growing vegetation cases (for peak discharges of 1381 m^3/s and 2762 m^3/s). In the cases with no growing vegetation, the point bar near the inner bank migrates downstream as the discharge reaches its peak. However, in the cases with growing vegetation, the growth of vegetation on the point bar reduces the flow velocity and captures more sediment, depositing it near the point bar in the lateral direction.

In cases of small peak discharge (690 m^3/s) for the growing vegetation case, the point bar exhibits a smaller width (**Figure 2.11(b)**) than for the same peak discharge under the no-growing vegetation case (**Figure 2.11(a)**). This is due to the reduction in the flow velocity by the growing vegetation, which inhibits the strength of the secondary flow, resulting in a lower flow discharge, which allows vegetation to grow on the outer bank, thus, stabilizing it. As a result, the thalweg does not shift toward the outer bank, instead, it develops along the channel centerline.

Such vegetation colonization (the case of small peak discharge) with bed morphology can be observed in real rivers. Gurnell and Grabowski (2015) carried out field survey and reported that the lack of vegetation colonization together with small stream power can cause the settlement of perennial vegetation that develops within the threads river channel. In addition, if vegetation settlement is initiated with small flood discharge during drought season, vegetation colonization may be accelerated. Gurnell et al. (2006) carried out field survey and analysis with a conceptual model and proposed that the three phases of gravel bed channel are due to the interaction between bed morphology and vegetation colonization: phase 1 is the initiation of the riparian margin, phase 2 is morphological development of the riparian margin, and phase 3 is full morphohydraulic integration of the riparian zone. Specifically, this study explains the development of the river margins. First, a pool and a riffle were created through the formation of the river margins, which is initiated by sediment deposition with initial vegetation settlement, in newly generated channel (phase 1). Then, the vegetation areas expand their colony, which can influence the development of bar migration and channel alteration in phase 2. If the vegetation colonization is fully expanded, vegetation may overwhelmingly control the change of the river channel (phase 3) in a large time scale.

The phase of the present study area can be estimated as phase 2 (**Figure 2.11(c)**) because vegetation initiates the colonization expansion, although the impact is insufficient to change the bed shape (KICT, 2015). However, if the flow discharge is consistently small due to the MF season or dam effect, this study area may expand to phase 3 because vegetation colonization expanded after several years as shown in **Figure 2.11(b)**. **Figure 2.1** also shows such phase change from phase 2 to phase 3.

Meanwhile, the cases of normal peak discharge (peak discharge: 1381 m^3/s) and extreme peak discharge (peak discharge: 2762 m^3/s) may also expand to phase 3; however, it is expected that they exhibit different phases in vegetation colonization and bed changing. These cases may lead to the development of the point bar shape (**Figure 2.11(c)–(f)**); however, the area of the point bar may slightly increase due to expanded vegetation colonization. Therefore, it is predicted that vegetation colonization stabilizes this study area from bed changing in phase 3.

Figure 2.12 illustrates the predicted distribution of vegetation in the study area, showing vegetation growth stage by color. If the growth stage is 0 (blue color), the area has no vegetation because vegetation is unable to grow at a water depth higher than 0.1m (germination depth) or it is removed by bed changing (depth of erosion > 0.8 m). If the growth stage is 1 (red color), the area is covered with permanent vegetation (see Section 2.1.2). Note that the maximum growth stage for growing vegetation is 0.21. In these results, the permanent vegetation area plays an important role in generating the bar and thalweg. Because the flow velocity increases near the permanent vegetation area as it does the near a growing vegetation area, local erosion occurs by chute cutoff (Ashmore, 1991). **Figure 2.12(a)** shows the vegetation areas located on both sides of the channel because the inundation time is short, and the flow velocity is too small to remove vegetation for the smaller peak discharge (690 m^3/s). As a result, the strength of the secondary flow of the first kind is very weak, causing the thalweg to deepen along the centerline. In this case, the local erosion is dominant near the vegetation area, resulting in the development of thread channels.

In cases of larger peak discharge (1381 m^3/s and 2762 m^3/s) a larger vegetation area develops on the point bar (**Figure 2.12(b),(c)**) because the flow velocity causes a strong secondary flow that deepens the thalweg and shifts it toward the outer bank. Therefore, water flow is easily concentrated along the thalweg, and the area of the unsubmerged point bar increases, concurrently increasing the vegetation area more than for the smaller peak discharge case (690 m^3/s).

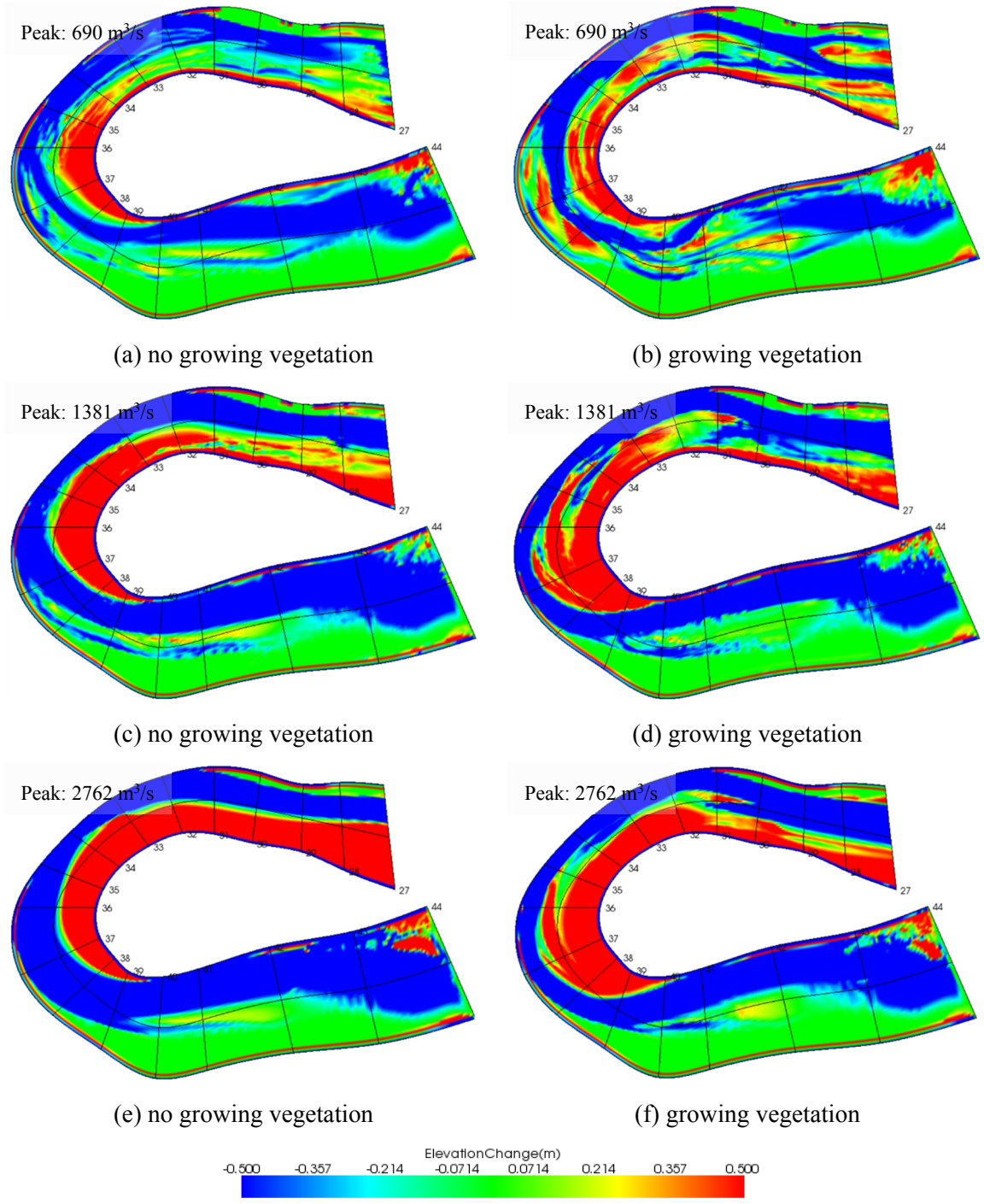

Figure 2.11 Final channel patterns depending on growing vegetation and peak discharge. ”Peak” is peak discharge (m^3/s).

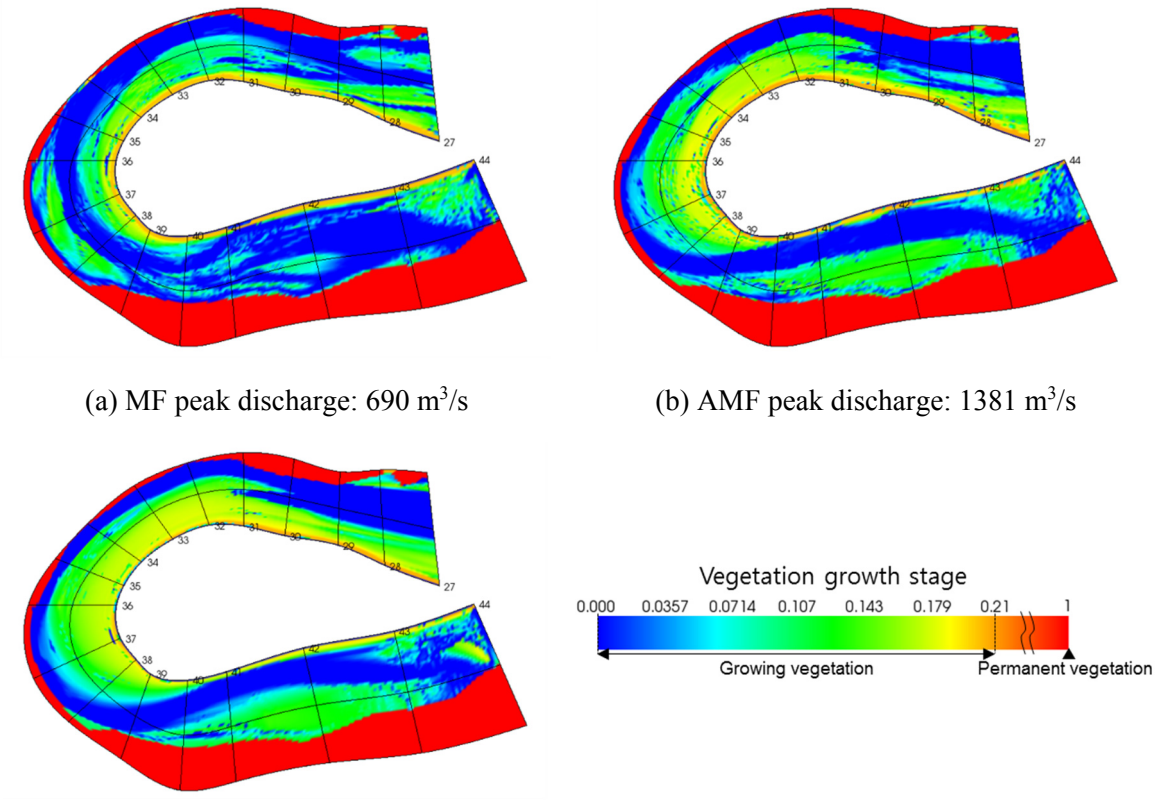

(a) MF peak discharge: 690 m^3/s

(b) AMF peak discharge: 1381 m^3/s

(c) EF peak discharge: 2762 m^3/s.

Figure 2.12 Final distribution of permanent vegetation with growing vegetation (red color: permanent vegetation).

2.3.3 Change in the ABI and BRI over Time

The change in the ABI and BRI were calculated with respect to the time step in order to compare the quantified bed changes. If the ABI increases, several thread channels or islands have been generated. If the ABI decreases, the number of thread channels has decreased. If the BRI increases, the thalweg has deepened, and if the BRI decreases, the thalweg has become shallower.

The change in the ABI over time exhibits different patterns depending on the level of the peak discharge (**Figure 2.13**). If the peak discharge is low, the maximum ABI increases because global erosion is weak. Instead, chute cutoff becomes active, and, in the case of growing vegetation, the flow velocity increases near the growing vegetation and causes local erosion. This, in turn, causes channel threading. As a result, for a small peak discharge, the change in ABI over time is larger for the growing vegetation case than for the no-growing vegetation case.

When the flood discharge is extreme (2762 m^3/s), the maximum ABI decreases (**Figure 2.13(e)**) because all channels have been inundated by the high flood discharge, which raises the water level. Furthermore, global scale erosion caused by a strong secondary flow of the first kind results in a decrease in the ABI.

The change in the BRI over time also exhibits different patterns depending on the peak discharge for the growing vegetation case. When the peak discharge is low (690 m^3/s), the change in the BRI over time decreases; when the peak discharge is high, the change in the BRI over time increases (**Figure 2.13(b),(d),(f)**). In particular, a high discharge through a meandering channel may cause water flow to concentrate along the thalweg, which then shifts to the outer bank due to the secondary flow of the first kind. This results in a deepening of the thalweg, followed by an increase in the BRI.

Clearly, the ABI and BRI are altered by the effects of vegetation for different degrees of flow discharge. For a small discharge (690 m^3/s), the vegetation acts to accelerate local erosion (Iwasaki et al., 2016a; Schnauder and Sukhodolov, 2012; Wolfert, 2001), which increases the ABI. Similarly, if the peak discharge is low (690 m^3/s), the BRI increases slightly over time due to local erosion of the vegetation area, whereas if the peak discharge is high (1381 m^3/s), the BRI increases significantly for the higher discharge and vegetation effects, which accelerates both local and global erosion.

However, if the peak discharge is extreme (2762 m^3/s), the change in the BRI over time is less than for the no-growing vegetation case because the larger vegetation area limits the scale of the secondary flow of the first kind, resulting in global erosion within unvegetated areas, such as the thalweg (Garcia et al., 2012). Therefore, the maximum depth of erosion increases along the thalweg, but the depth of the thalweg remains shallower than for the no-growing case.

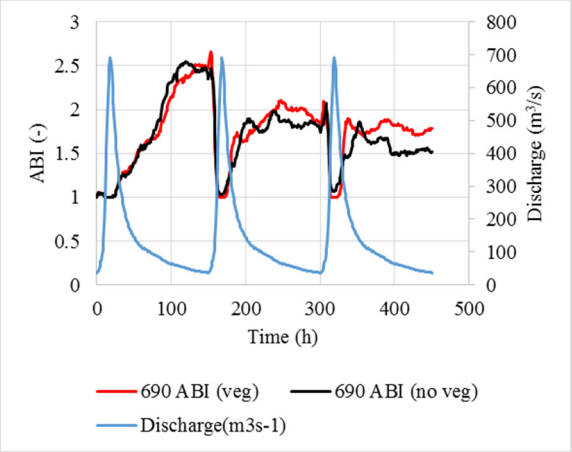

(a) MF peak discharge: 690 m^3/s

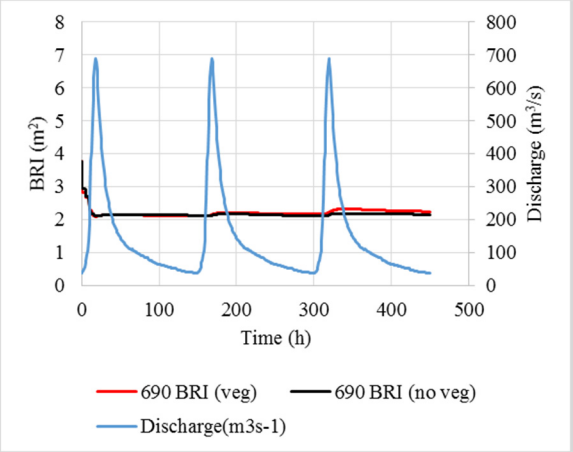

(b) MF peak discharge: 690 m^3/s

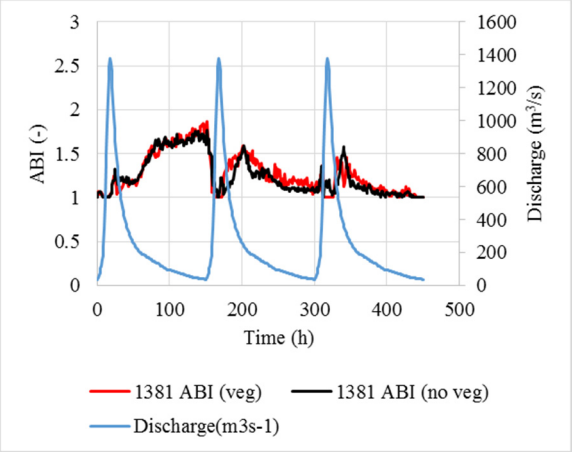

(c) AMF peak discharge: 1381 m^3/s

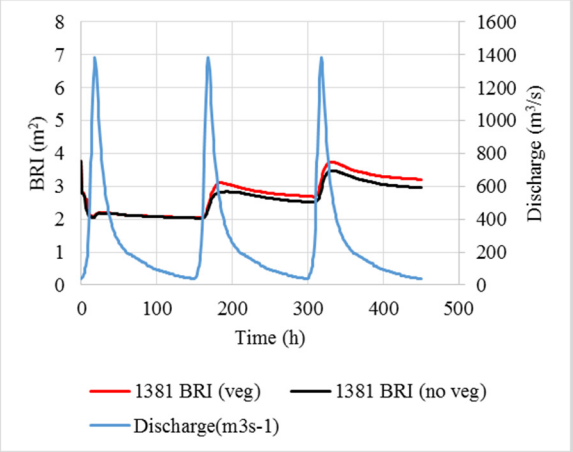

(d) AMF peak discharge: 1381 m^3/s

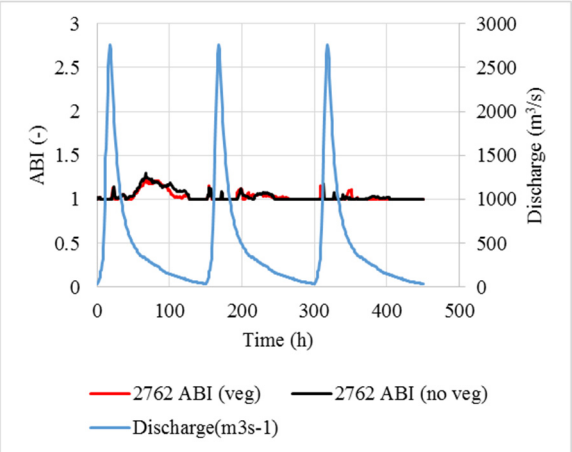

(e) EF peak discharge: 2762 m^3/s

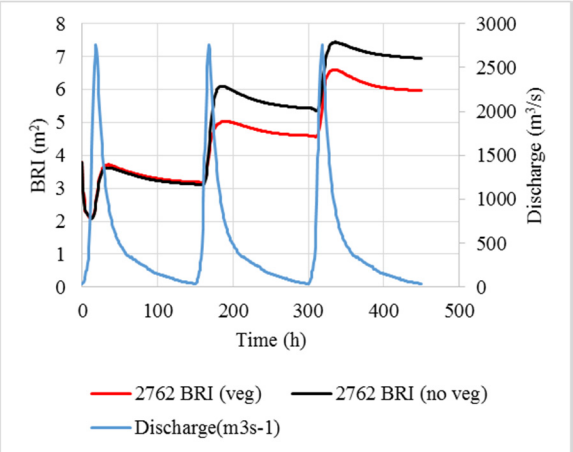

(f) EF peak discharge: 2762 m^3/s

Figure 2.13 Temporal change of ABI and BRI. (ABI: (a); (c); (e). BRI: (b); (d); (f))

2.3.4 Bar and Thalweg Dynamics under Different Levels of Flood Discharge: First Flood Event

For each vegetation simulation case, three consecutive occurrences of one of three flood magnitudes were evaluated. This section describes the bar and thalweg dynamics under the occurrence of the first flood event.

During the rapidly increasing flow stage approaching peak discharge, the riverbed begins to actively erode due to the increasing flow velocity and water level. An alternating bar then rapidly develops and migrates downstream. When the flood discharge reaches its peak, the entire computational domain is inundated by water flow. At this time, the ABI decreases to 1 (indicating the presence of a single channel), and the BRI increases (**Figure 2.13**).

Under these conditions, the effects on the outer bank are dominated by erosion due to the secondary flow of the first kind. While the inner bank also faces erosion, it is relatively less severe. As a result, the water flow sweeps away the alternating bar near the outer bank, and the alternative bar near the inner bank migrates downstream where it changes into a point bar.

If the peak discharge is extreme (2762 m^3/s), the inundation time is longer, the secondary flow grows larger, and global erosion is dominant in the entire study area. At this time, a deeper thalweg develops, causing the BRI to dramatically increase (**Figure 2.13**). However, the ABI collapses to 1 because the entire channel is submerged by the water flow (**Figure 2.13(e)**).

As the flood recedes, the water level gradually decreases, and water flow concentrates from the point bar near the inner bank into the thalweg near the outer bank. At same time, a thread channel is generated by chute cutoff [62], and local erosion occurs near the permanent vegetation area, so that the ABI increases and the BRI decreases. If the peak discharge is small (690 m^3/s), the thalweg develops along the centerline of the channel because the secondary flow of the first kind is insufficient to erode towards the outer bank.

In the second and final flood events, the river bed responses show partially similar channel patterns to the first flood, but the area of the point bar and thalweg are more developed, eventually initiating shape maintenance (**Figure 2.11(a),(c),(e)**). In particular, **Figure 2.13(c)** indirectly shows the developing process of thalweg through the changes in ABI. At the tail of the first flood, thalweg and chute cutoff are actively developed in the first flood, thus ABI increases. In addition, then, the thalweg moves and expands towards near the outer bank in second and third floods, thus, the thread channels by chute cutoff is engulfed in thalweg. Therefore, ABI decreases in the tail of second and third floods.

2.3.5 The Effect of Vegetation Depending on the Peak Discharge: Second and Third Flood Event

During the occurrence of the first of three floods, the cases under the effects of growing vegetation show similar patterns to the cases under no growing vegetation (Section 3.4). The changes in ABI and BRI over time also show similar patterns (**Figure 2.13**), because the effect of growing vegetation is not initially strong. However, after the first flood event, the vegetation effect grows stronger and the bed change displays a different pattern as the vegetation begins to grow.

Figure 2.14 shows the final cross-sectional elevation of the midstream channel (**Figure 2.14(d)**). In this **Figure**, "veg case" indicates the growing vegetation case and "no veg" indicates the no-growing vegetation case. Under growing vegetation case, "Veg growth stage" indicates the growth stage of the vegetation rate depending on the given location in the cross-sectional direction. If "Veg growth stage" is 1, the area exhibits permanent vegetation, which is typically located on the outer bank, if the rate is less than 1 and greater than 0, the area exhibits growing vegetation, and if the growth stage is 0, the area is unvegetated. However, "Veg growth stage" of the no-growing vegetation case only indicates 1 near the outer bank as permanent vegetation, which is same with permanent vegetation under growing vegetation case. Using **Figure 2.14**, the depth of the thalweg and degree of erosion can be estimated in relation to the peak discharge.

Under a small degree of peak discharge (690 m^3/s) with growing vegetation, the flow velocity increases near the areas of vegetation (containing both permanent and growing vegetation), causing local erosion and increasing the depth of erosion (**Figure 2.14(a)**). This erosion accelerates to generate several thread channels (Iwasaki et al., 2016a; Schnauder and Sukhodolov, 2012; Wolfert, 2001), so that both the BRI and ABI increase over time.

If the peak discharge is larger (1381 m^3/s), rather than creating thread channels, the depth of the thalweg increases, and the thalweg shifts toward the outer bank (**Figure 2.14(b)**). Because such a large flood discharge increases the flow velocity, a curved channel, in particular, increases the degree of erosion in the transverse direction due to secondary flow of the first kind. Under this peak discharge with growing vegetation, both local and global erosion is activated by the effects of the vegetation and secondary flow. As a result, the maximum ABI decreases, while the maximum BRI increases more than under the no-growing vegetation cases (**Figure 2.13(c),(d)**).

However, if the peak discharge is extreme (2762 m^3/s), the effect of the vegetation changes. In this case, global erosion is dominant as the discharge reaches its peak. As a result, the thalweg readily shifts toward the outer bank, so that the unsubmerged area on the point bar increases and the vegetation

area expands along the larger point bar. If vegetation expands sufficiently, this area can easily limit the scale of secondary flow (Garcia, 2012), because the flow velocity decreases along the vegetation. Therefore, global erosion is activated within the unvegetated areas, such as the thalweg, and the growing vegetation case in **Figure 2.14(c)** shows a shallow thalweg near the outer bank. Consequently, the change in BRI over time is smaller than that of the no-growing vegetation case.

Note that, in **Figure 2.7** at the Section 2.2, we compared the cross-sectional patterns between observation data and simulation data and found that the difference of the two data is 2–3 m, which was expected to be induced by some uncertainties in the field conditions. In **Figure 2.14**, we can find same order of difference between two data, however the meaning of the difference is very different from the case in **Figure 2.9** because **Figure 2.14** shows the comparison of two simulation results, which use completely same conditions except vegetation effect. Therefore, we can consider that the difference of two results in **Figure 2.14** clearly indicates the vegetation effect.

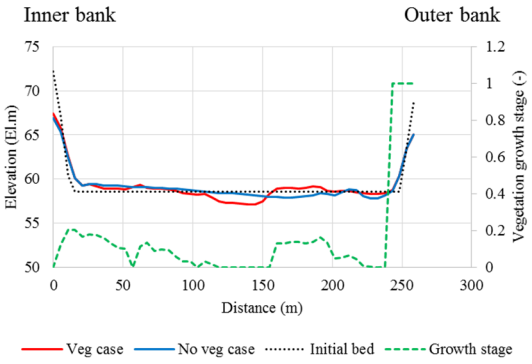

(a) MF (690 m^3/s) peak discharge

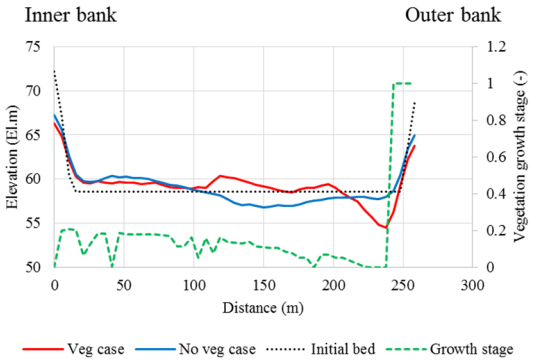

(b) AMF (1381 m^3/s) peak discharge

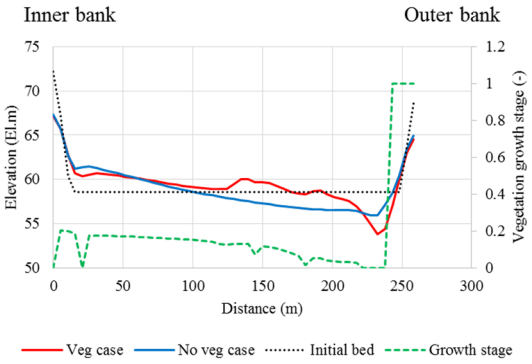

(c) EF (2762 m^3/s) peak discharge

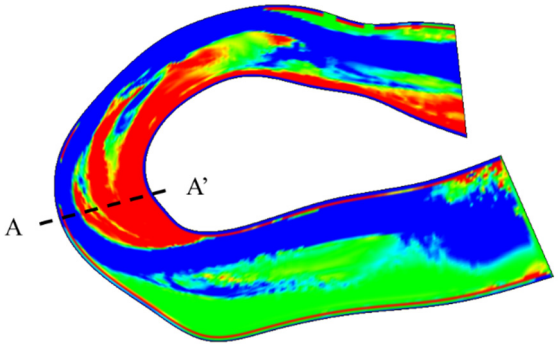

(d) location of cross section A-A'

Figure 2.14 Cross sectional bed changing depending on vegetation and peak discharge.

2.3.6 Limitation of Modelling and Suggestions

In the present study, the simulation results have reproduced well the observation data, such as point bar, alternating bar, and vegetation effect. However, these results have some limitations. The simulations were carried out under the initial condition with flat bed, which has a constant slope. Therefore, the results of simulations may show rather conceptual and yield typical patterns in bed morphology depending on the vegetation effect and the hydrograph characteristic shape. The most appropriate way for the verification of model is to use detailed survey data regarding bed topography and vegetation for the initial condition. However, such detailed survey data is presently not available. Thus, it is unavoidable to set initial conditions with some artificial way. We expected that simplest bed shape for the initial condition makes it easy to consider the results. Thus, we use the flat bed for the initial condition. It is desirable to obtain more detailed field survey data for the initial condition in the future research.

In addition, the parameter in the vegetation growth model should be specifically considered. Inherently, this study considered that vegetation growth is characterized by linear increases. This simple approach makes it easier to compare the cases for growing vegetation and no growing vegetation.

Moreover, we only considered the vegetation decay by bed erosion to simplify the vegetation model. The effect of burying vegetation by sediment deposition maybe also important for vegetation decay or change of drag force. However, to consider the burying effect, additional models, such as, the changes of root depth and vegetation height, become necessary. Therefore, the present study only focused on vegetation decay by the bed erosion for simplicity. The necessity of the burying effect and the model of it should be considered in further study.

2.4 SUMARRY

In this chapter, we conducted simulations using a two-dimensional, depth-averaged river flow and river morphology model to investigate the effect of vegetation growth and degree of flow discharge on a shallow meandering channel. To consider the effects of these factors, it was assumed that vegetation growth stage is changed by water flow and bed erosion. The non-uniformity of the vegetation growth was induced by the non-uniform and unsteady profile of the water depth due to the irregular shape of the bed elevation and the unsteady flow model reliant on hydrographs to evaluate three types of peak discharges: moderate flow, annual average maximum flow, and extreme flow. To compare the effects of non-uniform growing vegetation, the change in channel patterns was quantified using the Active Braiding Index (ABI), which indicates the average number of channels with flowing water at a cross

section and the Bed Relief Index (BRI), which quantifies the degree of irregularity of the cross-sectional shape. Two types of erosion were identified: local erosion (due to increased flow velocity near a vegetation area) and global erosion (due to the discharge approaching peak and the large depth of the channel). This chapter demonstrated that the growth of vegetation increases both the ABI and BRI when the peak discharge is lower than the annual average discharge, whereas the growth of vegetation reduces the BRI when the peak discharge is extreme. However, under extreme discharge, the ABI decreases because global erosion is dominant. The conclusions from this chapter help to deepen the understanding of the interactions between curved river channels and vegetation.

CHAPTER 3

SLIDING, ROLLING, AND SETTLING MOTIONS OF LARGE WOOD IN SHALLOW FLOWS

3.1 INTRODUCTION

In rivers, large wood is transported together with water and sediment. Deposited large wood affects river morphology by causing local scour and deposition of bed materials. Such large wood may initiate the formation of an island as a midchannel bar (Keller and Swanson, 1979; Nakamura and Swanson, 1993; Abbe and Montgomery, 1996; Gurnell and Petts, 2002; Swanson, 2003; van der Nat et al., 2003; Gurnell et al., 2005; Brooks et al., 2006; Cardenas, 2012). Large wood and deposition patterns can change in response to input processes, channel morphology, and hydrological parameters, including flood events (Montgomery 2003). Past bodies of research showed that the relative influence of those factors changes along the river system (Gurnell et al., 2002; Collins et al., 2012; Keller and Swanson, 1979; Gurnell et al., 2000a; Gurnell, 2013), resulting in distinct downstream trends in large wood accumulation style (Keller and Swanson, 1979; Gurnell et al., 1995; Marcus et al., 2002; Comiti et al., 2006). The ratio of wood length to channel width is a key parameter affecting large wood deposition patterns (Gurnell and Sweet, 1998). Large wood deposition patterns are also influenced by diverse parameters, such as drag force, water level, bed friction, and obstacles.

Studies of large wood dynamics have been performed by many researchers. Braudrick et al. (1999), Braudrick and Grant (2000), and Braudrick et al. (2001) provided the basic framework to approach large wood mobility and entrainment in rivers. Based on these studies, several researchers performed studies related to large wood transport dynamics, including Gurnell et al. (2002), Haga et al. (2002), Bocchiola et al. (2002, 2006), Welber et al. (2013), and Berotoldi et al (2014). These studies successfully predicted a wood motion relationship between hydrodynamic and resistance forces, and some of them dealt with transport systems. In studying large wood transport, the large wood shape and density for motion are first considered (Gurnell and Sweet, 1998; Comiti et al., 2006). A piece of large wood may consist of the stem, branch, and/or root wad. Among those, the stem and root wad are the major components of large wood, which actively affect the motion of large wood. Large wood deposition is especially sensitive to the characteristics of the root wad because this part increases the friction with the bed.

Along with many experiments and observations, computational models for large wood dynamics have been developed, such as the Iber-wood two-dimensional (2D) hydrodynamic model (Ruiz-Villanueva et al., 2014a, 2016) and the NaysCUBE (Kimura, 2012) three-dimensional (3D) Reynolds-averaged Navier–Stokes (RANS) model (Kitazono et al., 2016; Kimura and Kitazono, 2017). Both models address large wood dynamics following a Lagrangian method, coupling the water flow with the wood transport. The Iber-wood model considers the wood shape to be a simple cylinder. In contrast, the NaysCUBE large wood model applies a particle method to consider the impinging motion of large wood using a discrete element method. These studies showed the mechanism of large wood dynamics in deep water flows (where the water depth is greater than the wood diameter) to demonstrate floating motion only, and they reproduced the large wood motion well. However, large wood dynamics by integrations between river bed and large wood, such as the root wad effect and anisotropic bed friction, is overlooked in these models although large wood dynamics shows motions of floating motion, sliding motion, and deposition in a natural river system. Clarifying such phenomena by coupling motions (floating, sliding, and settling motions) is crucial in understanding large wood behavior in rivers and the role of large wood floating advection. Thus, it is required to study for the improvement of the computational method in consideration of sliding motion and deposition with root wad effect and anisotropic bed friction as key parameters of large wood dynamics.

This work's main aim is to develop a numerical method for simulating the transport of large wood together with hydrodynamics in shallow flows, considering the root effect under various hydrologic parameters (flow discharge and channel slope). This study presents a newly developed numerical model, which can simulate various behaviors of large wood. We use a 2D depth-averaged flow model (Nays2DH of iRIC: Shimizu et al., 2014 and International River Interface Cooperative, 2017), which is a Eulerian model for calculating the water flow and bed morphology. A Lagrange-type large wood model is newly developed and combined with Nays2DH. The applicability of the present model is discussed through a comparison with the experimental results.

3.2 EXPERIMENTAL SETUP

3.2.1 Scale of Experiment

Among several studies related to large wood and river morphology, Gurnell et al. (2002) first presented the classification of river scales (small, medium, large). Kramer and Wohl (2017) recently systematically categorized four river scales in relation to large wood (**Table 3.1**). We conducted laboratory tests on the medium scale river, which is arbitrarily selected, for a simplified experiment to

examine the reproducibility of the large wood model. The obstacle is useful in clearly making the process of wood deposition with the change of the channel width. We can also observe the transition of large wood motions, such as floating, sliding, settling, and re-moving in shallow flows. The root scale (diameter: approximately 0.01 m) was from Bertoldi et al. (2014).

Table 3.1 Classification of river scales (Kramer and Wohl, 2017)

Scale	River size	Transport
Small river	Channel width/stem length of large wood >1–2 Water depth/diameter of large wood >1–2	Wood not reorganized or transported except during unusual floods or debris flows with recurrence intervals N decadal; large pieces mostly immobile; long residence times regulated by decay and physical breakdown rather than fluvial transport
Medium river	Channel width/stem length of large wood >2–4 Water depth/diameter of large wood >2–4	Hydrologic regime is dominant control; drives periodic transport of stored and newly recruited pieces during high flows; key pieces and jams remain in place during smaller floods, accumulating smaller pieces; larger, more infrequent floods break up and rearrange jams
Large river	Channel width/stem length of large wood >5 or channel width> all wood lengths Depth of flooded channel > diameter of large wood (note that the transition between medium and large rivers at channel widths: ~20–50 m wide because longest wood pieces are in this range)	Wood exported downstream, laterally onto floodplains, or buried; wood exported regularly during high flow; amount of wood transfer highly variable and largely dependent on pattern of antecedent peak flows; high variability in water levels during flooding creates many opportunities for wood sequestration in long-term storage on the floodplain, causing large variability in wood residence time
Great river	~10^6 km^2 or larger Mean annual discharge > 10^3 m^3/s (note that the perennial flow, commonly have vast, seasonally, inundated floodplains, large fine sediment loads, and deep channels)	During most flows, rapid transfer of wood to deposition zones such as deltas, estuaries, or the ocean; lesser rapid fluctuations in discharge stage than large rivers create fewer opportunities for trapping of wood within channel or overbank deposition; wood transfer largely controlled by the spatial distribution and timing of wood recruitment from large tributaries; floodplain wood likely transported and redeposited within the floodplain rather than re-transported to main channel; wood buried within channel bed may be transported downstream annually as part of the bed load

3.2.2 Large Wood and Flume

The flume channel measures 0.3 m × 2 m (Figure 1(a)), and the flume bed was made of very smooth wood panels (**Figure 3.1(d)**). The obstacle size was 10 cm × 10 cm × 10 cm, and two obstacles were attached to the side wall (**Figure 3.1(a)**).

The large wood models were made of wood cylinders with diameters of 1 cm and lengths of 10 cm. The density of the large wood models was 650 kg/m3 in wet conditions (i.e., when floating on water). The root model was made by attaching two thin wood cylinders (0.18 cm in diameter and 2 cm in length) as a cross shape "+" at 90° to the end of the large wood model (Bertoldi et al., 2014; Welber et al., 2013). The shape of the stem was cylindrical; hence, the resistance to the motion in the lateral direction was much smaller than to the motion in the stem-wise direction because of the rolling motion. Hence, small pieces of wood (0.1 cm × 0.2 cm) were attached at the middle of the stem to increase resistance to the rolling motion (**Figure 3.1(b)**).

Table 3.2 shows the experimental cases. This study considered large wood deposition in relation to the channel slope, flow discharge, and root effect. In the experiments, we used two different flume slopes, 0.0045 and 0.007 (m/m), to consider the change in flow velocity under the same flow discharge. Two values of discharge were selected based on the minimal discharge (smaller case) for motion of wood piece with root wad and approximately its twice discharge (larger discharge): a smaller case (0.00065 m^3/s and 0.00060 m^3/s) and a larger case (0.0010 m^3/s and 0.0011 m^3/s). The root effect was also examined in two cases: with and without roots. Therefore, a total of eight cases were investigated in the experiments and in the computations. Each case was repeated thrice to verify reproducibility. A typical case was then selected.

Wood pieces were supplied one by one every four second intervals after the flow reached an equilibrium state (no wave with back water effect). In total, 10 wood pieces were supplied in each case. The initial input direction of the wood pieces was random. The range of the initial positions of the wood pieces was also random, but limited within a circle having a 5 cm radius (starting zone, **Figure 3.1(a)**) because the initial angle and position were difficult to control. These settings were identically applied to the computational conditions.

Table 3.2 Experimental and simulation cases (for simplification cases: none of prototype)

Cases	Flow discharge (m^3/s)	Channel slope (m/m)	Root wad
1	0.00065	0.0045	No
2	0.0010	0.0045	No
3	0.00060	0.0070	No
4	0.0011	0.0070	No
5	0.00065	0.0045	Yes
6	0.0010	0.0045	Yes
7	0.00060	0.0070	Yes
8	0.0011	0.0070	Yes

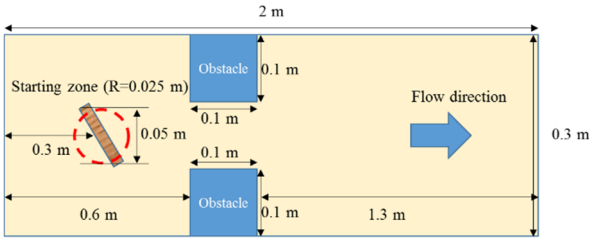

(a) flume design

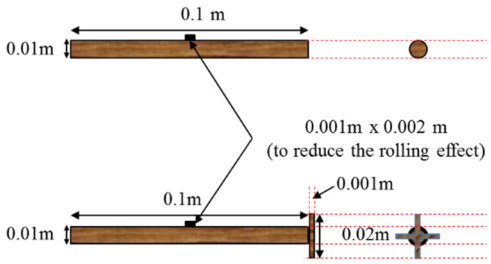

(b) large wood design

(c) large wood samples

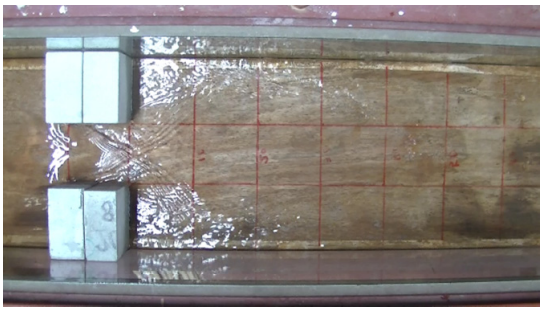

(d) experimental flume

Figure 3.1 Experimental flume and wood piece.

3.3 SIMULATION METHODOLOGY

We used a 2D plane numerical solver developed based on Nays2DH in iRIC to simulate the flows. A third-order total variation diminishing-monotonic upstream centered scheme for conservation laws (TVD-MUSCL) method was used for the advection term, and a zero-equation model was used for the turbulence model. The coupled model was a two-way model that considered the drag force exerted by the large wood on the flow. We estimated the Manning roughness coefficient as 0.006 because the bottom of the flume was flat and smooth. The grid size was set at 1 cm × 1 cm (the number of grids: 200 and 30 in *x*-direction and *y*-direction, respectively) to resolve the flows around the large wood with a diameter of 1 cm. The initial time step (Δt) was 0.0035 s, and the total simulation time was 70 s. Large wood pieces were supplied one by one every 4 s after the flow reached a stable condition (disappear the back water effect near the obstacle) in the same manner that a total of 10 pieces were supplied as in the experimental cases. We reduced the simulation time using the parallelization method (OpenMP).

3.3.1 2D Depth Average Model For Water Flow Dynamics

3.3.1.1 Governing equations for water flow

This model relies upon the depth-averaged momentum and continuity equations to calculate plane 2D flow using **Equations** (3-1)–(3-11) in a generalized curvilinear coordinate system.

Continuity equation:

$$\frac{\partial}{\partial t}\left(\frac{h}{J}\right)+\frac{\partial}{\partial \xi}\left(\frac{hU_{\xi}}{J}\right)+\frac{\partial}{\partial \eta}\left(\frac{hU_{\eta}}{J}\right)=0 \tag{3-1}$$

Momentum equation:

$$\begin{aligned}&\frac{\partial U_{\xi}}{\partial t}+U_{\xi}\frac{\partial U_{\xi}}{\partial \xi}+U_{\eta}\frac{\partial U_{\xi}}{\partial \eta}+\alpha_1 U_{\xi}U_{\xi}+\alpha_2 U_{\xi}U_{\eta}+\alpha_3 U_{\eta}U_{\eta}\\&=-g\left[\left(\xi_x^2+\xi_y^2\right)\frac{\partial H}{\partial \xi}+\left(\xi_x\eta_x+\xi_y\eta_y\right)\frac{\partial H}{\partial \eta}\right]\\&-C_f\frac{U_{\xi}}{hJ}\sqrt{\left(\eta_y U_{\xi}-\xi_y U_{\eta}\right)^2+\left(-\eta_x U_{\xi}+\xi_x U_{\xi}\right)^2}+D_{\xi}\end{aligned} \tag{3-2}$$

$$\frac{\partial U_{\eta}}{\partial t}+U_{\xi}\frac{\partial U_{\eta}}{\partial \xi}+U_{\eta}\frac{\partial U_{\eta}}{\partial \eta}+\alpha_1 U_{\xi}U_{\xi}+\alpha_2 U_{\xi}U_{\eta}+\alpha_3 U_{\eta}U_{\eta} \tag{3-3}$$

$$= -g\left[\left(\eta_x\xi_x + \eta_y\xi_y\right)\frac{\partial H}{\partial \xi} + \left(\eta_x^2 + \eta_y^2\right)\frac{\partial H}{\partial \eta}\right]$$
$$-C_f\frac{U_\eta}{hJ}\sqrt{\left(\eta_y U_\xi - \xi_y U_\eta\right)^2 + \left(-\eta_x U_\xi + \xi_x U_\eta\right)^2} + D_\eta$$

Here, ξ and η are the curvilinear coordinate components, respectively; t is time; g is gravitational acceleration; H is the water level; h is the water depth; D_ξ and D_η are turbulence viscosity terms in the directions of ξ and η, respectively; ν_t is the kinematic turbulent viscosity coefficient; and U_ξ and U_η are contra-variant components of velocity vectors in the directions of ξ and η, respectively. Those vectors are transformed from **Equation** (3-5) and **Equation** (3-4), which are obtained by applying the chain rule for partial differentiations.

$$\xi_x = \frac{\partial \xi}{\partial x},\quad \xi_y = \frac{\partial \xi}{\partial y},\quad \eta_x = \frac{\partial \eta}{\partial x},\quad \eta_y = \frac{\partial \eta}{\partial y},$$
$$x_\xi = \frac{\partial x}{\partial \xi},\quad x_\eta = \frac{\partial x}{\partial \eta},\quad y_\xi = \frac{\partial y}{\partial \xi},\quad y_\eta = \frac{\partial y}{\partial \eta} \tag{3-4}$$

$$U_\xi = \xi_x u + \xi_y v,\quad U_\eta = \eta_x u + \eta_y v \tag{3-5}$$

Here, x and y are the Cartesian coordinate components, respectively; u and v are depth-averaged velocity components in the x and y directions, respectively; ξ_x, ξ_y, η_x, η_y, x_ξ, x_η, y_ξ, and y_η are the components of the matrix between the Cartesian coordinates and the curvilinear coordinates. To transform between the two coordinate systems, the Jacobian of the coordinate transformation (J) and parameters for the transformation of the velocity components ($\alpha_1 - \alpha_6$) are given by **Equations** (3-6)–(3-8).

$$J = \frac{1}{x_\xi y_\eta - x_\eta y_\xi} \tag{3-6}$$

$$\alpha_1 = \xi_x\frac{\partial^2 x}{\partial \xi^2} + \xi_y\frac{\partial^2 y}{\partial \xi^2},\quad \alpha_2 = 2\left(\xi_x\frac{\partial^2 x}{\partial \xi \partial \eta} + \xi_y\frac{\partial^2 y}{\partial \xi \partial \eta}\right),\quad \alpha_3 = \xi_x\frac{\partial^2 x}{\partial \eta^2} + \xi_y\frac{\partial^2 y}{\partial \eta^2} \tag{3-7}$$

$$\alpha_4 = \eta_x\frac{\partial^2 x}{\partial \xi^2} + \eta_y\frac{\partial^2 y}{\partial \xi^2},\quad \alpha_5 = 2\left(\eta_x\frac{\partial^2 x}{\partial \xi \partial \eta} + \eta_y\frac{\partial^2 y}{\partial \xi \partial \eta}\right),\quad \alpha_6 = \eta_x\frac{\partial^2 x}{\partial \eta^2} + \eta_y\frac{\partial^2 y}{\partial \eta^2} \tag{3-8}$$

The turbulent viscosity terms (D_ξ and D_η) can be expressed as follows.

$$D_\xi = \left(\xi_x\frac{\partial}{\partial \xi} + \eta_x\frac{\partial}{\partial \eta}\right)\left[\nu_t\left(\xi_x\frac{\partial U_\xi}{\partial \xi} + \eta_x\frac{\partial U_\xi}{\partial \eta}\right)\right] + \left(\xi_y\frac{\partial}{\partial \xi} + \eta_y\frac{\partial}{\partial \eta}\right)\left[\nu_t\left(\xi_y\frac{\partial U_\xi}{\partial \xi} + \eta_y\frac{\partial U_\xi}{\partial \eta}\right)\right] \tag{3-9}$$

$$D_\eta = \left(\xi_x \frac{\partial}{\partial \xi} + \eta_x \frac{\partial}{\partial \eta}\right)\left[\nu_t\left(\xi_x \frac{\partial U_\eta}{\partial \xi} + \eta_x \frac{\partial U_\eta}{\partial \eta}\right)\right] + \left(\xi_y \frac{\partial}{\partial \xi} + \eta_y \frac{\partial}{\partial \eta}\right)\left[\nu_t\left(\xi_y \frac{\partial U_\eta}{\partial \xi} + \eta_y \frac{\partial U_\eta}{\partial \eta}\right)\right] \quad (3\text{-}10)$$

In **Equations** (3-2) and (3-3), C_f is the riverbed shear coefficient, which is calculated by **Equation** (3-11) with the Manning roughness coefficient (n_m).

$$C_f = \frac{g n_m^2}{h^{1/3}} \quad (3\text{-}11)$$

More detailed formula derivations can be found in the Nays2DH manual.

3.3.1.2 Zero-equation model for eddy viscosity

To consider the turbulent flow, a zero-equation model is used to model a wide and shallow water channel as given in **Equation** (3-12):

$$\nu_t = \frac{\kappa}{6} A_c u_* h + B_c \quad (3\text{-}12)$$

where ν_t is the eddy viscosity coefficient; κ is the von Karman constant (0.4); u_* is the friction velocity; and A_c and B_c are user-defined parameters for the eddy viscosity coefficient (the default values of A_c and B_c are 1 and 0, respectively).

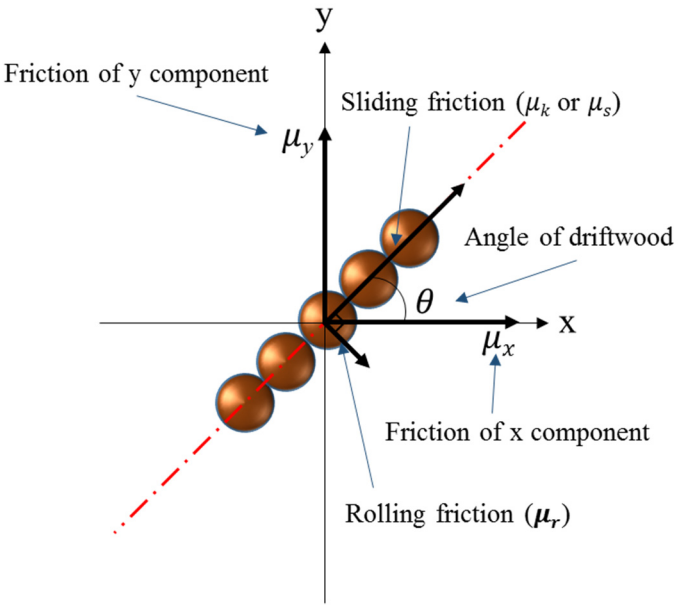

Figure 3.2 Bed friction depending on the stemwise angle of large wood (where the root wad component is expressed as a sphere with twice the diameter at one end of the large wood piece in the simulation).

3.3.2 Particle Method for Modeling Large Wood Dynamics

4.3.2.1 Governing equation for motion of large wood

The large wood movement equation (Kimura, 2012; Kitazono et al., 2016; Kimura and Kitazono, 2017) in Cartesian coordinates is described as:

$$\sigma A_3 d^3 \frac{d\mathbf{u_p}}{dt} = \begin{cases} \mathbf{F_D}+\mathbf{F_{wa}}+\mathbf{F_{am}}-\mathbf{F_{bed}}, & \mathbf{F_D}+\mathbf{F_{wa}}+\mathbf{F_{am}} > \mathbf{F_{bed}} \\ 0 & , \mathbf{F_D}+\mathbf{F_{wa}}+\mathbf{F_{am}} \le \mathbf{F_{bed}} \end{cases} \tag{3-13}$$

where

$$\mathbf{F_D} = \frac{1}{2} C_D \rho \lambda_{A\text{-}sub} A_2 d^2 \left|\mathbf{u}-\mathbf{u_p}\right| (\mathbf{u}-\mathbf{u_p}) \tag{3-14}$$

$$\mathbf{F_{wa}} = \rho \lambda_{V\text{-}sub} A_3 d^3 \left(\frac{d\mathbf{u}}{dt}\right) \tag{3-15}$$

$$\mathbf{F_{am}} = C_M \rho \lambda_{V\text{-}sub} A_3 d^3 \left(\frac{d\mathbf{u}}{dt} - \frac{d\mathbf{u_p}}{dt}\right) \tag{3-16}$$

$$\mathbf{F_{bed}} = \begin{cases} 0 & , h > h_c \\ \mu A_3 d^3 (\sigma - \lambda_{V\text{-}sub}\rho) g, & h \le h_c \end{cases} \tag{3-17}$$

The bed friction coefficient (μ) in **Equation** (3-17), which is an anisotropic friction coefficient, is changed by the large wood angle, as shown in **Figure 3.2**. This parameter is expressed by **Equation** (3-18) and (3-19).

$$\mu_x = \sqrt{(n\mu_{s\,or\,k})^2 \cos^2\theta + \boldsymbol{\mu}_r^2 \sin^2\theta} \tag{3-18}$$

$$\mu_y = \sqrt{(n\mu_{s\,or\,k})^2 \sin^2\theta + \mu_r^2 \cos^2\theta} \tag{3-19}$$

Here, ρ is the water density; σ is the density of large wood; C_M is an additional mass coefficient (C_M= 0.5 was used in this work); C_D is a drag coefficient; A_2 is a 2D shape coefficient (π/4 in this work); A_3 is a 3D shape coefficient (π/6 in this work); d is the diameter of the particle sphere; u is the fluid velocity around the sphere; $\mathbf{u_p}$ is the velocity of the sphere; v is the kinematic viscosity coefficient; t is time; g is gravitational acceleration; and μ_x and μ_y are the x and y components of the friction coefficient, respectively; θ is the large wood angle (θ = 0 indicates the angle matches the x-axis direction); n is the number of particles for one large wood piece; $\mu_{s\text{ or }k}$ is the sliding friction coefficient (s = static, k = kinematic); $\mathbf{F_{bed}}$ is the bed friction force; $\lambda_{A\text{-}sub}$ is the submerged area rate; $\lambda_{V\text{-}sub}$ is the submerged volume rate; $\mathbf{F_D}$ is the drag force; $\mathbf{F_{wa}}$ is the effect of acceleration of the surrounding water; $\mathbf{F_{am}}$ is the effect of the water's added mass; h_c is the critical draft for wood motion. When calculating the sliding friction (**Equations** (3-18) and (3-19)), the sliding friction coefficient ($\mu_{s\,or\,k}$) should be multiplied by the total

number of sphere particles (n) in the large wood because all of particles' sliding friction have the same direction, moving as one material. For the Eulerian momentum equation for water flows, the following drag force terms, which are caused by the large wood, are added.

$$\mathbf{F_{dr}} = -\frac{1}{2}\rho C_D \frac{1}{hA_{cell}} \sum_{n=1}^{N_{cell}} A_n \left|\mathbf{u}^i - \mathbf{u}_\mathbf{p}^i\right| \left(\mathbf{u}^i - \mathbf{u}_\mathbf{p}^i\right) \tag{3-20}$$

Here, A_n is the projected area of a particle toward the flow direction; A_{cell} is the area of a grid cell; and i is the number of particles in the large wood piece.

The present study neglects the effect of collisions among large wood pieces to focus on the large wood advection and deposition patterns. Therefore, each large wood dynamic is independent. However, this numerical analysis includes motion that is indirectly changed by water alterations due to adjacent large wood because such large wood piece is modeled as causing drag force and changing the water depth.

3.3.2.3 Anisotropic friction coefficient

The static friction coefficient between the wood used to construct the flume bed and the large wood is generally approximately 0.4–0.6 (Ambrose and Tripeny, 2011). The friction coefficient under submerged conditions is uncertain, but may be expected to decrease. Therefore, we conducted trials to compare the experiment and the simulation and adjusted the friction coefficients accordingly (**Table 3.3**). The static friction coefficient (μ_s) refers to the friction coefficient when large wood is deposited, and the kinematic friction coefficient (μ_k) refers to the friction coefficient when large wood is sliding. These coefficients are valid in the stemwise direction of wood piece. If the large wood slides in the direction perpendicular to the stemwise direction, the large wood rolls, and the roll friction becomes dominant. **Table 3.3** shows the static, kinematic, and roll friction coefficient.

Table 3.3 Friction coefficients

Friction coefficient	Value
Static friction coefficient (μ_s)	0.4
Kinematic friction coefficient (μ_k)	0.05
Roll friction coefficient (μ_r)	0.001

3.3.2.4 Buoyancy and critical draft for wood motion

One important factor affecting large wood deposition is its buoyancy. This study considers the sphere-by-sphere transition of the submerged volume based on the change in flow depth and the presence of a root wad. The inclination of the settled large wood based on the root wad shape is also reflected to evaluate the buoyancy. The large wood is deposited if the buoyancy is less than the weight of the large wood. The large wood floats if the buoyancy is larger than the gravitational force. If the density of the large wood is less than the water density, the draft of the large wood is determined by the balance between the buoyancy and the weight. If the water depth is the same as the draft, the depth is called the critical draft for wood motion (CDM). In other words, the CDM is the minimum depth at which large wood does not touch the bed. The CDM (hc) is same as the maximum draft in the floating condition, which can be obtained as follows.

The maximum unsubmerged volume of large wood is calculated by **Equation** (3-21).

$$V_e = \frac{B_w - W_d}{\rho_w},\ W_d = \frac{4}{3}\pi r^3 \rho_d,\ B_w = \frac{4}{3}\pi r^3 \rho_w, \tag{3-21}$$

Here, r is the diameter of a large wood particle; W_d is the weight of a **large wood** particle under the totally submerged condition; B_w is the buoyancy under the totally submerged condition; and V_e is the unsubmerged volume of a particle under the totally floating condition, as shown in **Figure 3.3**.

From **Equation** (3-21), we can obtain the maximum unsubmerged volume V_e, and we can obtain the submerged volume V_s using **Equation** (3-22).

$$\begin{aligned} V_s &= \int_r^{a_c} f(y)^2 \pi dy,\ f(y) = +\sqrt{r^2 - y^2} = \pi \int_r^{a_c} r^2 - y^2 dy = \pi \left[r^3 y - \frac{1}{3} y^3 \right]_r^{a_c} \\ &= \pi \left[\left(r^2 a_c - \frac{1}{3} a_c^3 \right) - \left(r^3 - \frac{1}{3} r^3 \right) \right] \end{aligned} \tag{3-22}$$

The unsubmerged volume V_e can also be calculated by **Equation** (3-23) from **Equation** (3-22) and (2-10).

$$V_e = V_t - V_s,\ V_t = \frac{4}{3}\pi r^3 \tag{3-23}$$

Here, V_s is the submerged volume of the large wood particle; V_t is the large wood particle volume; a_c is the water level from the center of the particle (**Figure 3.3**). By executing these equations iteratively, we can obtain the CDM.

In the case of a root wad particle, we assume that its diameter is twice the diameter of a stem particle to model the different drag force and buoyancy of the root. The drag force of a root particle is larger than that of a stem particle because of the root's larger projection area, whereas the root's weight is large because of its increased volume at the same density.

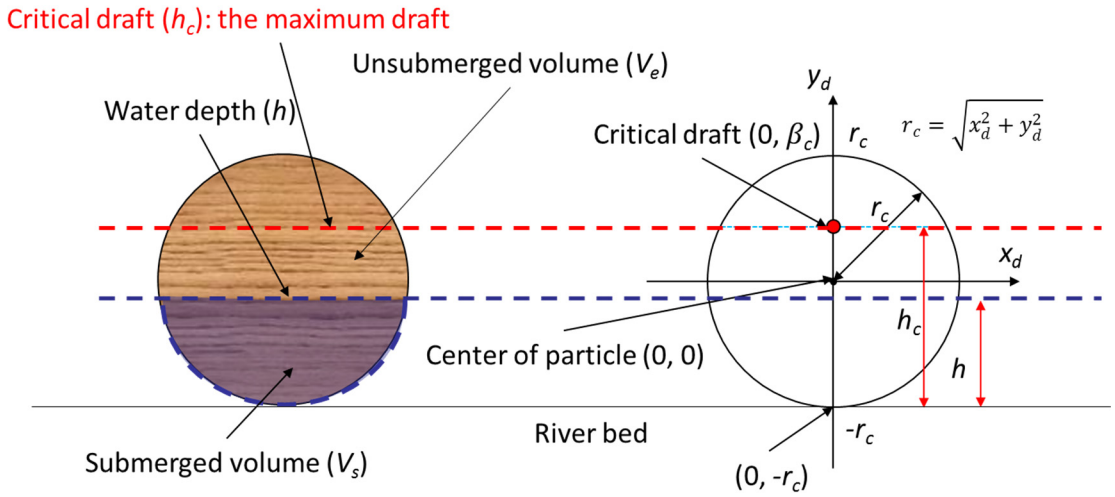

Figure 3.3 CDM concept (structure of submerged large wood (left), geometry of critical draft for wood motion (right)).

3.3.2.5 Change of water depth by root effect

When a root wad of floating large wood (**Figure 3.4(a)**) becomes deposited on the bed at a lower water depth than CDM, the root wad effect is activated, thereby decreasing the draft of the wood piece (**Figure 3.4(b)**). The root wad lifts one edge of the stem up from the river bed; thus, the submerged volume of large wood decreases. The influence of buoyancy is then decreased, and the normal force to the bed increases compared to the case of a large wood piece with no root wad. In the computation, we first determine the CDM of each particle in the large wood piece. A change in the water depth caused by the root wad effect is then applied as follows if the average CDM of the large wood particles is lower than the present water depth (**Figure 3.4(c)**):

$$h_{sn}^{i_p} = h_s - h_r L_a \frac{i_p}{i_{pn}},\ h_r = \left(h_p \times L_d\right) / L_a,\ L_a = \sqrt{h_p^2 + L_d^2} \tag{3-24}$$

Here, h_s is the present water depth under the root particle; h_p is half the difference between the trunk diameter and root diameter; L_d is the trunk length; L_a is the projection length of the trunk length

into the river bed; h_r is the height lift due to the root effect; $h_{sn}^{i_p}$ is the calculated water depth due to the root effect for each particle; i_{pn}, is the total number of particles in the large wood piece; and i_p is the index of each particle.

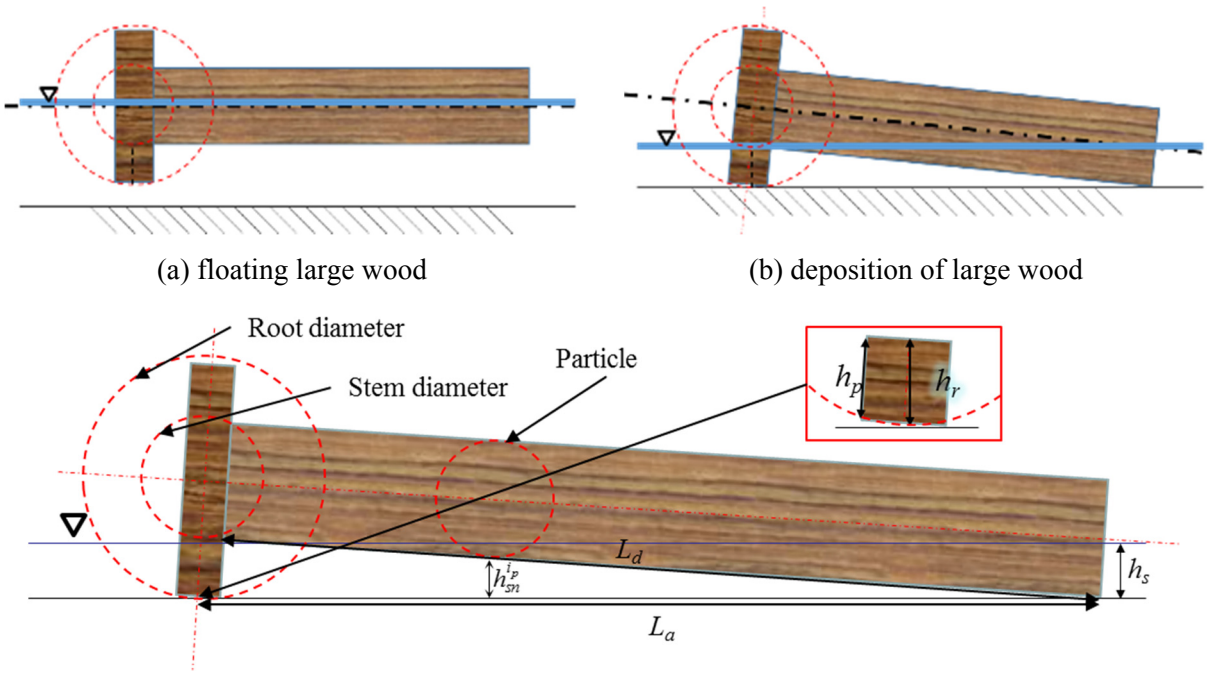

(a) floating large wood

(b) deposition of large wood

(c) change in water depth

Figure 3.4 Change in submerged depth due to root effect.

3.3.3 Interaction between Water Flow and Large Wood

In this solver, the calculation schemes for water flow and large wood are different. In the present large wood dynamics model, one large wood piece is expressed as connected particles, which are driven following the Lagrangian method. Therefore, a method for modeling the interaction between the grid-based water flow and the particle-based large wood motion is required. For this purpose, we use linear interpolation, as shown in **Figure 3.5**, to obtain the flow velocity and water depth at target points on the particles that compose the large wood. If each particle is located at an arbitrary position, the relative length (l_a, l_b) from a standard grid point (F_1) to the center of the particle can be calculated to determine the inverse distance weight. Here, all grid lengths between all grid points are 1 on the generalized curvilinear coordinate system. The value at the particle center (F_{ip}) is then calculated with reference to the values at four surrounding grid points using **Equations** (3-25) and (3-26).

$$F_{ip} = \frac{\sum_{k=1}^{4} \frac{F_k}{A_k}}{\sum_{k=1}^{4} \frac{1}{A_k}} \tag{3-25}$$

$$A_1 = l_a \times l_b,\ A_2 = l_a \times (1 - l_b),\ A_3 = (1 - l_a) \times (1 - l_b),\ A_4 = (1 - l_a) \times l_b \tag{3-26}$$

Here, F_{ip} is the interpolated value at the particle center; F_1–F_4 are grid nodes in the ξ and η directions (ξ and η are generalized curvilinear coordinates), respectively; A_1–A_4 are the weighting area considering the inverse distance from the particle (F_{ip}); and l_a and l_b are the relative lengths from the target point based on the standard grid point (F_1). If the positions of F_1 and F_{ip} are the same, the values of l_a and l_b are 0; k is the index for the grid point.

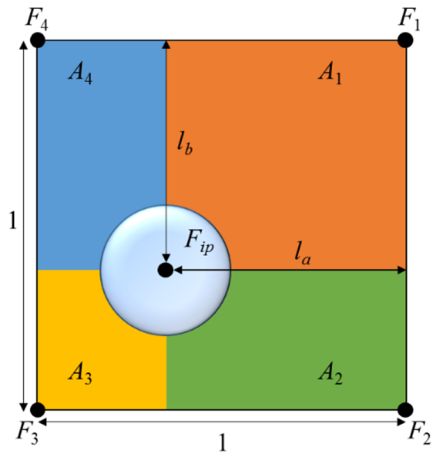

Figure 3.5 Linear interpolation in the particle characterization area to determine the flow velocity and water depth from a generalized curvilinear coordinate system.

Through this interpolation, we can obtain interpolated flow velocity and water depth values at each particle location from a grid node point in the generalized curvilinear coordinate system. Figure 6 shows the process of calculating the interaction between water flow and large wood motion. The specific calculation procedure is as follows:

1) The water flow is calculated using the 2D shallow flow model based on Nays2DH.

2) The submerged volume of the large wood is calculated considering buoyancy and CDM. If the large wood has a root component, the CDM and submerged volume are recalculated.

3) The bed friction acting on the large wood is determined considering the CDM: no bed friction is applied to the large wood motion if the large wood is located in a water depth higher than the CDM. The bed friction coefficient models static friction with roll friction if large wood is stopped; otherwise, the bed friction coefficient models kinematic friction with roll friction.

4) The large wood particle velocity is calculated by drag force with reference to the water flow velocity. The bed friction is considered if the draft of the large wood particle is less than the CDM.

5) From the particle velocity calculation, the advection of each particle is calculated separately without connection for one time step (Δt). The new location of the gravitational center of the large wood is then determined by averaging the new particle locations. In each particle, the rotation angle of the large wood is calculated by averaging the rotation angle of each particle in relation to the large wood piece's center of gravity (**Figure 3.6(b)**).

6) The position of each particle is rearranged into the shape of large wood considering the averaged rotation angle and the center of gravity (**Figure 3.6(b)**).

7) From the rearranged large wood, the drag force is calculated and then applied to the water flow calculation in the next time step.

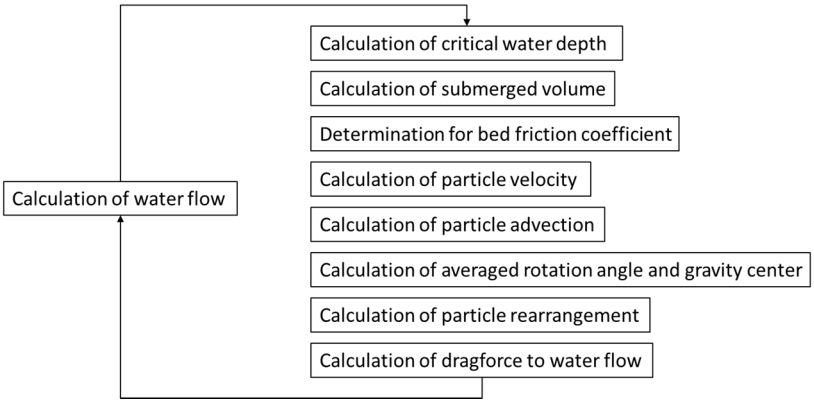

(a) Algorithm for calculating the coupled dynamics of water flow and large wood motion

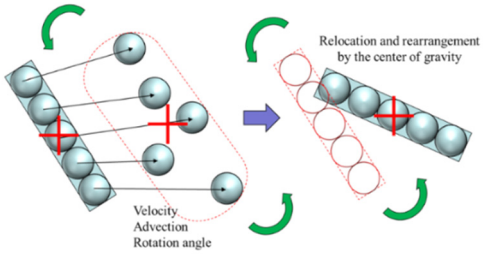

(b) Concept of large wood motion model (cross shape indicates the center of gravity)

Figure 3.6 Calculation concept of large wood motion model.

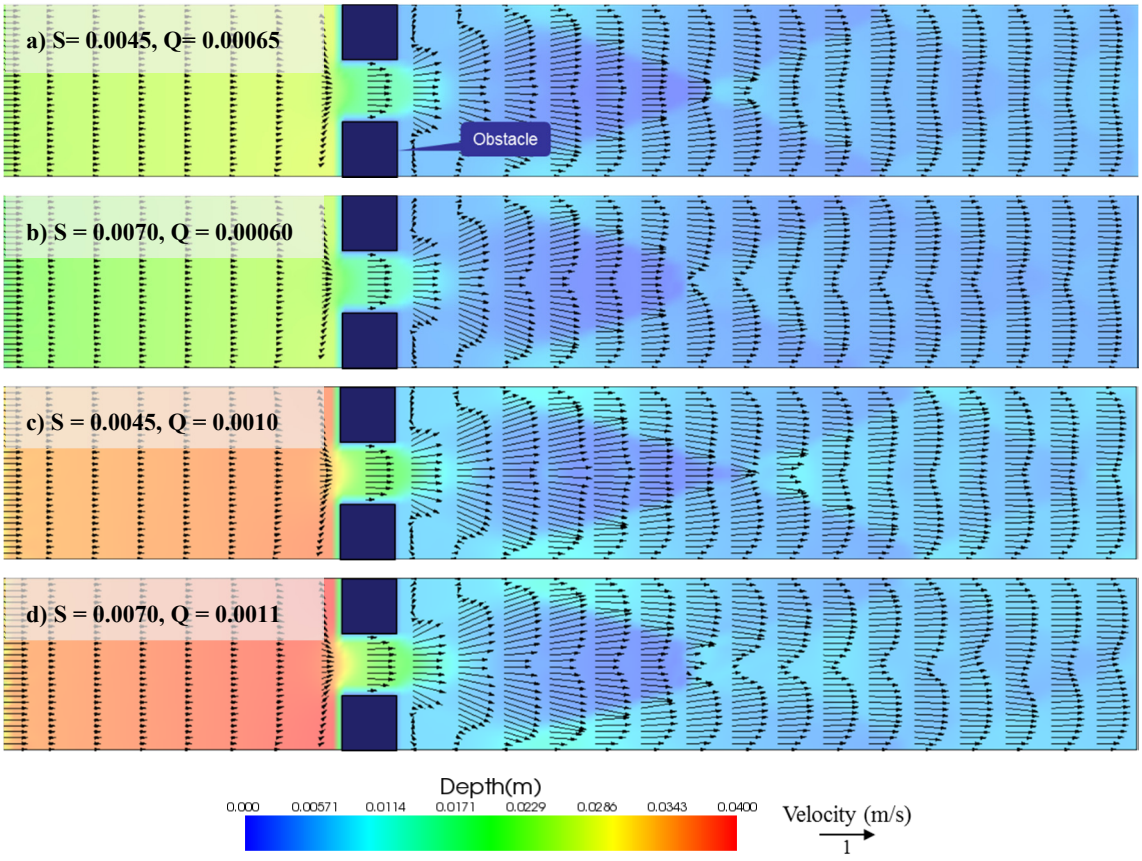

Figure 3.7 Final pattern of flow depth and velocity vector in simulation result (S: channel slope (m/m); Q: flow discharge (m^3/s)).

3.3.4 Verification For Simulation Results In Flow Depth

Figure 3.7 illustrates the final pattern of the flow velocity vector and water depth in the computational domain. The constriction caused by the obstacle forces can cause a transition to the subcritical flow at upstream of the obstacle because the energy of the flow is lower than the minimum energy required to go through the narrow section. The water depth rapidly decreased near downstream obstacles because the supercritical flow was dominant due to the smooth bed. The effect of a localized narrowing also depended on the Froude number of the unaffected flow (upstream of obstacle) and on the constriction ratio (width of narrow section/width of wide section). In other words, the water flow was supercritical with a higher velocity and a lower depth with respect to the non-uniform flow conditions. It also tended asymptotically to uniform flow. Similarly, in the experiment (**Figure 3.8**), a hydraulic jump was observed because of the transition of the water flow from the supercritical flow. **Figure 3.8** compares the water depth along the centerline between the simulations (at the final

computation step) and the experiments. The red box in these figures marks an obstacle section. Although the simulation result overestimated the flow depth upstream of the obstacle, this inconsistency can be neglected because we focused on the area downstream of the obstacle. In the downstream section, the difference between the simulation and the experiment was small. Therefore, the present flow model can be considered to capture the flow depth well.

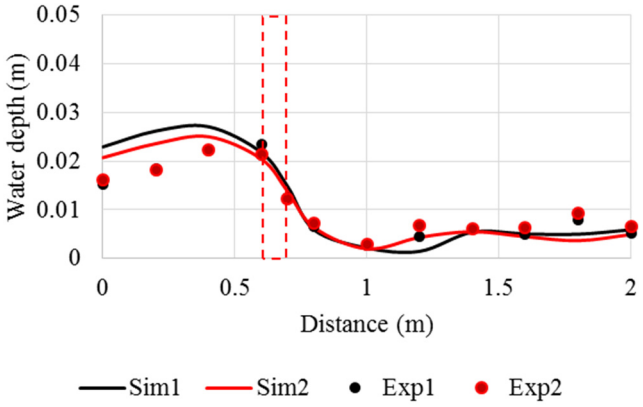

(a) low discharge case (Sim1 and Exp1: S = 0.0045, Q = 0.00065, Sim2 and Exp2: S = 0.0070, Q = 0.00060).

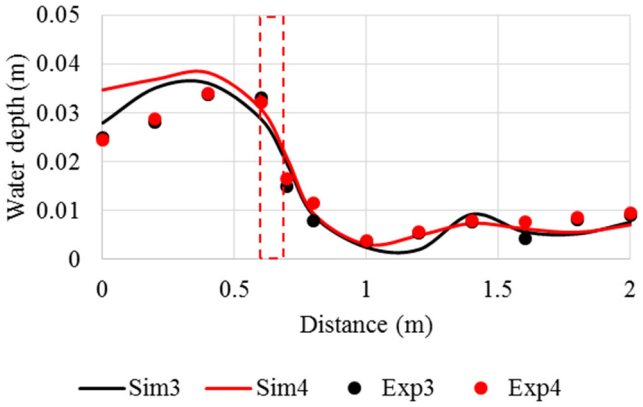

(b) large discharge case (Sim3 and Exp3: S = 0.0045, Q = 0.0010, Sim4 and Exp4: S = 0.0070, Q = 0.0011).

Figure 3.8 Comparison of water depth between the experiment and simulation (red box marks an obstacle; S: channel slope (m/m); Q: flow discharge (m^3/s)).

3.4 RESULTS OF EXPERIMENT AND SIMULATION

3.3.5 Large Wood Cases with No Root Wad (Case 1- Case 4)

As shown in **Table 3.2**, we conducted eight cases of experiment and simulations. This section describes the results of cases 1–4 that considered the wood piece without root wad. Note that no figure for the simulation results was presented in this study. Only experiment results were presented in Figure 9 because none of the wood pieces without root wad was deposited in the simulation results. The experimental results showed that the wood piece without the root wad can become deposited near the side wall (**Figure 3.9**) in contrary to the simulated result indicating no deposition of wood pieces in the flume channel. In the experiments, the roll friction was dominant; hence, when the wood piece was touched on the bed, it was immediately flowed by floating and rolling motion. We expected that the applicability of the depth-averaged 2D model was relatively bad near the side wall because the strong secondary current at the corner between the bed and the sidewall was not considered in the present 2D flow model, and this secondary current increased the flow resistance. In addition, this simulation only considered the motion of the wood piece in the horizontal direction and neglected the advection in the vertical direction; thus, the downward motion of the wood piece induced by the secondary flow was neglected.

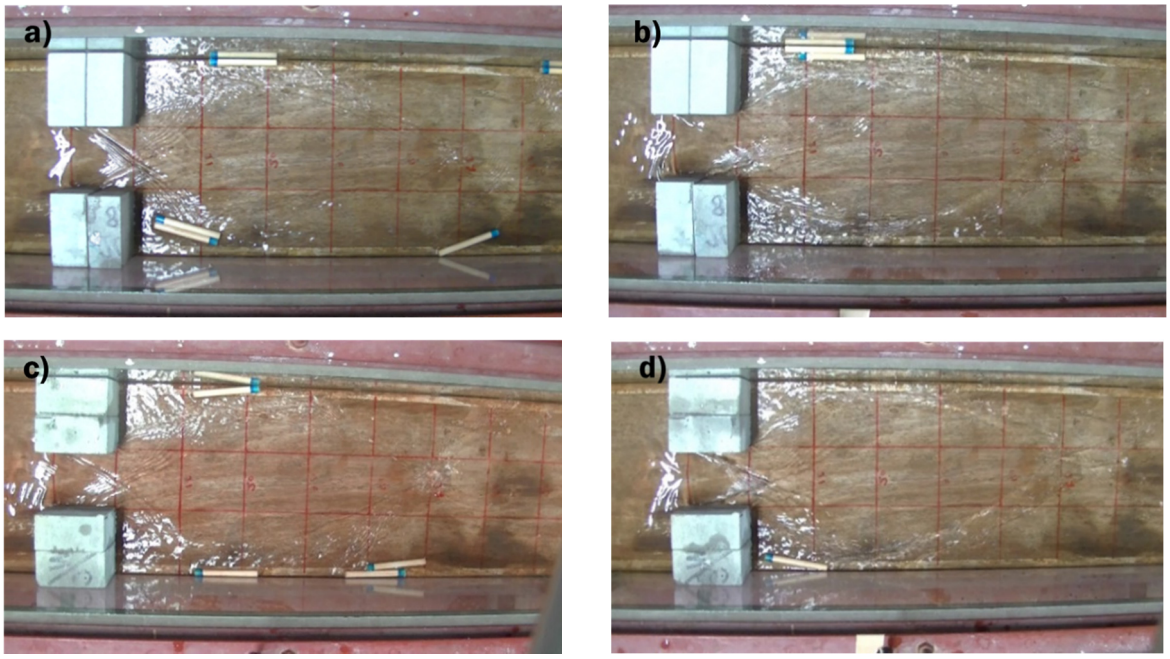

Figure 3.9 Results of experiments using wood piece without roots: a) Case 1; b) Case 2; c) Case 3; d) Case 4.

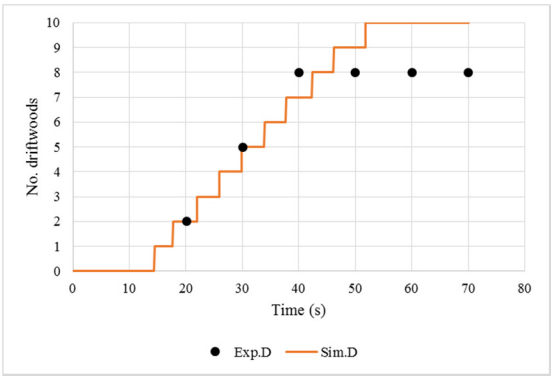

(a) Case 5

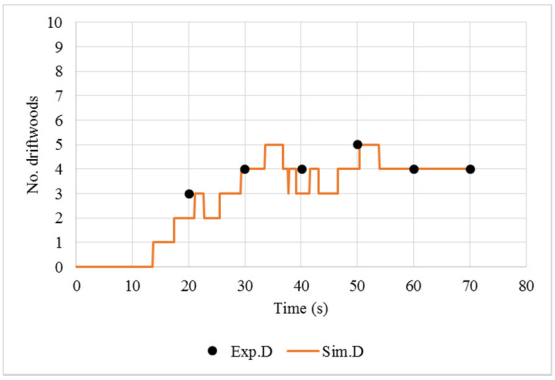

(b) Case 6

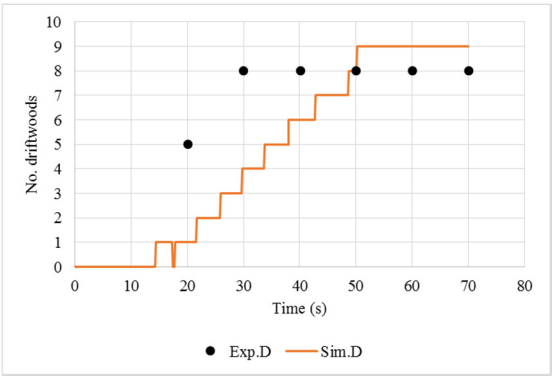

(c) Case 7

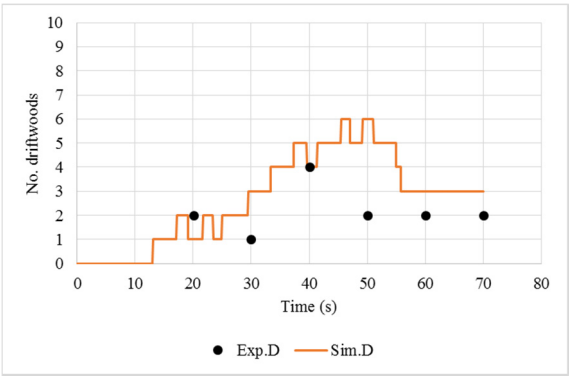

(d) Case 8

Figure 3.10 Time changes in the number of stored wood pieces (Exp. D and Sim. D: the number of stored wood pieces).

3.3.6 Large Wood Cases with Root Wad (Case 5- Case 8)

While the wood piece without the root wad showed no deposited wood in the simulations, the wood piece with the root wad exhibited a clear deposition of the wood pieces. **Figure 3.10** illustrates the time change in proportion of the deposited woods. The range of the final proportion for the deposited wood pieces in the simulation results (30–100%) reproduced the experimental results (20–80%) well. In particular, the deepening on the discharge increased, and the proportion of the deposited wood pieces from the simulation results showed the similar decrease as the experimental results over time. On the contrary, the responses of the changes in the channel slope were unclearly indicated because the channel slope changed only the flow dispersion (**Figure 3.7**), which may be insufficient to affect the motion of the wood pieces.

We measured the final averaged position considering the gravity center of a wood piece in a normalized coordinate using flume width and length to compare the final deposition patterns of the experiments and the simulations (**Figure 3.10**). **Figure 11(a)** shows the final averaged deposition in the streamwise direction, while **Figure 11(b)** presents the distribution of the wood deposition in the lateral direction (mean deviation value). In **Figure 11(a)**, the value of 1 means that all wood pieces are deposited downstream. If the value is 0, all wood pieces are upstream. **Figure 11(b)** indicates the wood dispersal in the lateral direction, where a value of 0 means that the wood pieces are deposited along the channel centerline, and a value of 1 indicates that wood pieces are deposited near a wall.

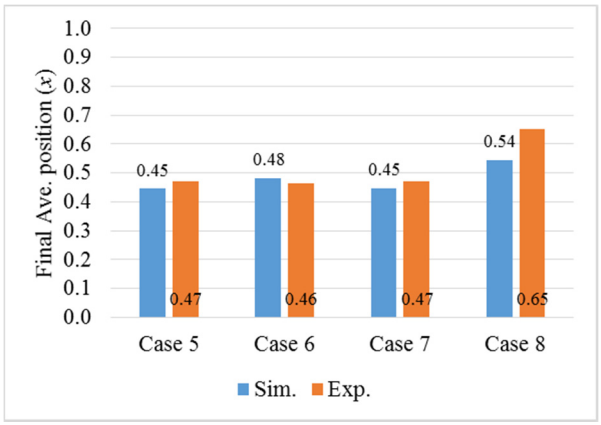

(a) averaged position in streamwise direction

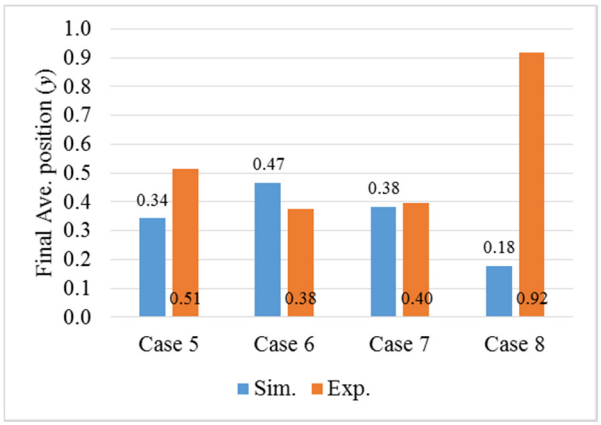

(b) averaged position in lateral direction

Figure 3.11 Final averaged position in deposition of wood pieces.

According to **Figure 3.11(a)**, if the flow discharge is larger (cases 6 and 8), the value of the averaged position increases in the streamwise direction because the larger flow discharge increases the water depth and the flow velocity; thus, the drag force increases, and the influence of buoyancy becomes strong. Meanwhile, the averaged values in **Figure 3.11(b)** show an unclear relation between the wood piece dispersal and two parameters (i.e., discharge and channel slope) because the wood piece dispersal in the lateral direction depends on several parameters, such as the strength of the secondary flow, the angle of stem direction, and the initial position in the lateral direction. The initial conditions must be controlled more strictly (e.g., input stemwise angle of the wood piece and input position should be set uniformly) to analyze this relation.

Figure 3.12 shows the experimental and simulation results for the wood pieces with the root wad. In the simulation results, the yellow items represent the wood piece, where the large head is a root, and the small head is the opposite side. Two types of contours are indicated: water depth (0–0.025 m) and

flow velocity (0–1 m/s). The section that is the focus of this work is up to 80 cm from the obstacles. Once a wood piece is deposited on the center of the flume bed, other wood pieces can easily become deposited around the first piece because the settled wood piece exerts drag force on the flow, decelerating the flow velocity and increasing the water depth. Thus, when the large wood settles on the bed, it acts like vegetation, implying that future work should also carefully consider the bed morphology around settled large wood in real rivers. Vegetation is known to increase the traction force on the bed materials and the water level around it such that the vegetation area captures sediment even though the area immediately adjacent to the vegetation area is eroded by increased flow velocity (e.g., Ikeda and Izumi, 1990; Nanson and Knighton 1996; Murray and Paola, 2003). Similar bed shape changes can be expected around settled large wood.

In these root wad cases, the root wad of wood pieces facing upstream because the root lifts the wood piece from the bed when the wood piece flows into the lower water depth zone. This lifting by the root wad decreases the draft for the root wad section. The deposited wood piece tends to maintain the deposited state by reducing the projection area of the wood piece (e.g., Persson, 2000); hence, the stem section is immediately rotated to be parallel to the flow direction. We found that the angle of the deposited wood piece tends to depend on the flow discharge (**Figure 3.12**). As shown in **Table 4**, when the flow discharge is larger (cases 6 and 8), the angle between the streamwise direction and the stemwise direction of the wood piece becomes smaller than in the cases of a smaller discharge (cases 5 and 7). This result indicates that the change of the deposition angle is associated with the projection area affected by the flow discharge. However, the strength of the relationship between discharge and deposition angle caused by the projection area is unclear, and should be further analyzed.

Table 3.4 Averaged final stemwise angle of wood pieces (deg).

	Case 5	Case 6	Case 7	Case 8
Simulation	20.41	12.98	20.84	17.84
Experiment	24.40	15.25	32.75	8.50

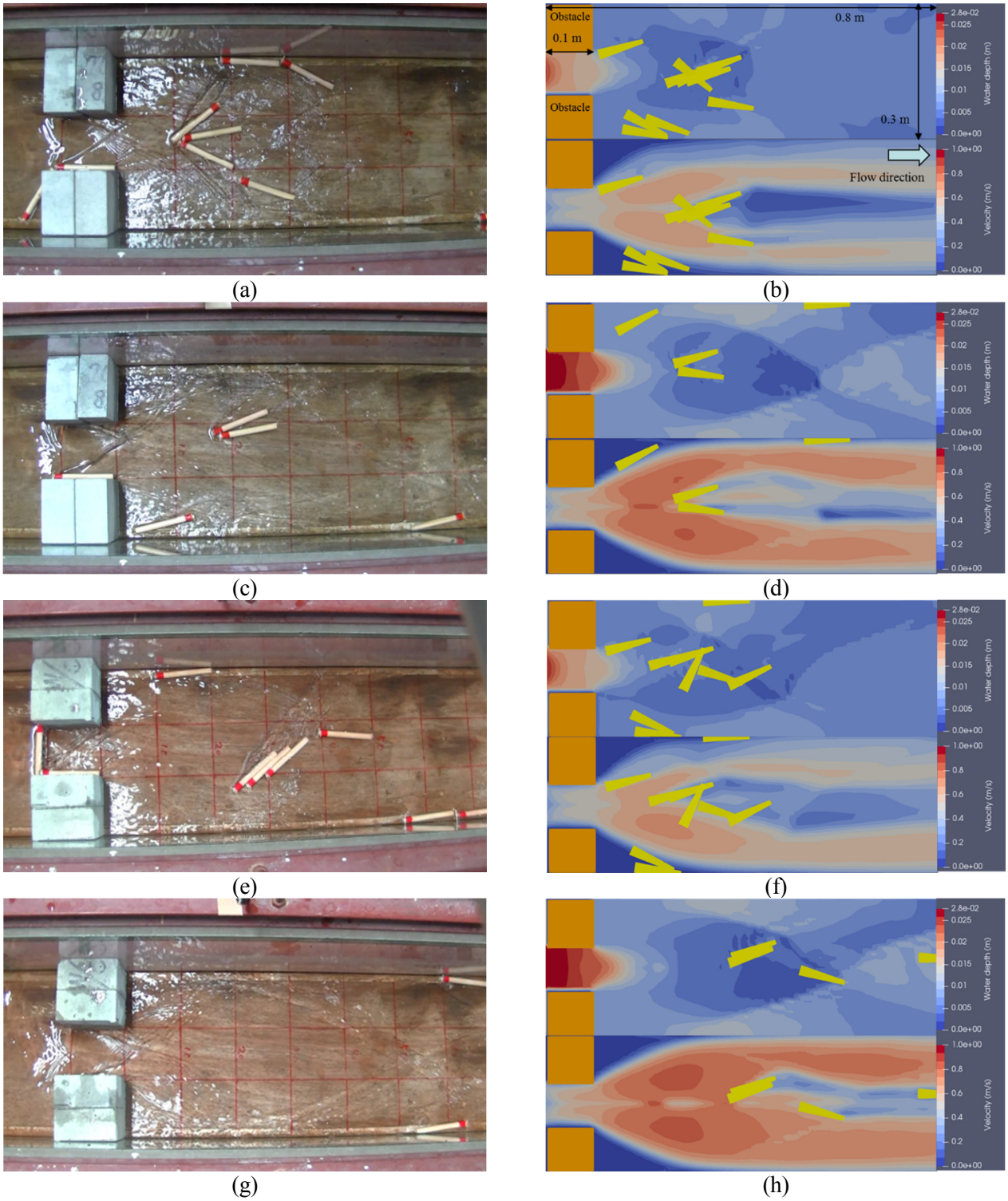

Figure 3.12 Experimental and simulation results for the deposition of wood piece with roots: experiments are (a) Case 5, (c) Case 6, (e) Case 7, (g) Case 8; simulations are (b) Case 5, (d) Case 6, (f) Case 7, (h) Case 8.

3.5 DISCUSSION

The results of the simulations and the experiments showed that in both presence and absence of the root wad, two deposition patterns were dominant: at the center of the flume and near the side walls (**Figure 3.13**).

The water depth upstream of the obstacle was larger (>1.2 cm) than the CDM (root: 1.2 cm, stem: 0.6 cm); hence, all wood pieces flowed downstream. After passing the obstacles, the water depth became smaller than the CDM, and the wood pieces touched the bed around the center of the flume. In this region, if the drag force is sufficient to drive the wood piece, some sliding motion occurs to the wood piece, and the wood piece may gradually flow downstream, rotating in its stemwise direction along with the flow direction because the increased flow velocity in the narrowing section enhances the drag force beside the obstacle (**Figure 3.13(a) and (b)**). If the wood piece has a root wad, the wood piece can easily become deposited after passing the obstacle because of the decreases of draft for wood motion at the root wad part, although the diameter of the root wad is larger than that of the stem. The wood piece with the root wad is easily subjected to a larger drag force because the root wad can lift the head of the wood piece from the flume bed because when the root first touches to the flume bed, the buoyancy of the wood piece decreases by the root wad decreasing draft (Merten et al., 2010; Shields and Alonso, 2012). After the wood piece comes into contact with the flume bed, the water depth around the wood piece increases as well as the velocity head because the wood piece affects the water flow. This increases both the buoyancy and the drag force; hence, the wood piece shifts toward the flume walls by rolling although the friction force in the stemwise direction remains larger (**Figure 13(c)**). Braudrick et al. (1997) also demonstrated that wood pieces are often deposited on the lateral margins (wall or bank) of the channel through the flume experiment, but their study neglected bed friction for wood motion. On the contrary, the present study shows that rolling motion is also one factor for deposition on the lateral margins. Moreover, downstream of the obstacle flow velocity has a component directed toward the wall as steering flow caused by the channel geometry near obstacle (**Figure 3.7**). This rolling occurs because the sliding friction (static $\mu = 0.4$ and kinematic $\mu = 0.05$) along the stemwise direction is much larger than along the lateral direction, in which the friction for wood motion is more governed by the roll friction ($\mu = 0.001$) than the sliding friction. Therefore, the wood piece cannot move in the stemwise direction, but can move in the lateral direction; thus, it moves toward a flume wall. The wood piece flows downstream if the drag force and the stemwise angle are larger (**Figure 3.13(d)**). If the wood

piece has no root wad, the wood piece flows more easily downstream because its draft for wood motion is larger than that of the wood piece with a root wad.

Such deposition pattern, which is parallel to the flow direction, was observed in the experiments (Welber et al., 2013; Bertoldi et al., 2014) and field observations (e.g., Piegay and Gurnell (1997) in the Drôme River (France) and Gurnell et al. (2000) and Bertoldi et al. (2013) in the Tagliamento River (Italy)). However, the rolling motion can be limited to occur within the artificial hydraulic structure, which has a rigid and flat channel bed, because in the natural system, most channel beds are not flat in shape due to the sediment (e.g., sand, gravel, and boulder).

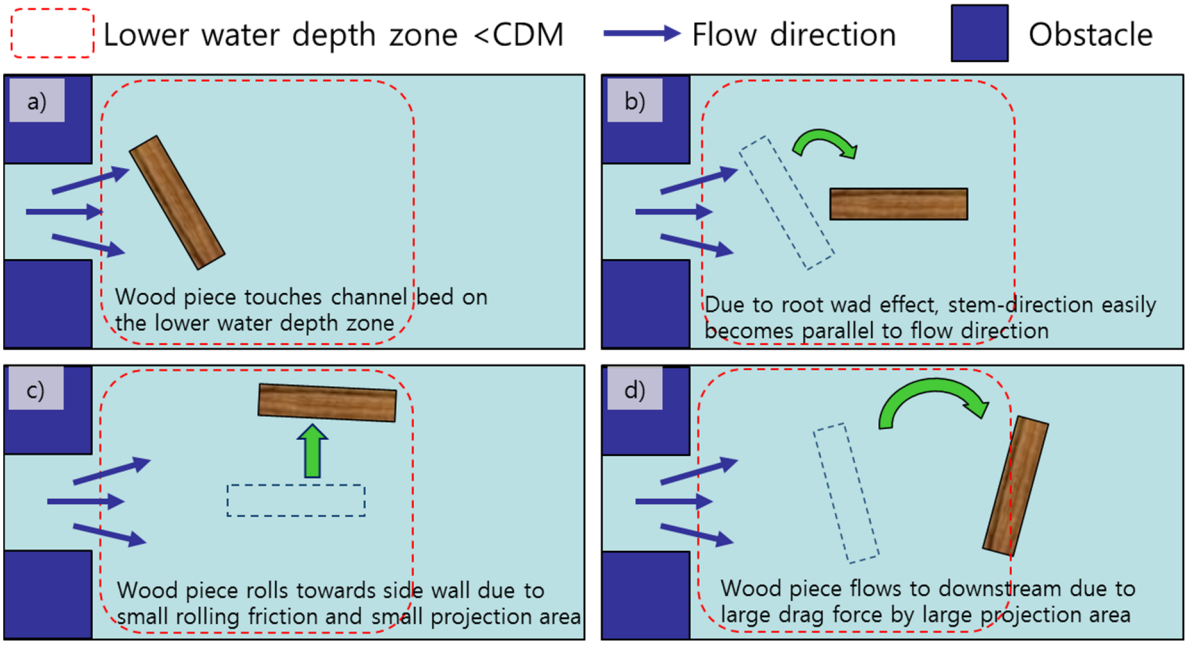

Figure 3.13 Schematics of large wood deposition patterns.

The results of both experiments and simulations showed that the presence of a root wad and the CDM had the most important roles in controlling deposition. Braudrick et al. (1997) also showed in their experiment that large wood was mainly deposited on the most shallow water depth. Davidson et al. (2015) demonstrated that root wad significantly decreased the travel distance. Braudrick and Grant (2000), Merten et al. (2010), and Schenk et al. (2014) showed that the presence of root wad is the most important determinant of both mobilization and travel distance.

In this study, the root wad particles were regarded as having a diameter larger than the trunk particles by a factor of 2. Thus, the root wad particles were more easily subjected to larger drag forces

because of the larger projection area than the trunk particles. However, the root wad particles weighed more than the trunk particles, which had the same density and, thus, had a higher CDM than the trunk particles. Moreover, we considered the change of the water depth caused by the root wad effect (**Figure 3.3**). Therefore, a larger number of wood pieces with a root wad could be deposited in both simulation and experiment results, and the proportion of the deposited wood with a root wad was clearly in a good agreement with the experimental results (**Figures 3.10 and 3.12**). Thus, we have shown that the root wad effect was reasonably reproduced by our numerical method, and wood motions could be accurately simulated using more diverse root wads (size and density). However, the root wad effect should be carefully refined using more detailed measurements. The present simulation model employed an empirical bed friction coefficient, and the bed friction coefficients of the root wad particle and trunk particle were tuned using a trial and error approach through a comparison with the experimental results. In addition, the motion of the wood pieces without the root wad showed only a floating motion. It also should be improved considering several parameters, such as secondary flow and projection area of the wood piece.

This simulation considered the random stemwise angle of the wood piece when supplied at the starting zone because the stemwise angle cannot be controlled prior to an obstacle. Therefore, the positions of the wood pieces and the number of wood pieces may show slightly different patterns between the simulations and the experiments. We even observed floating wood pieces near obstacle at upstream without flowing downstream through experiments maybe because that inconstant stemwise input angle caused different projection areas for the wood motion. If we make the stemwise angle of the wood pieces constant before they pass the obstacle in both the experiment and the simulation, both sets of results may show more regular patterns of wood piece deposition and advection.

The responses of the wood motion by the change of the channel slope showed an unclear pattern. The debris flow on the steep channel exhibited the active motion of the large wood because the steep channel can make gravity flow by higher potential energy (Carter 1975; Pierson., 1981; Costa., 1984; Takahashi., et al. 1992; Shieh., et al. 1996; Imran., et al. 2000; Shrestha et al., 2012). In this steep channel, the large wood can more easily move down than mild channel, such as an alluvial river, because of the gravity flow by potential energy. Such gravity flow was neglected herein because we used a mild channel slope on the simulation and the experiment. Therefore, the change of the channel slope should be larger to consider steep channel for the gravity effect in a further study.

Interestingly, the experiments in this study showed a simple jam formation by the deposited wood piece (**Figure 3.12**). This jam formation was clearly indicated when the flow discharge was smaller

(cases 5 and 7), then it can be accelerated by the first wood piece, which can interrupt the motion of subsequent wood pieces. Several researchers (e.g., Braudrick et al., 1997; Welber et al., 2013; Bertoldi et al., 2014; Bertoldi et al., 2015) also showed characteristics of jam formation by wood supply, bed elevation, and flow discharge through experiments. However, these studies only conducted the flume experiment, and many researchers are attempting to study this using the computational model for jam formation. The computational model is one of the challenging models to apply as a large wood dynamics model because we should consider many parameters, such as wood collusion, large wood shape, profile of the channel bed, and water flow. A large CPU time by the high-performance workstation is needed to reproduce a number of wood motions like the experiments for the jam formation. Therefore, our study would provide informative data for the development of the computational model considering the anisotropic bed friction, change of draft for wood motion, and root wad effect.

3.6 SUMARRY

This study developed a computational model for large wood deposition patterns in shallow flows considering the effect of a root wad based on laboratory experiments. We used the Nays2DH depth-averaged two-dimensional model of iRIC to simulate shallow flows. A newly developed large wood simulation model was combined with the shallow flow model. The laboratory tests were performed by changing several hydraulic parameters. In shallow water with a depth similar to the diameter of large wood, the root wad decreased the draft for wood motion (the depth at which large wood contacts the river bed) by lifting the head of large wood. The experimental results showed that the large wood tends to move toward the side walls and deposit on the bed after passing an obstacle. Computational results reasonably showed that the proposed coupling model reproduced the fundamental and physical aspects of the phenomena.

CHAPTER 4

LARGE WOOD DEPOSITION PATTERNS AND RESPONSES OF BED MORPHOLOGY IN A BRAIDED RIVER: COMPUTATIONAL HYDRODYNAMIC MODELING

4.1 INTRODUCTION

Along with water and sediment, rivers transport large pieces of wood (l/d > 10, l: length of wood, d: diameter of wood), and their deposition affects the river morphology by causing local scouring and the deposition of bed materials. Such large wood enhances habitat diversity in the river environment, and may initiate the formation of islands as a mid-channel bar in the bed morphology (Keller and Swanson, 1979; Nakamura and Swanson, 1993; Abbe and Montgomery, 1996; Gurnell and Petts, 2002; Swanson, 2003; van der Nat et al., 2003; Gurnell et al., 2005; Brooks et al., 2006; Cardenas, 2012). The deposition patterns of large wood can change in response to input processes, channel morphology, and hydrological parameters, including flood events (Montgomery 2003). Past research has shown that the relative influence of these factors changes along the river system (Gurnell et al., 2002; Collins et al., 2012; Keller and Swanson, 1979; Gurnell et al., 2000a; Gurnell, 2013), resulting in distinct downstream trends in the manner of large wood accumulation (Keller and Swanson, 1979; Gurnell et al., 1995; Marcus et al., 2002; Comiti et al., 2006). The ratio of the log length to channel width is a key parameter in determining large wood deposition patterns (Gurnell and Sweet, 1998); these patterns are also influenced by parameters such as the drag force, water level, bed friction, and presence of obstacles.

The factors that induce large wood deposition in a river can be primarily classified into the following patterns: 1) capture by an obstacle, 2) shallow flows, 3) wood jam, 4) bed morphology, and 5) wildlife. In this study, we focus on the riverbed deposition caused by shallow flows (e.g., Gurnell et al., 2005; Welber et al., 2013; Bertoldi et al., 2014) and bed morphology with wood jams (in braiding channel: Welber et al., 2013; Bertoldi et al., 2014). In particular, Welber et al. (2013) and Manners and Doyle (2008) note that the relative relevance of jams depends on the wood supply and transport mechanisms. While the spatial density of wood jams has been evaluated in various riverine contexts (Piegay and Gurnell, 1997; Gurnell et al., 2000b; Andreoli et al., 2007; Curran, 2010), limited data are available on the proportion of wood stored in jams, and direct comparisons are hindered by the use of

different definitions and metrics. In a survey carried out on the large, meandering Lower Roanoke River, Moulin et al. (2011) found that slightly more than 50% of wood was deposited in jams. Such large wood deposition is obviously associated with wood motion. The motion of large wood has been investigated by many researchers. For instance, Braudrick and Grant (2000) and Braudrick et al. (2001) laid out the basic framework for describing large wood mobility and entrainment in rivers. Their work allowed several researchers to undertake studies related to large wood transport dynamics (Haga et al., 2002; Bocchiola et al., 2002, 2006; Kramer and Wohl, 2017). These studies successfully predicted the relationship between the wood characteristics (wood size, flow discharge, area of river basin) and the hydrodynamic and resistance forces, and also extended the scope to transport systems. In similar cases, Manners et al. (2007) and Curran (2010) used these methodologies to clarify the large wood motion in streams. In studying the transport of large wood, the profile of the wood (size and presence of root wad) must first be considered (Gurnell and Sweet, 1998; Comiti et al., 2006). A piece of large wood may consist of trunk, branch, and/or root wad sections. Among those, the trunk and root plate are the major components of large wood, and they actively affect its motion. Large wood deposition is especially sensitive to the characteristics/properties of the root wad (Braudrick and Grant, 2000), because this part increases the friction with the bed and reduces the large wood's buoyancy.

The increase in experimental and observational research (e.g., Haga et al., 2002; Gurnell, 2003; Moulin and Piégay, 2004; Wohl and Goode, 2008; Seo and Nakamura, 2009; Cadol and Wohl, 2010; Curran, 2010; Iroume et al., 2010; Merten et al., 2010; Mao et al., 2013; Kramer and Wohl, 2017; Thévenet et al., 1998; Lassettre et al., 2008), as well as the enhanced importance of predicting and managing the stability of wood pieces and jams (Richmond and Fausch, 1995; Dixon and Sear, 2014, Davidson, et al., 2015), has led to the active development of numerical models of large wood transport. For instance, hydrodynamic models of rivers have been combined with large wood transport models, such as the Iber-wood two-dimensional (2D) hydrodynamic model (Ruiz-Villanueva et al., 2014a, 2014b, 2016) and the NaysCUBE (Kimura, 2012) three-dimensional (3D) Reynolds-averaged Navier–Stokes (RANS) model (Kitazono et al., 2016; Kimura and Kitazono, 2017). Both of these models address wood transport using a Lagrangian method, whereby the water flow is coupled with the wood transport at every time step. The Iber-wood model considers the wood shape to be a simple cylinder. In contrast, the NaysCUBE large wood model applies a particle-based method to consider the impinging motion of large wood using a discrete element method (DEM). These studies have clarified the mechanism of large wood motion in deep water flows (where the water depth is greater than the wood diameter), and reproduce the large wood motion well. However, these models overlook the bed

morphology and large wood deposition factors such as the root wad effect and anisotropic bed friction, although the effect of the wood on bed morphology is most relevant when being transported in shallow flows. Thus, clarifying such phenomena by coupling floating and deposition motions with bed morphology is crucial in enhancing our understanding of large wood behavior in rivers as well as the role of large wood floating advection on the permanent bed.

The main aim of this study, therefore, is to develop a numerical method for simulating the transport of large wood together with the hydrodynamics in the braiding channel while considering the root wad effect under various empirically determined hydrologic parameters (flow discharge and channel slope) (Welber et al., 2013; Bertoldi et al., 2014). This paper presents the newly developed numerical model, which can precisely simulate the behavior of large wood. We use a 2D depth-averaged flow model to evaluate the flow phase. The flow model is developed based on Nays2DH iRIC (Shimizu et al., 2014; International River Interface Cooperative, 2018), which is an Eulerian model for calculating the water flow and bed morphology in generalized coordinates. A Lagrange-type large wood model is developed and combined with Nays2DH. The applicability of the present model is discussed through a comparison with experimental results.

4.2 COMPUTATIONAL SETUP AND METHODOLOGY

4.2.1 Profile of Large Wood and Computational Domain

We used a 2D plane numerical solver, which was developed based on Nays2DH in iRIC, to simulate the flows. We employed the third-order total variation diminishing-monotonic upstream centered scheme for conservation laws (TVD-MUSCL) to solve the advection term, the central scheme for the Reynolds stress term, and a zero-equation-type turbulence model based on the shallow flow equations. Ashida and Michiue's model (1972) was used to estimate the bedload flux, and incorporated a bank collapse model that considers the angle of repose (=0.6 rad) (Hasegawa, 1985). The Manning roughness coefficient was estimated as 0.01457 $s/m^{1/3}$ from the averaged sediment diameter of 0.73 mm, which was determined using the Manning–Strickler formula. The total simulation time was set to be 1080 min, the same as the experimental time (Bertoldi et al., 2014). To reduce the simulation time, we used a parallelization method (OpenMP). This 2D plane numerical solver is described in further detail on the Nays2DH and iRIC website (Shimizu et al., 2014; International River Interface Cooperative, 2018). In this paper, we only describe the particle method for wood motion. The main parameters for water flow and wood motion are listed in **Table 4.1**.

Table 4.1 Main parameters used for simulations.

Parameter	Value	Parameter	Value
Computational domain (Flume size)	11 m × 1.7 m	Diameter of wood piece	0.003 m
Bed slope	0.013 (m/m)	Root wad diameter	0.01 m = (0.008 + 0.012)/2
Grid length (=Δx and Δy)	0.02 m (550×85)	Density of wood piece	670 kg/m^3
Input discharge	0.00126 m^3/s	Drag-force coefficient	1 (as sphere shape)
Critical draft for wood motion (stem particle)	0.0017 m	Critical draft for wood motion (root wad particle)	0.0061 m
Manning roughness coefficient	0.0145 s/m$^{1/3}$	Static bed friction coefficient	0.5
Critical shear stress	0.034	Kinematic bed friction coefficient	0.2
Grain size	0.73 mm	Rolling bed friction coefficient	0.075
Length of wood piece	0.08 m	Radius for wood jam resolution	0.08 m
Angle of repose for bed collapse model	0.6 [rad]	Eddy viscosity for zero equation	0.4

To generate the braiding channel, we first conducted a 20-h bed morphology simulation from an initial flat bed with a constant slope. To generate the instabilities required to form the brading channel, we used a random variation input flow discharge ($\pm$1%) at the upstream inlet as an input boundary condition.

This process resulted in the bed profile shown in **Figure 4.1(a)**, which has a braiding channel (Total Braiding Index: 3.6). In all simulation cases, we employed the bed shown in **Figure 4.1** as an initial condition. This bed has a similar Total Braiding Index (called the Braiding Index in Bertoldi et al., 2014) as in the experiments (C1–C3 have a Total Braiding Index of approximately 3.5, 3.65, and 4.7, respectively; see **Figure 4.12(a)**). **Table 4.2** describes wood supplement scenarios that can be considered as three different cases (C1–C3). Wood pieces are inserted at the wood supply points in the wood supply zone, as shown **Figure 4.1(c)**. The radius of the wood supply points is 0.025 m and wood pieces are randomly placed within this radius. The initial stemwise angle of the wood pieces is set at random. The wood supply zone generates 10 wood pieces at each time step (each wood supply point generates one wood piece). In cases C2 and C3, the wood supply process is repeated (two times for C2 and three times for C3). The time interval for the repeated wood supply is 3 s, thus preventing the formation of a wood jam at the wood supply points (Bertoldi et al., 2014).

Table 4.2 Simulation cases based on previous experiments (Bertoldi et al., 2014).

Case	C1		C2		C3	
	Hours		Hours		Hours	
	0-6	6-18	0-6	6-18	0-6	6-18
Wood input rate (logs/h)	60	40	120	80	180	120
Input frequency (cohorts/h)	6	4	6	4	6	4
Cohort size (logs)	10	10	20	20	30	30
Logs with root wads (%)	60	40	60	40	60	40

In Bertoldi's experiments, the root wad was modeled as a "cross" shape. The deposition of this cross shape varied depending on the root wad (**Figure 4.1(e)**). When the root wad diameter was 0.012 m, the wood piece was deposited with a "+" shape; 2) when the root wad diameter was 0.008 m (perpendicular height), the wood piece was deposited with a "×" shape. Thus, as we wish to consider both deposition types, we used an averaged root wad particle diameter of 0.01 m.

In addition, we defined the radius for wood jam resolution as 0.08 m, because when a wood piece rotates without advection, it can touch other pieces of wood that are within 0.08 m (**Figure 4.1(f)**).

To reduce the CPU time, this study neglected the collision of wood pieces, because we wish to calculate large numbers of wood pieces (>500). Thus, wood pieces can be deposited at the same place, i.e., overlapping. This limitation increases the number of stored wood pieces by a factor two. The other simulation conditions are identical to Bertoldi's experimental conditions (see Bertoldi et al., 2014). Hereafter, we refer to "large wood," "wood pieces," and "wood particles" as the target wood in the natural system, the wood bodies in the simulations and experiments, and parts of the wood pieces in the simulations, respectively.

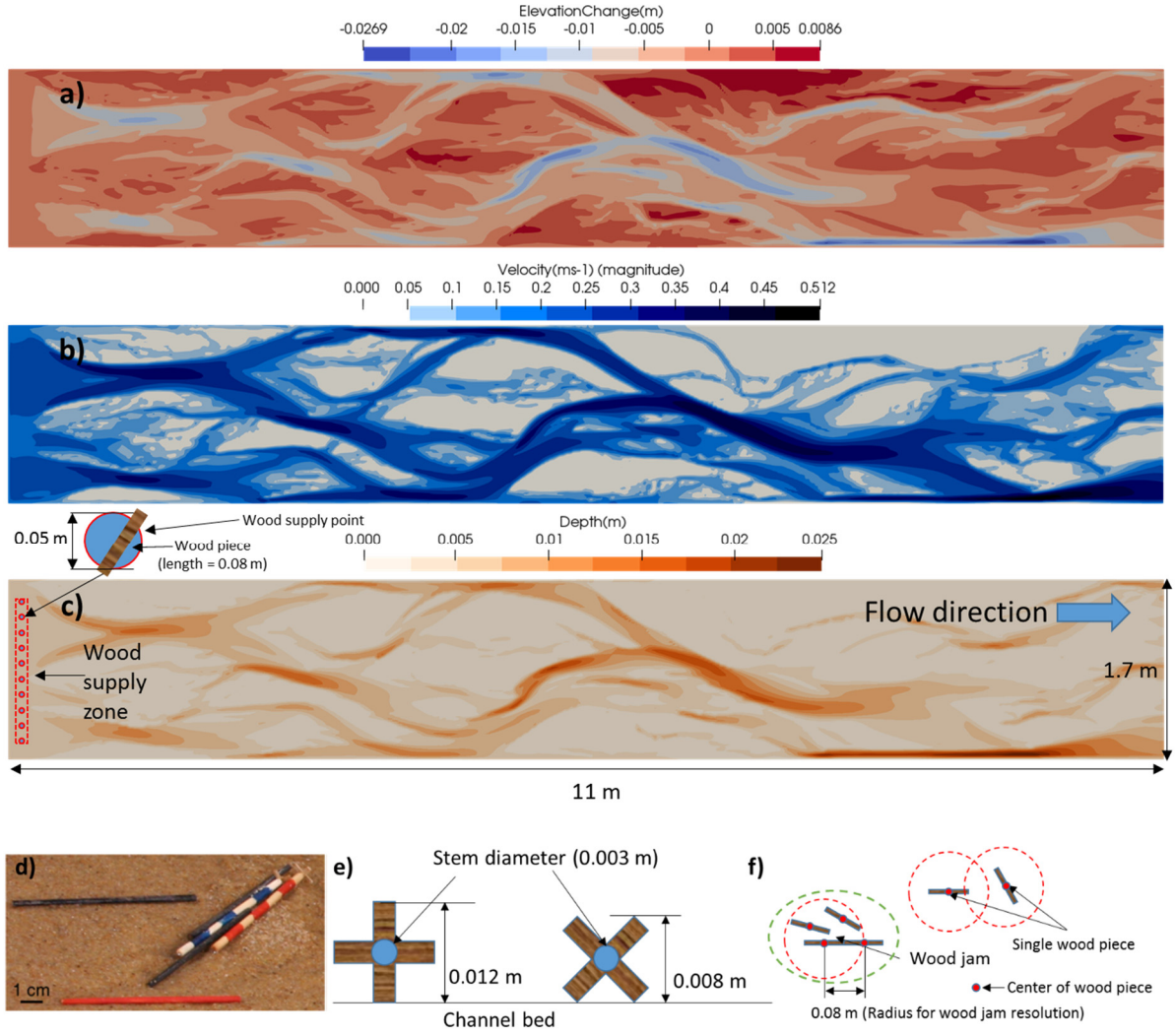

Figure 4.1 Preprocessed computational domain and wood piece. a) changed elevation (m); b) velocity magnitude (m^3/s); c) water depth (m) d) wood piece in experiment; e) two deposition types of root wad; f) definition of radius for wood jam resolution in this study.

4.2.2 Particle Method for Modeling Large Wood Dynamics

In the present large wood model, one piece of large wood is expressed as a set of connected particles. Each particle in a piece of wood is advected by the following equation (Kimura, 2012; Kitazono et al., 2016; Kimura and Kitazono, 2017):

$$\sigma A_t d_p^3 \frac{d\mathbf{u_p}}{dt} = \begin{cases} \mathbf{F_d} + \mathbf{F_{wa}} + \mathbf{F_{am}} - \mathbf{F_{bed}}, \mathbf{F_d} + \mathbf{F_{wa}} + \mathbf{F_{am}} > \mathbf{F_{bed}} \\ 0, \mathbf{F_d} + \mathbf{F_{wa}} + \mathbf{F_{am}} \leq \mathbf{F_{bed}} \end{cases} \tag{4-1}$$

where

$$\mathbf{F_d} = \frac{1}{2} C_D \rho \lambda_{A-sub} \overline{A_p} |\mathbf{u} - \mathbf{u_p}| (\mathbf{u} - \mathbf{u_p}) \tag{4-2}$$

$$\mathbf{F_{wa}} = \rho \lambda_{V-sub} A_t d_p^3 \left(\frac{d\mathbf{u}}{dt} \right) \tag{4-3}$$

$$\mathbf{F_{am}} = C_M \rho \lambda_{V-sub} A_t d_p^3 \left(\frac{d\mathbf{u}}{dt} - \frac{d\mathbf{u_p}}{dt} \right) \tag{4-4}$$

$$\mathbf{F_{bed}} = \begin{cases} 0, h > h_c \\ \mu A_t d_p^3 (\sigma - \lambda_{V-sub} \rho) g, h \leq h_c \end{cases} \tag{4-5}$$

where $\overline{A_p}$ is the projected particle area in the relative flow direction; ρ is the water density; σ is the large wood density; C_M is an additional mass coefficient (C_M= 0.5 was used in this work); C_D is a drag coefficient; A_t is a 3D shape coefficient (π/6 in this work); d is the diameter of the particle sphere; $\mathbf{u}$ is the fluid velocity around the sphere; $\mathbf{u_p}$ is the velocity of the sphere; t is time; and g is gravitational acceleration. $\mathbf{F_{bed}}$ is the bed friction force vector; λ_{A-sub} is the submerged area ratio; λ_{V-sub} is the submerged volume ratio; $\mathbf{F_d}$ is the drag force; $\mathbf{F_{wa}}$is the effect of the acceleration of the surrounding water; $\mathbf{F_{am}}$ is the effect of the water's added mass; and h_c is the critical draft for wood motion (see **Figure 4.4**) when calculating the sliding friction (**Equations** (4-1) - (4-5)).

The bed friction coefficient (μ) in **Equation** (1-5), which is an anisotropic friction coefficient, changes with the direction of the water flow that the wood particle passes and the stemwise angle of the wood piece (see **Figure 4.3**). The *x* and *y* components of μ are expressed as:

$$\mu_x = \sqrt{f_t \cos\theta - f_n \sin\theta} \tag{4-6}$$

$$\mu_y = \sqrt{f_t \sin\theta + f_n \cos\theta} \tag{4-7}$$

where θ is the stemwise angle of the wood piece (θ = 0 indicates the *x*-axis direction). For the Eulerian momentum equation for water flows, the following drag force terms are caused by the large wood:

$$\mathbf{F_{DW}} = -\frac{1}{2}\rho C_D \frac{1}{hA_{cell}} \sum_{n=1}^{N_{cell}} A_{pn} \left|\mathbf{u}^n - \mathbf{u}_\mathbf{p}^n\right| \left(\mathbf{u}^n - \mathbf{u}_\mathbf{p}^n\right) \tag{4-8}$$

where A_{pn} is the projected area of a particle toward the flow direction; A_{cell} is the area of a grid cell; n is the number of particles in the wood piece; and N_{cell} is the number of stored wood particles in the cell. This numerical analysis includes motion that is indirectly changed by alterations to the water due to adjacent wood pieces, because such wood particles are modeled as causing a drag force and changing the water depth.

As we have neglected the collision of wood particles, several wood pieces can be deposited at the same place, i.e., overlapping, which can result in excessive drag force. To avoid such a numerical limitation, we define the maximum drag force. If the total A_{pn} in one grid cell exceeds A_{cell} during the summation process of **Equation** (4-8), the summation is stopped.

4.2.3 Projection Area for Drag Force depending on The Angle Between Flow Direction and Stemwise Direction

The drag force can be changed by the flow direction, because the projection area of the particles is changed by the angle between the relative flow direction and stemwise direction. The drag force on the wood particles increases when the angle is large, increasing the motion velocity. In contrast, the drag force on the wood particles decreases when the angle is small, decreasing the velocity. If we neglect the projection area, the influence of the flow velocity is too strong, making the wood motion monotonous. For example, the wood motion suggests that the wood only flows downstream, with few wood flows near the river margin (side wall). Therefore, it is important to reproduce the motion of the wood. In the simulations, to consider the projected angle (ϕ) between the relative flow direction and stemwise direction, we define the unit vector in the stemwise direction ($\boldsymbol{S_t} = (\cos\theta, \sin\theta)$) and the unit vector in the relative flow direction ($\boldsymbol{S_s} = \left(\frac{u_x}{|\mathbf{u}|}, \frac{u_y}{|\mathbf{u}|}\right)$) as shown in **Figure 4.2(a)**. We can then calculate the angle between the flow direction and stemwise direction using $\boldsymbol{S_s}$ and $\boldsymbol{S_t}$ as:

$$\cos\phi = \boldsymbol{S_s} \cdot \boldsymbol{S_t} = \frac{u_x \cos\theta + u_y \sin\theta}{|\mathbf{u}|},\ \sin\phi\ | = \sqrt{1 - \cos^2\phi},\ |\mathbf{u}| = \sqrt{u_x^2 + u_y^2} \tag{4-9}$$

where ϕ is the angle between the stemwise direction and flow direction (if ϕ=0, the stemwise direction is the same as the flow direction); u_x and u_y are components of flow velocity in the *x* and *y* directions; and $|\mathbf{u}|$ is the absolute flow velocity.

We calculate the projection area of stem particles as:

$$\overline{A_p} = A_p|\sin\phi|,\ A_p = d_p^2 A_2 \tag{4-10}$$

where $\overline{A_p}$ is the projection area and A_p is the particle area (see **Figure 4.2(b)**).

It is important to consider the first and last particles in a wood piece, because such particles are simultaneously exposed to water flow in the streamwise and lateral directions. The calculation of their projection areas is illustrated in **Figure 4.2(c)–(f)**. To consider the first wood particle (**Figure 4.2(c),(d)**), we have:

$$\overline{A_{p1}} = A_{p1}(|\sin\phi| + \max[\cos\phi, 0]) \tag{4-11}$$

where $\overline{A_{p1}}$ is the projected area of the first particle and A_{p1} is the original area of the first particle. The projection area of the last wood particle (**Figure 4.2 (e),(f)**) is given by:

$$\overline{A_{pl}} = A_{pl}(|\sin\phi| + \max[-\cos\phi, 0]) \tag{4-12}$$

where $\overline{A_{pl}}$ is the projected area of the last wood particle and $A_{pl}$is the original area of the last wood particle.

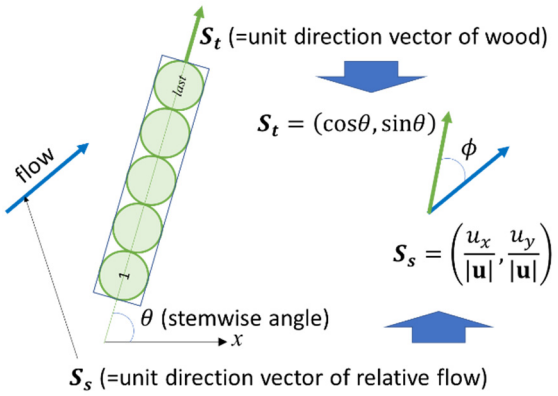

(a) angle between stemwise direction and flow direction

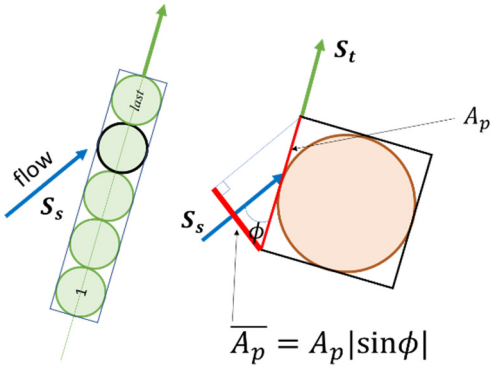

(b) projection area for stem part

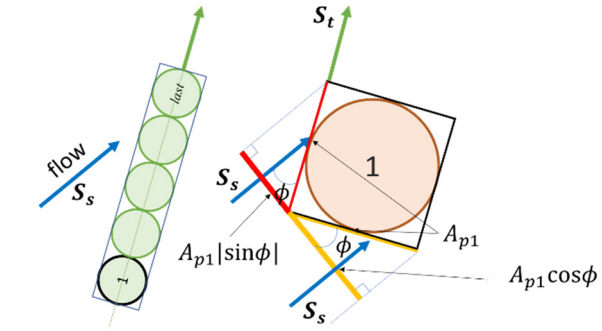

If ϕ is an acute angle ($-\pi/2 \leqq \phi \leqq \pi/2$): $\cos\phi \geq 0$

$\overline{A_{p1}} = A_{p1}(|\sin\phi| + \cos\phi)$, if $\cos\phi \geq 0$

(c) projection area for first particle (acute ϕ)

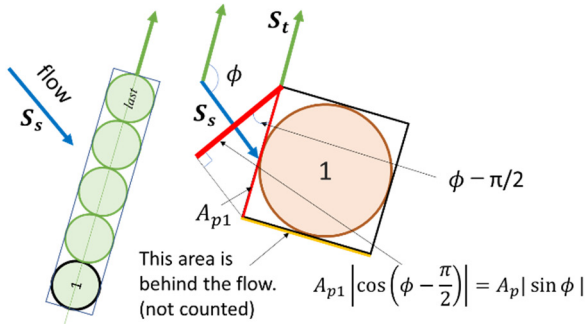

If ϕ is an obtuse angle ($-\pi/2 > \phi$ or $\phi > \pi/2$) :$\cos\phi < 0$

$\overline{A_{p1}} = A_p|\sin\phi|$, if $\cos\phi < 0$

(d) projection area for first particle (obtuse ϕ)

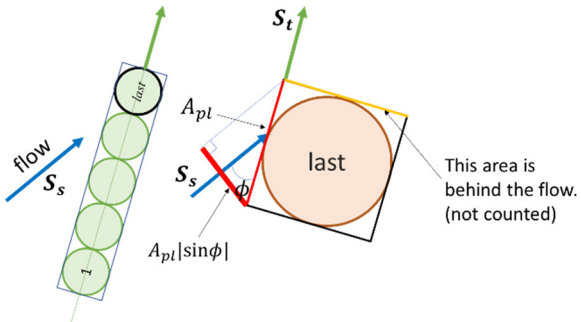

If ϕ is an acute angle($-\pi/2 \leqq \phi \leqq \pi/2$): $\cos\phi \geq 0$

$\overline{A_{pl}} = A_{pl}|\sin\phi|$, if $\cos\phi \geq 0$

(e) projection area for last particle (acute ϕ)

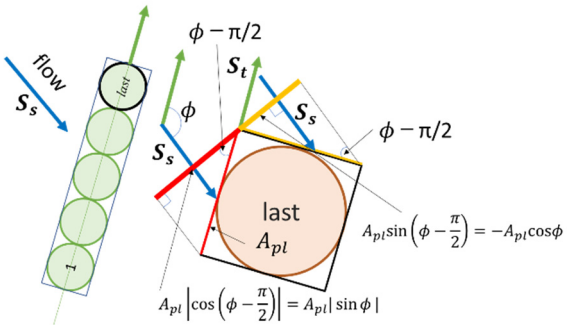

If ϕ is an obtuse angle ($-\pi/2 > \phi$ or $\phi > \pi/2$): $\cos\phi < 0$

$\overline{A_{pl}} = A_{pl}(|\sin\phi| - A_{pl}\cos\phi)$, if $\cos\phi < 0$

(f) projection area for last particle (obtuse ϕ)

Figure 4.2 Diagram for calculation of projection area.

4.2.4 Anisotropic Bed Friction Coefficient Affected by Angle Between Flow Direction and Stemwise Direction

In general, the static bed friction coefficient between the wood piece used to construct the flume bed and the wood piece flowing down the river is approximately 0.4–0.6 (Ambrose and Tripeny, 2011). The bed friction coefficient under submerged conditions is uncertain; however, it may be expected to decrease because the water surface plays role of lubricating the wood motion. Therefore, we conducted trials to compare the experimental results with the simulation output (Kang et al. 2018), and adjusted the bed friction coefficients accordingly (see **Table 4.1**). The static bed friction coefficient (μ_s) refers to the friction coefficient when a wood piece is deposited, and the kinematic bed friction coefficient (μ_k) refers to the friction coefficient when a wood piece is moving.

These coefficients are mainly activated in the stemwise direction of the wood piece. If the movement is in the direction perpendicular to the trunk direction, the wood piece rolls and the friction becomes much smaller. The rolling friction is small (μ_r <0.1), and so the stemwise bed friction coefficient (f_t) is much larger than the lateral bed friction coefficient (f_n). Thus, the stemwise velocity of the wood particles is subjected to more deceleration than the lateral stemwise velocity. As a result, the wood piece tends to move in the lateral stemwise direction. This anisotropic bed friction model reproduces the natural wood motion better than isotropic bed friction, indicating the importance of considering such anisotropic friction.

The anisotropic bed friction coefficient is affected by the angle between the flow direction and stemwise direction, as shown in **Figure 4.3**. To consider this angle, we employed the unit vector in the lateral stemwise direction ($\boldsymbol{S_n}(-\sin\theta, \cos\theta)$) and the unit vector in the lateral wood piece direction ($\boldsymbol{S_p}$). $\boldsymbol{S_p}$ is given by:

$$\boldsymbol{S_p} = \frac{1}{\sqrt{u_{px}^2 + u_{py}^2}}(u_{px}, u_{py}) \tag{4-13}$$

where u_{px} and u_{py} denote the particle velocity in the *x* and *y* directions, respectively.

The angle between the stemwise direction and particle pass direction (ϕ_t), and the angle between the lateral stemwise direction and particle pass direction (ϕ_n), are calculated as:

$$\cos\phi_t = \boldsymbol{S_p} \cdot \boldsymbol{S_t} = \frac{u_{px}\cos\theta + u_{py}\sin\theta}{\sqrt{u_{px}^2+u_{py}^2}},\ \cos\phi_n = \boldsymbol{S_p} \cdot \boldsymbol{S_n} = \frac{-u_{px}\sin\theta + u_{py}\cos\theta}{\sqrt{u_{px}^2+u_{py}^2}} \tag{4-14}$$

Using both ϕ_t and ϕ_n, we can estimate the bed friction coefficients (f_t, f_n) at both angles as:

$$f_t = -\mu_{s\ or\ k} \cdot \frac{\cos\phi_t}{|\cos\phi_t|},\ f_n = -\mu_r \cdot \frac{\cos\phi_n}{|\cos\phi_n|} \tag{4-15}$$

where the direction (sign) of both friction coefficients (f_t, f_n) is determined by the unit vector in the lateral wood piece direction ($\boldsymbol{S_p}$), as shown in **Figure 4.3(b), (c)**.

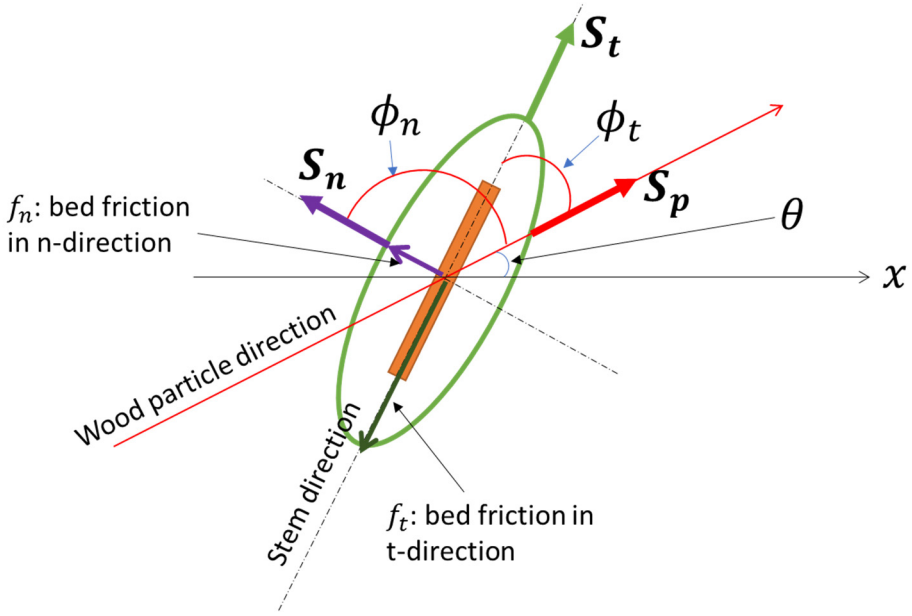

(a) basic domain

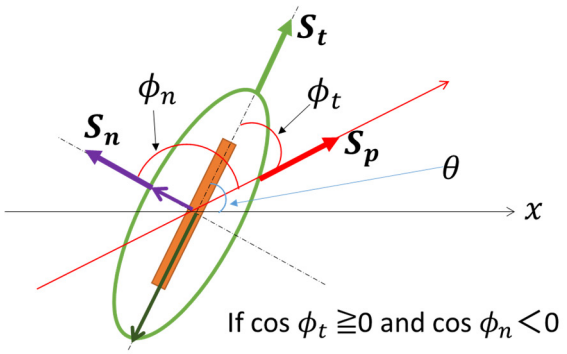

(b) type of positive (+) particle pass direction to x-axis

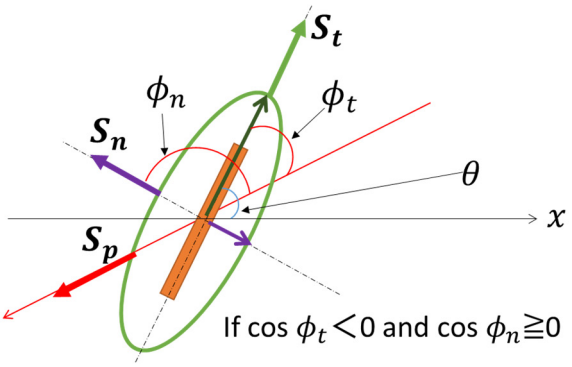

(c) type of negative (-) particle pass direction to x-axis

Figure 4.3 Diagram of anisotropic bed friction coefficient affected by angle between flow direction and stemwise direction.

4.2.5 Buoyancy and Critical Draft for Wood Motion

An important factor affecting large wood deposition is the buoyancy of the wood piece. Braudrick et al. (1997) estimated the draft for a cylindrical wood piece, but their method is inappropriate for the spherical particles used in the present model. Moreover, this study considers the difference in the submerged volume of each particle due to changes in flow depth and the presence of root wad. The inclination of settled wood pieces based on the root wad shape is also taken into account to evaluate the buoyancy. If the buoyancy is less than the weight of the wood piece, the wood piece is deposited. If the buoyancy is greater than the gravitational force, the wood piece floats. When the density of the wood piece is less than the water density, the draft of the wood piece is determined by the balance between the buoyancy and the weight. The point at which the water depth is the same as the draft is called the critical draft for wood motion (CDM). In other words, the CDM is the minimum depth in which wood does not touch the bed. The CDM (h_c) is the same as the draft in the floating condition, which can be obtained as follows.

The maximum unsubmerged volume of wood is calculated as:

$$V_e = \frac{B_w - W_d}{\rho_w},\ W_d = \frac{4}{3}\pi d^3 \rho_d,\ B_w = \frac{3}{4}\pi d^3 \rho_w \tag{4-16}$$

where W_d is the weight of a wood particle; B_w is the buoyancy under the totally submerged condition; and V_e is the unsubmerged volume of a particle under the totally floating condition, as shown in **Figure 4.4**.

From **Equation** (4-16), we can obtain the maximum unsubmerged volume V_e and the submerged volume V_s using:

$$V_s = \int_{r_c}^{\beta_c} f(y_d)^2 \pi dy_d,\ f(y_d) = +\sqrt{r_c^2 - y_d^2} = \pi \int_{r_c}^{\beta_c} r_c^2 - y_d^2 dy_d = \pi \left[r_c^3 y_d - \frac{1}{3} y_d^3 \right]_{r_c}^{\beta_c}$$
$$= \pi \left[\left(r_c^2 \beta_c - \frac{1}{3}\beta_c^3 \right) - \left(r_c^3 - \frac{1}{3} r_c^3 \right) \right] \tag{4-17}$$

where y_d is the coordinate in the depthwise direction, as shown **Figure 4.4**; β_c is the water level from the center of the particle; and r_c is particle radius along the depthwise axis.

From **Equation**s (4-17) and (4-18), the unsubmerged volume V_e can be written as:

$$V_e = V_t - V_s,\ V_t = \frac{4}{3}\pi d_p^3 \tag{4-18}$$

where V_s is the submerged volume of the wood particle and V_t is the wood particle volume. By solving these equations iteratively, we can obtain the CDM.

In the case of a root wad particle, we assume its diameter to be larger than that of a trunk particle. The drag force of a root wad particle is larger than that of a trunk particle because of its larger projection area, and the weight of the root wad particle is greater than that of a trunk particle because of its larger volume under the same density. Thus, root wad particles can have a lower velocity under the same water depth and flow velocity.

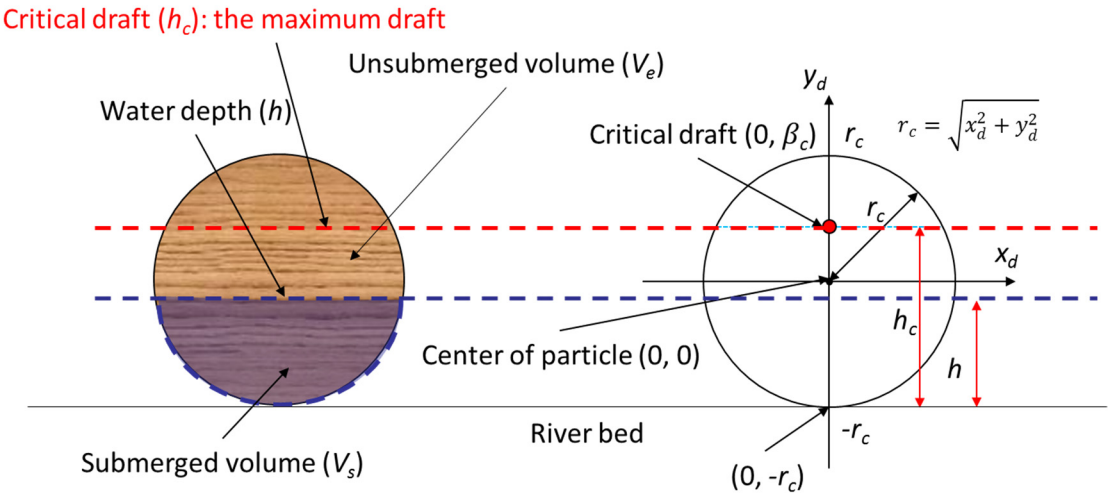

Figure 4.4 CDM concept. (left) structure of submerged wood particle for each particle; (right) geometry of critical draft for wood motion for each particle.

4.2.6 Change of Water Depth under Root Wad Effect

When the root wad of a large wood piece becomes deposited on the bed at a water depth that is less than the CDM, the root wad effect decreases the submerged water depth at each particle, as shown in **Figure 4.5(c)**. The root wad lifts one edge of the trunk up from the river bed, decreasing the submerged volume of the wood piece. The influence of buoyancy decrease accordingly, and the force normal to the bed increases compared to the case of a wood piece with no root wad. In the computation, we first determine the CDM of each particle in the wood piece, and then, if the averaged CDM of the wood particles is lower than the present water depth (**Figure 4.5(b)**), modify the water depth under the root wad effect as:

$$h_{sn}^{i} = h_s - h_r L_a \frac{i}{n},\ h_r = (h_p \times L_d)/L_a,\ L_a = \sqrt{h_p^2 + L_d^2} \tag{4-19}$$

where h_s is water depth (constant over the area of interest); h_p is half the difference between the trunk diameter and root wad diameter; L_d is the trunk length; L_a is the projection length of the trunk length

into the river bed; h_r is the height lift due to the root wad effect; h_{sn}^i is the calculated water depth due to the root wad effect for each particle; and n is the total number of particles in the wood piece.

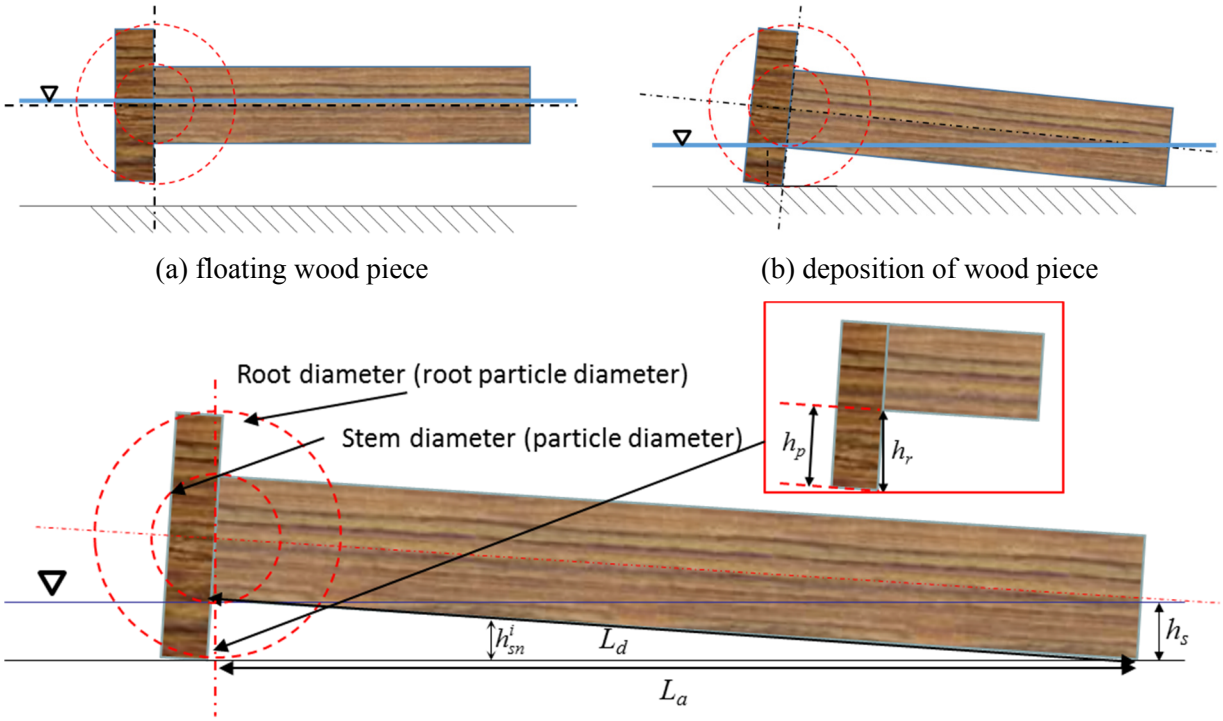

(a) floating wood piece

(b) deposition of wood piece

(c) change in water depth.

Figure 4.5 Change in submerged depth due to root effect.

4.2.7 Changes to The Bed Caused by Large Wood Deposition

Deposited large wood can be partially buried by the sediment in the river bed. Berg et al. (1998) and Wohl and Goode (2008) suggested that burial is the most important determinant of wood motion when the bed morphology is considered. A greater force is required to move a partially buried wood piece than an exposed piece (Brooks et al., 2006). However, the opposite process occurs in rivers, and buried wood pieces may become unburied through channel meandering (Latterell and Naiman, 2007), which can result in mobilization. Therefore, we consider large wood deposition with a burial process for each wood particle. However, the mobilization force for partially buried wood pieces is neglected because it is too complicated to consider the wood motion and deposition.

To consider the burial and remobilization by sediment flux and bed morphology, we employed the area occupation ratio of one particle against one grid cell (σ_p) as shown in **Figure 4.6(a)**. When a wood particle is deposited on the cell area (A_{cell}), the occupation ratio (σ_p) increases. This increases the

bed elevation, because the wood particle area (A_p) decreases the vacant space in the cell. If the deposited wood particle deviates from this cell area (A_{cell}), the bed elevation decreases by the volume ratio equivalent to the wood particle area; this change in bed elevation (Δr_1) is shown in **Figure 4.6(b)**. For this bed elevation change, we used a modified Exner equation:

$$\frac{q_{bx}(x) - q_{bx}(x+\Delta x)}{\Delta x} + \frac{q_{by}(y) - q_{by}(y+\Delta y)}{\Delta y} = \frac{\Delta \zeta}{\Delta t}(1-\lambda_s)(1-\Sigma\sigma_p) \tag{4-20}$$

where $q_{bx}$and q_{by}denote the sediment discharge flux in the x and y directions, respectively; Δt is the time step; $\Delta\zeta$ is the bed elevation change at Δt; Δx and Δy are the cell lengths in the x and y directions, respectively; λ_s is the soil porosity (=0.4); and σ_p can be written as:

$$\sigma_p = \frac{A_p}{\Delta x \Delta y} = \frac{A_p}{A_{cell}} \tag{4-21}$$

When the wood particle is remobilized, the bed elevation changes by the occupation ratio of the remobilized particle. For example, we assume that deposited particles 1 and 2 are placed in one grid cell, as shown in **Figure 4.6(b)**, and then particle 1 moves out of the cell. At that time, the bed elevation changes by:

$$\Delta\zeta_{2new} = \Delta\zeta_{2old} - \Delta r_1,\ \Delta r_1 = \frac{A_{p1}\Delta\zeta_1}{A_{cell}} \tag{4-23}$$

where $\Delta\zeta_{2new}$ is the bed elevation with only particle 2; $\Delta\zeta_{2old}$ is the original bed elevation with particles 1 and 2; Δr_1 is the occupation ratio of particle 1; ζ_1 is the bed elevation before the wood particle is remobilized; and A_{p1} is the diameter of the wood particle before remobilization. Note that this modified Exner equation does not consider the precise volume of a sphere, and so the bed change produced by wood particle motion is slightly overestimated.

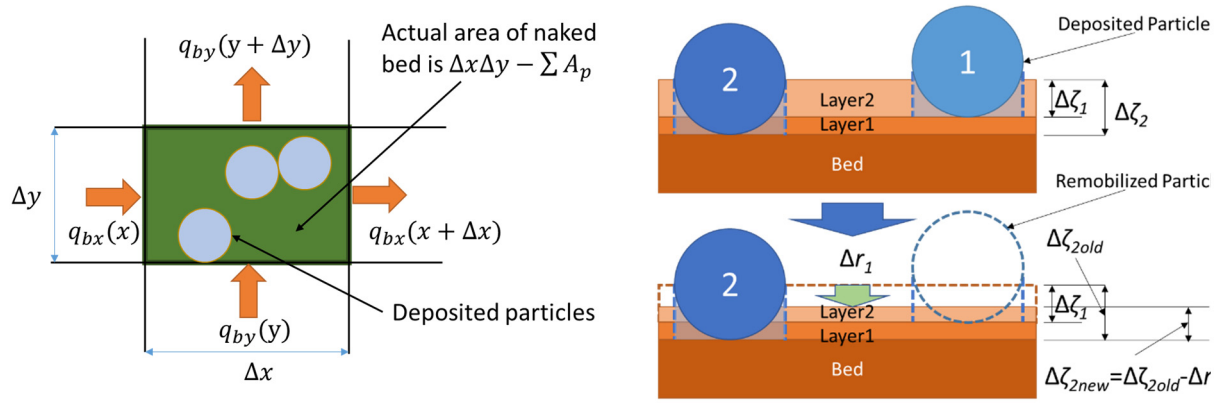

(a) diagram for cell area and particle (b) buried particle in the bed

Figure 4.6 Bed changing by large wood particle deposition.

4.2.8 Interaction between Water Flow and Wood Particles

In this solver, the calculation schemes for the water flow and the wood particles are completely different. In the present large wood model, one wood piece is expressed as connected particles, which are driven by a Lagrangian method. Therefore, a method is required for modeling the interaction between the grid-based water flow and the particle-based wood motion. For this purpose, we use linear interpolation, as shown in **Figure 4.7(c)**, to obtain the flow velocity and water depth at the target particle. If each particle is located at an arbitrary position, the distances (l_a, l_b) from a standard grid point (G_1) to the center of the particle are defined, and these are used for the interpolation. The edge length of each cell is set to 1 on the generalized curvilinear coordinate system. The value at the particle center (G_{ip}) is then calculated with reference to the values at four surrounding grid points using:

$$G_{ip} = \frac{\sum_{k=1}^{4} \frac{G_k}{A_k}}{\sum_{k=1}^{4} \frac{1}{A_k}} \tag{4-24}$$

$$A_1 = l_a \times l_b, A_2 = l_a \times (1 - l_b), A_3 = (1 - l_a) \times (1 - l_b), A_4 = (1 - l_a) \times l_b \tag{4-25}$$

where G_{ip} is the interpolated value at the particle center; $G_1 - G_4$ are values at the grid nodes; A_1–A_4 are the weighting areas (see **Figure 4.7**); l_a, and l_b are the lengths from grid point G1; and k is the index for the grid point. If $G_1 = G_{ip}$, the values of l_a and l_b are 0.

Through this interpolation, we obtain the interpolated flow velocity and water depth values at each particle location from a grid node point. **Figure 4.7(a)** shows the process of calculating the interaction between the water flow and wood motion. The specific calculation procedure is as follows.

1) Water flow is calculated using the 2D shallow flow model based on Nays2DH.

2) The submerged volume of the wood particle is calculated considering buoyancy and CDM. If the wood particle has a root wad component, the CDM and submerged volume are recalculated.

3) The bed friction acting on the wood particle is determined considering the CDM: if the wood particle is located in water that is deeper than the CDM, no bed friction is applied to the wood motion. When the wood is moving, the kinematic and rolling friction should be considered if the wood is touching the bed.

4) The wood particle velocity is calculated considering the drag force. If the water depth is less than the CDM, the bed friction is considered.

5) From the particle velocity calculation, the advection of each particle is calculated independently without any connection force for one time step (Δt), and then the new location of the gravitational center of the wood pieces is determined by averaging the new particle locations. The

rotation angle of each particle with respect to the new gravitational center is also averaged and the angular velocity of the wood is determined (see **Figure 4.7(b)**).

6) The position of each particle is rearranged into the shape of a wood piece considering the averaged rotation angle and the center of gravity (see **Figure 4.7(b)**).

7) From the rearranged wood piece, the drag force of the flow is calculated at each particle of the wood piece, and then applied to the water flow calculation in the next time step.

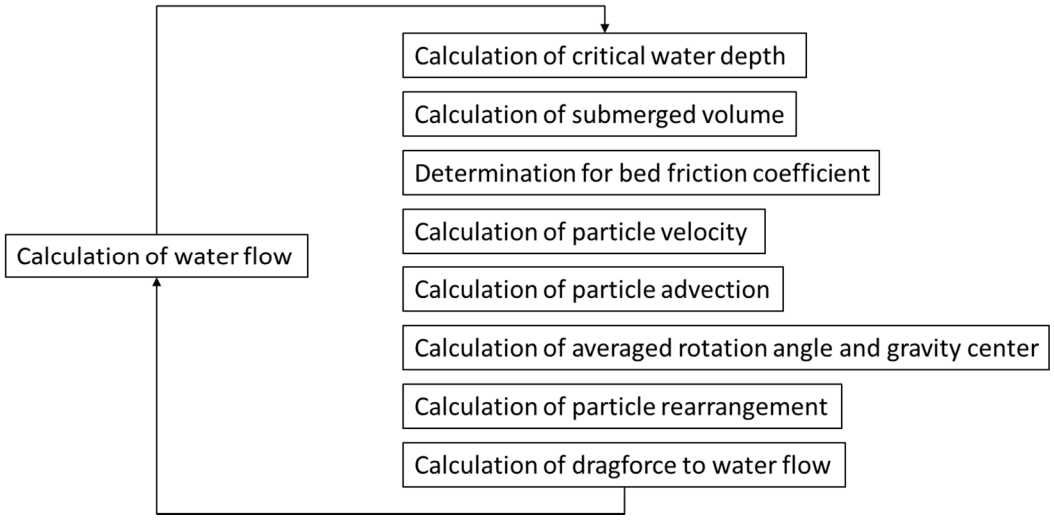

(a) algorithm for calculating the coupled dynamics of water flow and wood motion

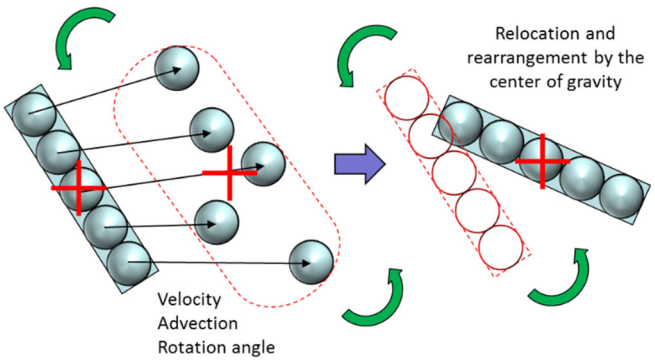

(b) concept of wood motion model (cross shape indicates the center of gravity

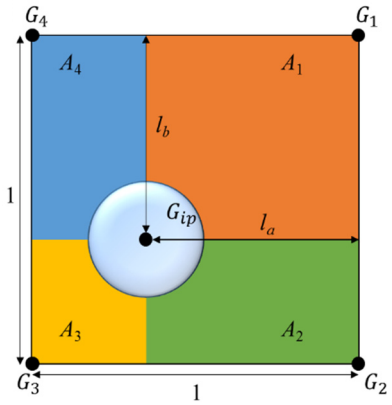

(c) linear interpolation for the wood particle characterization using grid points

Figure 4.7 Calculation processing for motion of large wood.

4.3 SIMULATION RESULTS

4.3.1 Final Patterns in Channel Bed and Wood Deposition

Figure 4.8 shows contours of the water depth and stored wood pieces in the computational domain. Blue and red indicate wood pieces with and without root wad, respectively. To clearly distinguish the root part, the width of this part is slightly thicker in **Figure 4.8**. The wood piece deposition patterns observed in the present simulation are generally in good agreement with experimental results (Welber et al., 2013; Bertoldi et al., 2014) and related observations (Piegay et al., 1999; Gurnell et al., 2002; Wyzga and Zawiejska, 2005). In all cases (C1–C3 and no wood case), a number of channel threads developed in the domain (**Figure 4.8**), because channel migration and bar formation were actively developed during the simulation. Thalweg is also generated in the middle of the domain; in particular, **Figures 4.8(b)** and **(d)** show largely developed thalweg (see **Figure 4.12**).

A number of stored wood pieces can be observed in the upstream area of **Figure 4.8**. These stored wood pieces are longitudinally deposited towards the downstream direction. A wood jam tends to form near the mid-channel bar, and many high-density wood jams formed upstream of the entrance to the bar, where a bifurcation occurs. A large number of isolated wood pieces can be observed in the downstream region. This deposition pattern implies that wood piece deposition is affected by bed morphology in terms of bar deformation and changes in discharge distribution (Bertoldi, 2012). In addition, the concave outer bank is the main deposition sector, affecting the jam formation through wood deposition as much as the entrance to the mid-channel bar (Bertoldi et al., 2013; Bertoldi et al., 2014). Jams often developed from a single wood piece being deposited parallel to the flow direction because of additional orthogonal wood pieces (Abbe and Montgomery, 1996). This model neglects wood particle collision, but the drag force of the water flow is activated by wood particles. Thus, large wood jams can decrease the flow velocity, causing further wood pieces to be captured by the jam. This kind of deposition can be observed in the simulation results (**Figure 4.8(a)–(c)**).

The simulation results show the deposition of wood pieces with and without a root wad (**Figure 4.8**). The stemwise direction of the deposited wood pieces is almost parallel to the flow direction in the upstream region (Braudrick and Grant, 2001; Welber et al., 2013). These wood pieces are mostly deposited near the thread channel bank along the water flow direction, and their stemwise directions run parallel to the water flow. This is because, in areas of lower water depth (<CDM) such as bar crests, deposited wood pieces can be affected by the drag force of water flow, although the buoyancy of the wood pieces is too weak for wood motion. There are two types of motion here. The first type concerns wood pieces with no root wad. These tend to rotate, becoming perpendicular to the direction of water

flow, because of the small rolling friction. If such a wood piece then touches the bed in areas of lower water depth (bar surface), which have less drag force, it is deposited and settles. The wood piece may move again if the depth becomes greater than the CDM or the drag force becomes larger than the bed friction. The second type of motion is essentially controlled by root wad, which remarkably affects the wood motion. When the root wad touches the bed, the trunk of the wood piece rotates to become parallel to the flow direction. The root wad then tends to head upstream. If the drag force is sufficient to drive the wood piece, some sliding motion occurs. As the diameter of the root wad is larger than that of the trunk, a wood piece with root wad is easily subjected to a larger drag force. Such deposition patterns have been observed in experiments (Welber et al., 2013; Bertoldi et al., 2014) and field observations (e.g., Piegay and Gurnell (1997) in the Drôme River (France); Gurnell et al. (2000) and Bertoldi et al. (2013) in the Tagliamento River (Italy)).

Such phenomena can also be explained by considering the response to energy dissipation. At low shear rates (absence of root wad and small rolling friction), the wood piece is perpendicularly driven depending on the angle between the stemwise direction and flow direction under the small rolling friction. When the shear rate increases above some critical value (e.g., CDM and large drag force), the wood pieces orients themselves in the state corresponding to the least dissipation energy, where the stemwise direction is parallel to the flow direction (e.g., Persson, 2000).

The simulation results exhibit three types of wood deposition patterns that have been observed in experiments (Abbe and Montgomery, 1996, 2003; Welber et al., 2013; Bertoldi et al., 2014): 1) “jam on a mid-channel bar” in **Figure 4.9(a)**; 2) “wood scattered across bars” in **Figure 4.9(c)**; 3) “wood accumulation at bar head” in **Figure 4.9(e)** (see Welber et al., 2013). Most of the simulated wood deposition patterns were similar to those in **Figure 4.9(b)** and **(f)**, and wood was often scattered across bars (**Figure 4.9(c)**). To explain this deposition pattern, Gurnell et al. (2005) postulated that wood pieces tend to accumulate around island margins, in areas of lower water depth, resulting in wood pieces being scattered across bars. Abbe and Montgomery (2003) also explained that small jams and single wood pieces can be deposited across the bar surfaces.

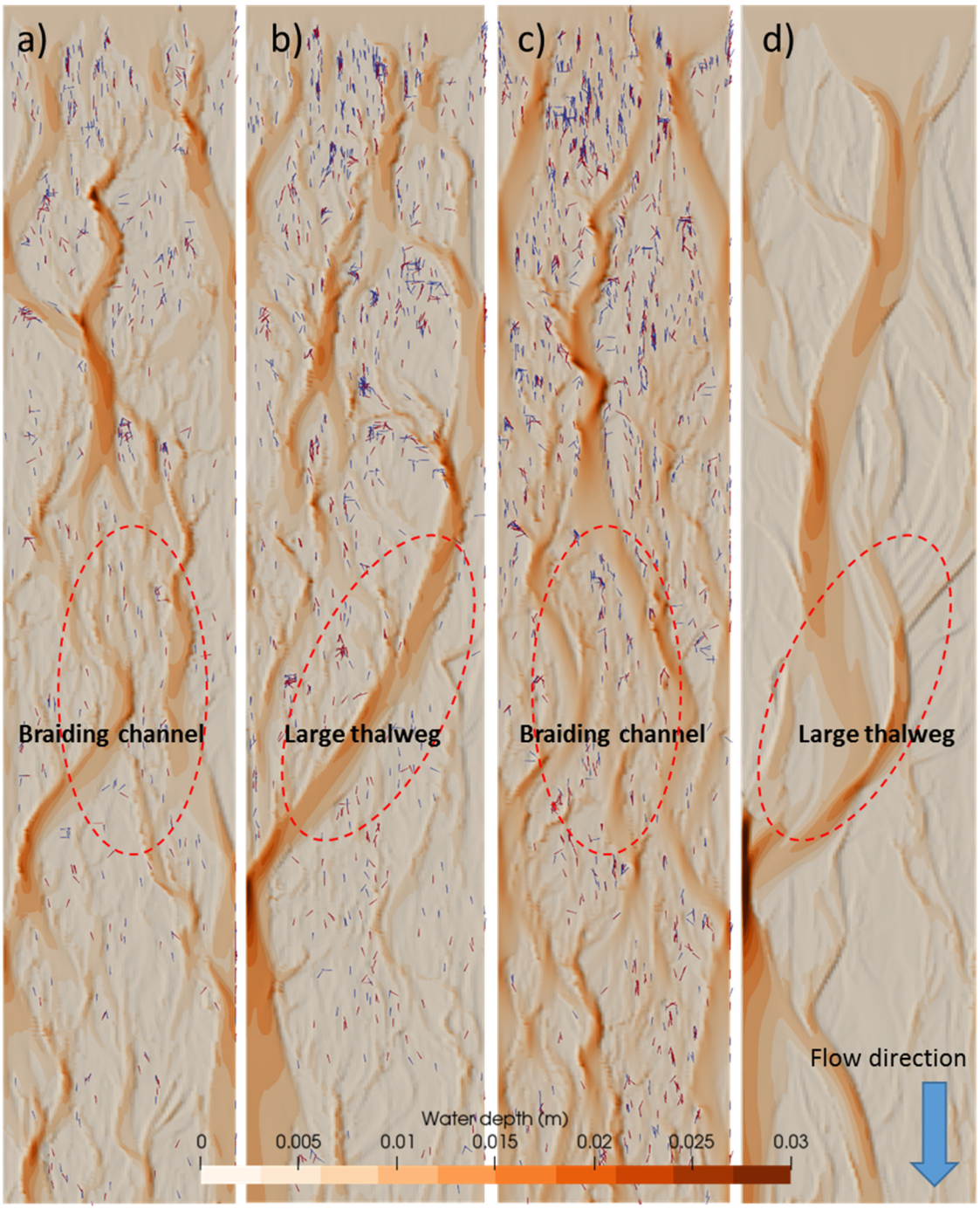

Figure 4.8 Final water depth in simulation results. a) C1; b) C2; c) C3; d) no wood case.

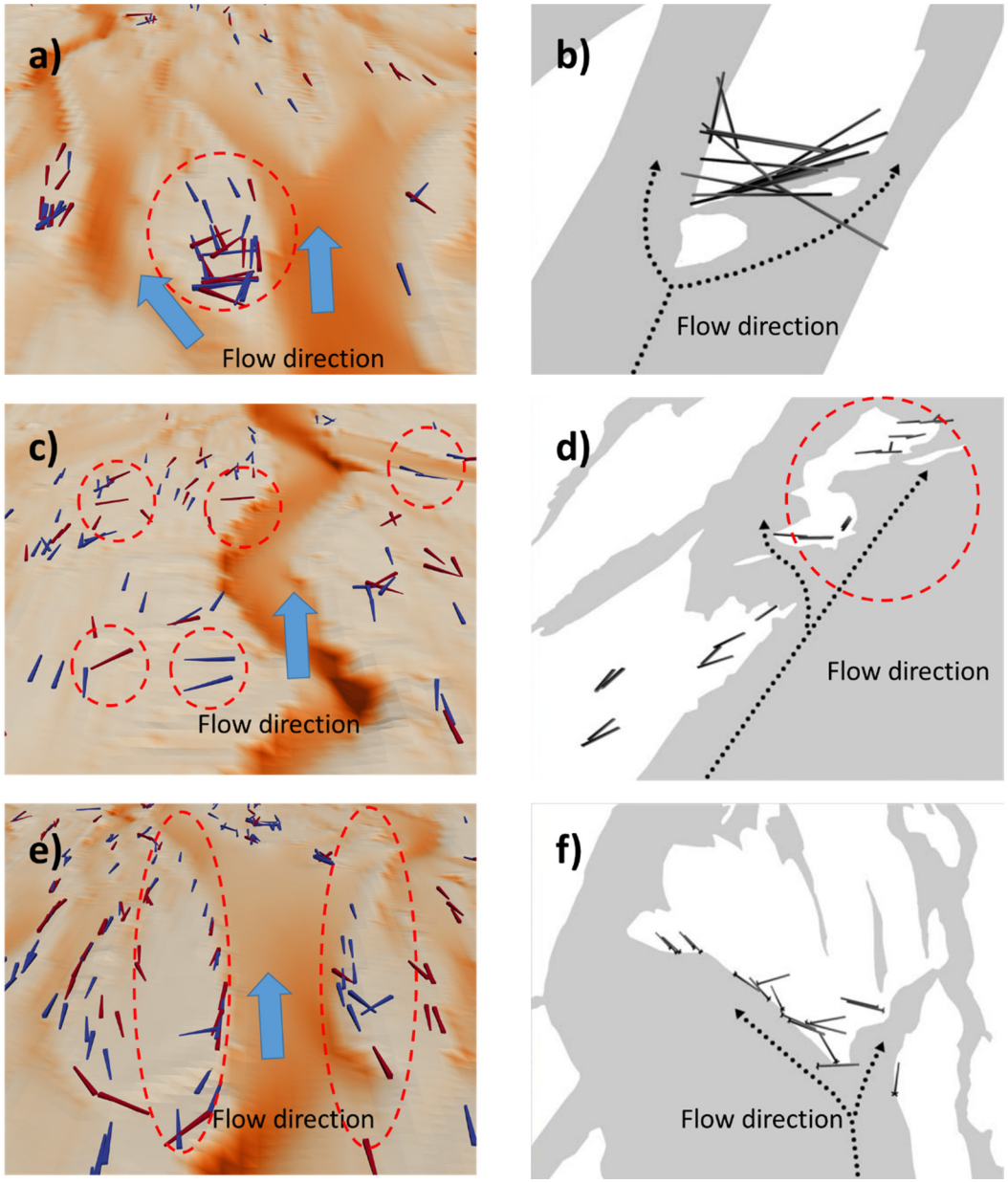

Figure 4.9 Sample for comparison between simulation result and experimental result (Welber et al., 2013). a) jam on a mid-channel bar (Sim., C1); b) jam on a mid-channel bar (Exp.); c) wood scattered across bars (Sim., C1); d) wood scattered across bars (Exp.); e) wood accumulation at bar head (Sim., C3); f) wood accumulation at bar head (Exp.); Sim. is simulation result and Exp. is experimental result.

4.3.2 Temporal Changes in Wood Piece Storage

The temporal changes in the number of stored wood pieces are shown in **Figure 4.10(a)** (simulation) and **11(b)** (experimental results: Bertoldi et al., 2014). In the experimental results, C1 and C2 exhibit similar changes in the number of stored wood pieces over time, whereas C3 shows a steady increase in stored wood. However, all simulation results indicate that the number of stored wood pieces steadily increases over time. Even though the root wad proportion changes after 6 h, decreasing the slope of the temporal change, the total number of wood pieces continues to increase. These results differ from the experimental cases (**Figure 4.10(b)**). One reason is the absence of wood piece collision dynamics in the simulations. In the experiments (**Figure 4.10(b)**), when a number of wood pieces are deposited in the flume, the wood piece stability for deposition increases and the occupation ratio of the area where wood pieces are deposited decreases. Thus, it is more difficult for wood pieces arriving in that area later to be deposited. **Figure 4.10(b)** also shows the tendency of narrow variations, particularly after the change in root wad proportion (from 6 h). In contrast, the simulations allow wood pieces to be deposited at the same place (see **Figures 4.9** and **4.10**). Moreover, **Figure 4.10(c)** shows that the simulated output to input (OI) ratio is lower than in the experimental case (**Figure 4.10(d)**). In particular, the experimental OI ratio increases after the wood supply and root wad ratio decrease. However, the simulated OI ratio does not exhibit the same tendency. This may be caused by the overlapping of wood pieces in the simulation. Even though the OI ratio is different in the simulations and experiments, the temporal changes in root wad proportion display a similar tendency (**Figure 4.10(e),(f)**). This means that our model gives a reasonable reproduction of both deposition types in the presence of root wad.

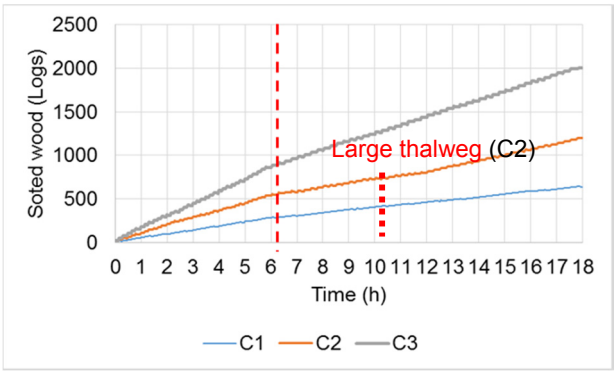

(a) the number of stored wood (Sim.)

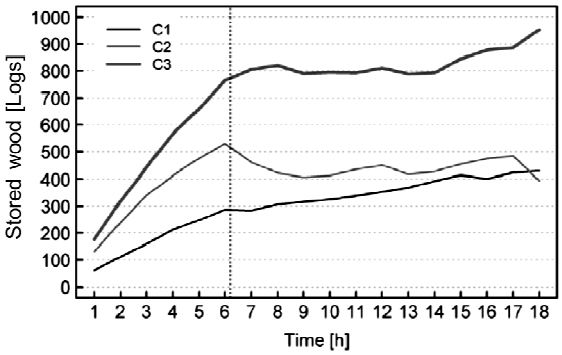

(b) the number of stored wood (Exp.)

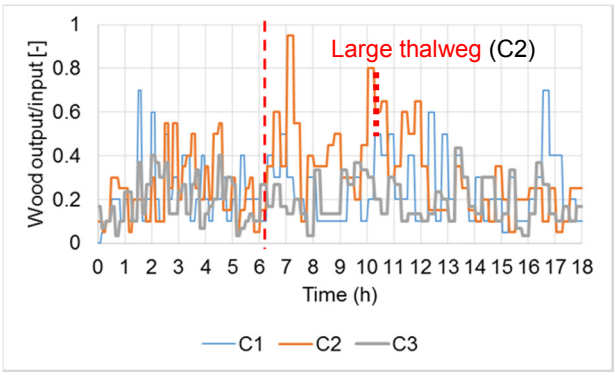

(c) wood OI ratio (Sim.)

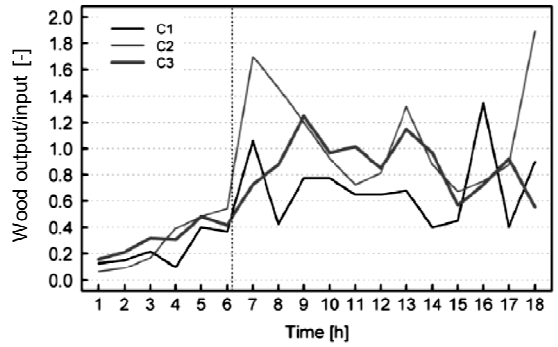

(d) wood OI ratio (Exp.)

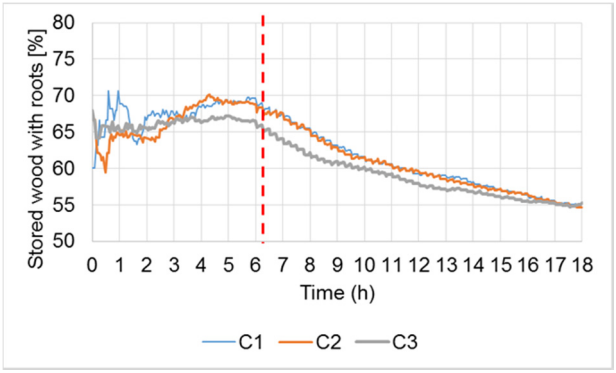

(e) wood with root wad proportion (Sim.)

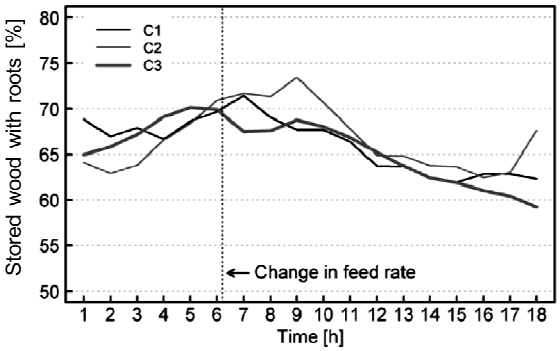

(f) wood this root wad proportion (Exp.)

Figure 4.10 Temporal changes in stored wood profiles (Experimental result is Bertoldi et al., 2014).

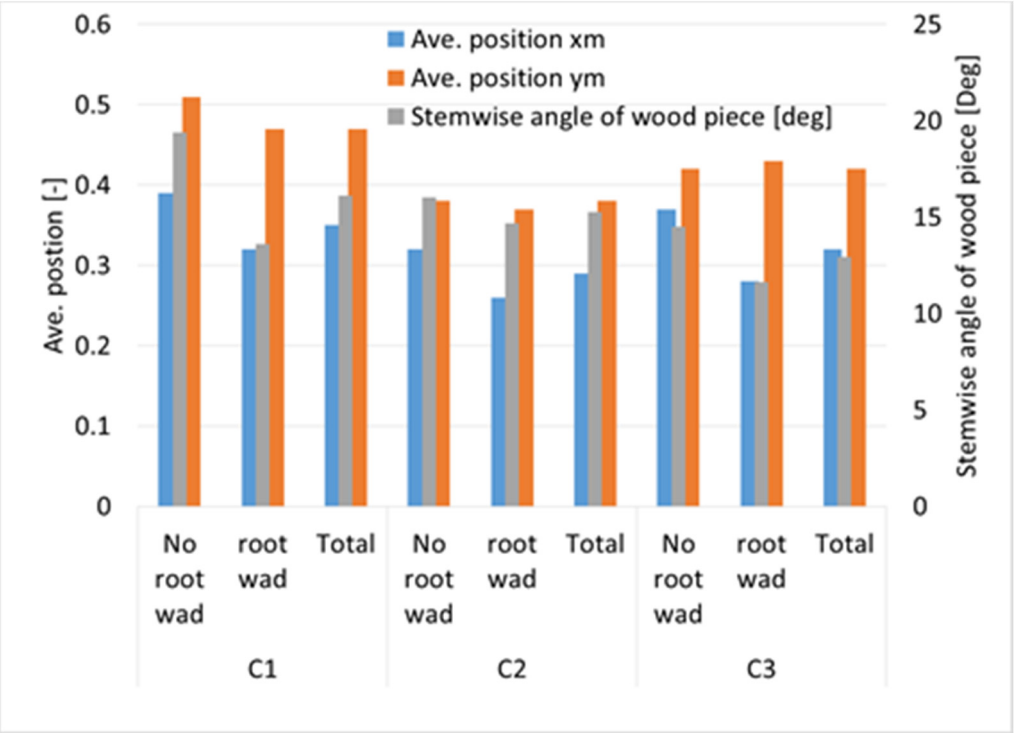

Figure 4.11 Averaged final profile of wood storage in simulation. (Ave. position xc is $\boldsymbol{x_m}$; Ave. position yc is $\boldsymbol{y_m}$).

Figure 4.11 shows the final profile of the wood deposition pattern. To quantify the wood deposition pattern, we calculated the normalized averaged position (x_m and y_m) of the wood pieces. From each center position (x_c, y_c) of a wood piece in the x_c- and y_c-directions (x_c: streamwise direction, y_c: lateral direction), the x_m and y_m components were calculated by averaging x_c and y_c and then normalizing these values according to the flume scale in the x_c-direction (11 m) and y_c-direction (1.7 m). These x_m and y_m values allowed us to identify the characteristics of wood deposition in relation to wood supply and the root wad effect. If x_m = 0, all of the wood pieces were deposited at the upstream inlet; if x_m = 1, all of the wood pieces were deposited at the downstream end. If y_m = 0, all of the wood pieces were deposited on the centerline; if y_m is close to 1, the wood pieces were deposited near a wall.

From **Figure 4.11**, we can see that C1 gives the largest average values of x_c and y_c, because fewer wood pieces are placed in the domain, so the possibility of interaction between wood pieces is lower. Hence, the proportion of single wood piece is the largest among C1–C3 (see **Figures 4.14(a), (c), (e)**). C1 also produces a greater stemwise angle, which is against the *x*-axis, than in cases C2 and C3. This is because fewer wood pieces are deposited upstream than in the other cases, whereas C2 and C3 deposit

more wood pieces upstream through the process of capture by developed wood jams (Abbe and Montgomery, 2003). These wood jams cause localized erosion, resulting in thread channels being generated near the jams. As the wood pieces are exposed to water flow in the thread channels, their stemwise angle changes to become parallel to the flow direction (e.g., Welber et al., 2013; Bertoldi et al., 2014; Piegay and Gurnell, 1997; Gurnell et al., 2000; Bertoldi et al., 2013). The root wad has a strong effect on the large wood motion (**Figure 4.11**). In other words, the presence of a root wad increases the wood stability and enhances the likelihood of deposition. Bertoldi et al. (2014) noted that wood pieces without root wad exhibited significant motion during the experiment. In addition, **Figure 4.10(e)** shows the high proportion of stored wood in the presence of root wad. This root wad effect has been observed by several researchers (e.g., Abbe and Montgomery, 1996; Gurnell et al., 2002; Manners and Doyle, 2008; Davidson et al., 2015).

The computational and experimental results for the bed morphology can be compared using the active braiding index (ABI) and bed relief index (BRI) for channel quantification (see Bertoldi et al. 2014; Kang et al. 2018), as shown in **Figure 4.12**. As the number of thread channels increases, ABI increases, and vice versa. As the thalweg depth increases, the BRI value increases. The experimental (Bertoldi et al., 2014) range of the braiding index is 3.5–5, as shown in **Figure 4.12(a)**. In the simulations, the ABI ranged from 2.7–4.5. However, the simulation with no wood produced a narrower range of 2–2.7. **Figure 4.12(b)** shows the BRI values given by the simulations. This graph also shows that, in the case with no wood, BRI increases remarkably over time. In the C1 and C3 simulation results, the temporal changes in ABI and BRI exhibit a different tendency when there is no wood in the domain. It may be expected that deposited wood pieces and jams would increase ABI and decrease BRI through local erosion. In simulation C2, a large thalweg appears after ~10 h (**Figure 4.12(b)** and **(c)**). This is generated by the merger of several thread channels through channel migration.

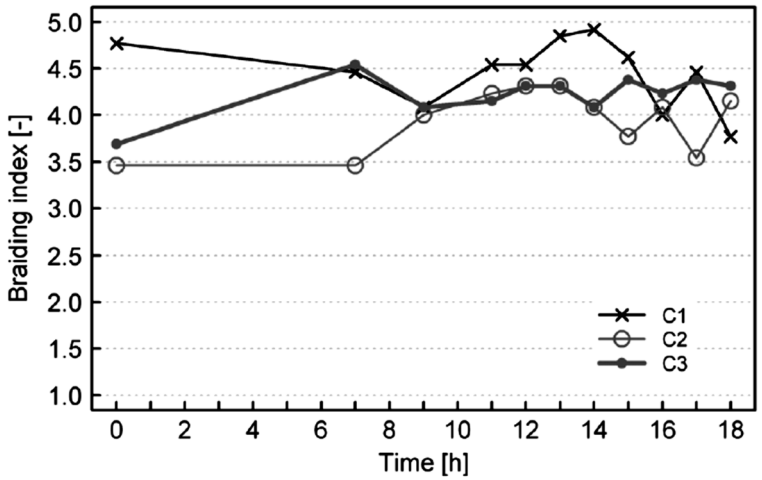

(a) BI in experiment (Bertoldi et al., 2014)

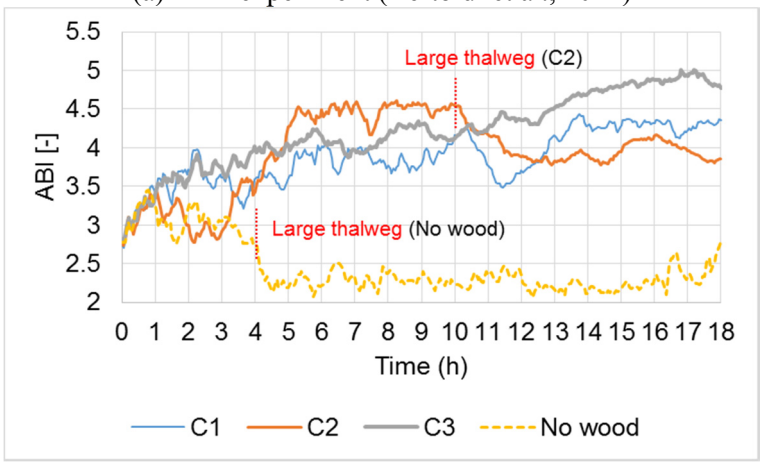

(b) ABI in simulation results

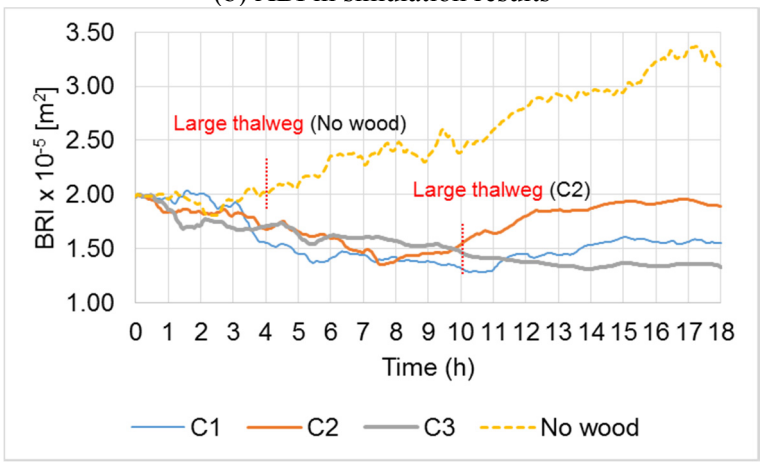

(c) BRI in simulation results

Figure 4.12 Temporal changes in bed morphology.

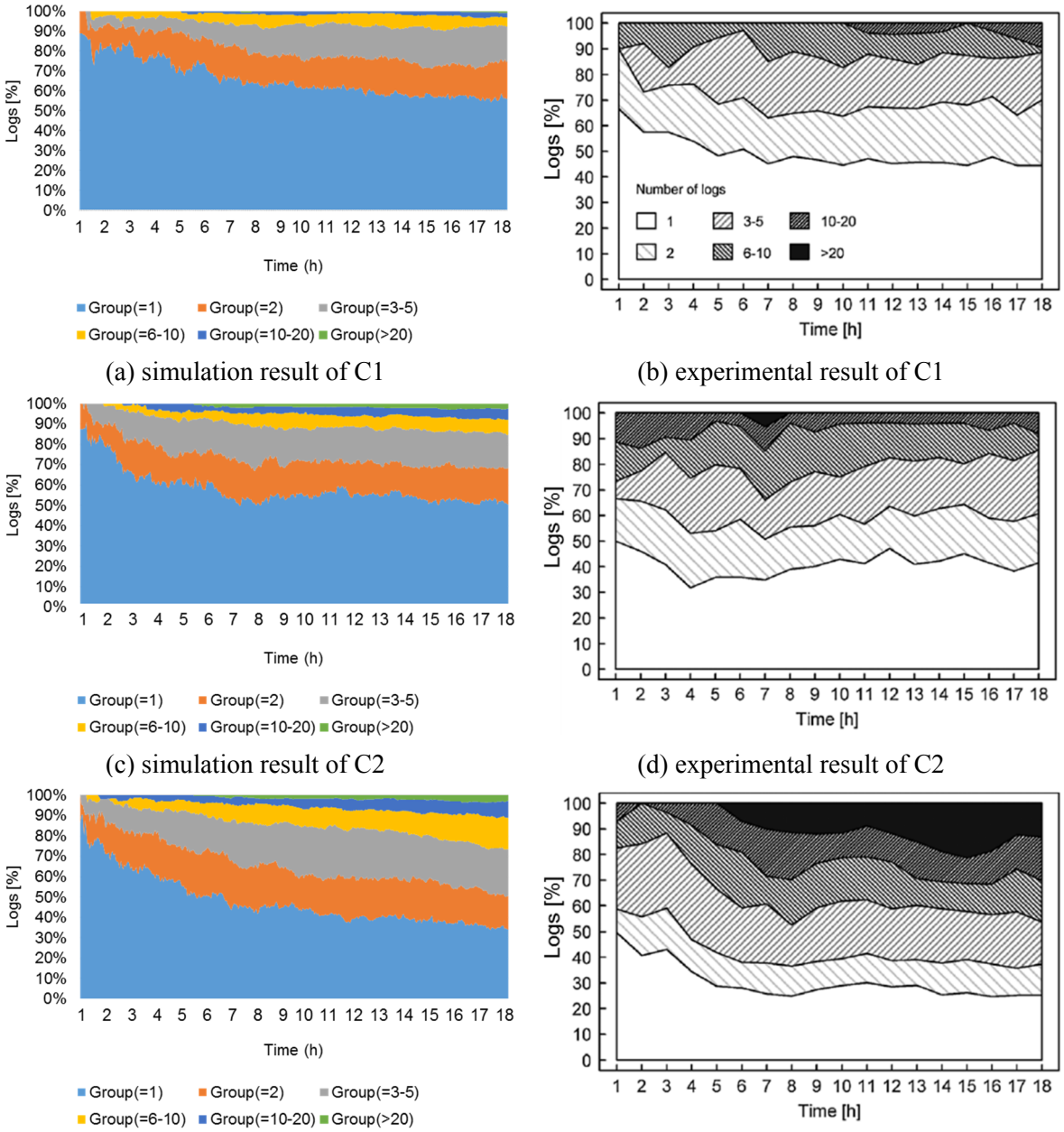

(a) simulation result of C1

(b) experimental result of C1

(c) simulation result of C2

(d) experimental result of C2

(e) simulation result of C3

(f) experimental result of C3

Figure 4.13 Proportion of stored wood jam (experiment is Bertoldi et al., 2014).

Therefore, the number of thread channels decreases and the thalweg depth increases. When this large thalweg is generated, the OI ratio of C2 increases dramatically (**Figure 4.10(c)**) and then steadily decreases after 10 h, because deposited wood pieces near the large thalweg flow away downstream. Moreover, the water flow becomes concentrated in the large thalweg at the river margin (near the wall), resulting in a reduction in the number of active braiding channels that can transport wood pieces. As a

result, the final number of stored wood pieces is smaller than in C1 and C3 (see Ave. position x_c and y_c of C2 in **Figure 4.11**).

Figure 4.13 shows the distribution of the number of wood pieces included in a jam. The simulated wood jam has a similar pattern as in the experiments (Bertoldi et al., 2014). As the wood supply increases over time (from C1 to C3), the number of wood jams (group >1) also increases. However, the overlapping phenomenon among wood pieces means that fewer of the simulated wood jams include an extremely large number of wood pieces (group >20) (**Figure 4.13 (a), (c), (e)**) than in the experimental cases (**Figure 4.13 (b), (d), (f)**). Instead, the simulation produced a higher maximum number of wood pieces in one big jam. Wood jams actively influence the bed morphology through localized erosion; thus, the thread channels generated by local erosion increase the ABI and decrease BRI. However, in simulation C2, the emergence of a large thalweg changes the wood deposition pattern (see **Figure 4.12**), although it is unclear whether the large thalweg affects the formation of wood jams.

4.4 DISCUSSION

The simulation results produced in the present study give a reasonable reproduction of the wood motion, including the wood deposition patterns, jam formation, root wad effect, and responses of bed morphology to large wood (see Mao et al., 2012; Marcus et al., 2002; Bertoldi et al., 2013; Welber et al., 2013; Bertoldi et al., 2014). Therefore, this model is useful for predicting the bed morphology under wood deposition in shallow rivers. However, to study the wood deposition patterns more precisely, further detailed modeling based on a physical approach may be necessary (Bertoldi et al., 2014).

In the simulation results, the presence of a root wad and the CDM have the most important roles in controlling deposition. In this study, the root wad particles were regarded as having a larger diameter than the trunk particles by a factor 3.3. Thus, the root wad particles were more easily subjected to larger drag forces because of the larger projection area than the trunk particles. However, root wad particles weigh more than trunk particles, which have the same density, and thus have a higher CDM than the trunk particles. Moreover, we considered the change of water depth caused by the root wad effect (see **Figure 4.5**). Therefore, a larger number of wood pieces with a root wad could be deposited in the simulation results, and the proportion of stored wood with a root wad was in good agreement with experimental results (**Figure 4.12**). Thus, we have shown that the root wad effect is reproduced reasonably well by our numerical method, and it may be expected that wood motions could be accurately simulated using more diverse root wads (size and density). However, the root wad effect should be carefully refined using more detailed measurements. In particular, the present simulation model employs

an empirical bed friction coefficient (Kang et al., 2018), and the bed friction coefficients of the root wad particle and trunk particle were tuned using a trial and error approach through a comparison with the experimental results.

Braudrick et al. (1997) stated that wood pieces are often deposited on the lateral margins (wall or bank) of the channel, parallel to the flow direction. In experiments (Bertoldi et al., 2014), the number of wood pieces deposited near the walls is smaller than suggested by the present computational results. This indicates that the present computation overestimates the number of wood pieces deposited near the side walls. One reason is that, if most of the particles that constitute a wood piece attach to the wall, the direction of wood motion heads toward the wall because of the small rolling friction. In this case, the wood is no longer being transported advectively. Thus, the modeling near the side wall should be refined.

In the model developed by Merten et al. (2010), burial is the most important mechanism for wood motion. Moreover, Latterell and Naiman (2007) suggested that partially buried large wood tends to be less movable than totally unburied large wood, and the burial state significantly affects a substantial amount of large wood in the river basin. However, we did not consider such phenomena, because it is difficult to quantify these effects under field conditions (Merten et al., 2010). Instead, we employed a modified Exner equation that reflects the dynamics of the deposited and removed wood pieces. The model can indirectly simulate the burial effect. Although we neglected this in our simulations, the wood deposition patterns simulated by the root wad effect and bed morphology are in good agreement with the experimental results (Welber et al., 2013; Bertoldi et al., 2014). Based on previous experiments (Bertoldi et al., 2014), this simulation employed a small constant discharge that is insufficient to cause large sediment movements. If we wish to consider unsteady flow (flood discharge) and finer sediments, this burial effect should be incorporated (see Merten et al., 2010).

In the simulation, the presence of a root wad clearly decreased the mobility of the wood by lifting the body above the bed and reducing the projected area exposed to the flow, as well as by reducing the buoyancy (Merten et al., 2010; Shields and Alonso, 2012). However, this simulation was unable to reproduce the development of local scour erosion around the root wad (Braudrick and Grant, 2000), because the grid cell size used in the computations was 0.02 m × 0.02 m, which is larger than the diameter of a root wad particle (0.01 m). Thus, a finer grid size is required to reproduce the local scour erosion around a root wad.

Davidson et al. (2015) emphasized that root wad significantly decreases the travel distance, whereas the length of the wood has less of an effect. Braudrick and Grant (2000), Merten et al. (2010), and Schenk et al. (2014) showed that the presence of root wad is the most important determinant of both

mobilization and travel distance. In addition, other researchers have shown that jam formation and complex wood shapes increase the stability of the wood motion (Abbe and Montgomery, 1996; Kollmann et al., 1999). Bertoldi et al (2014) found that a wood piece with a cross-shaped root is more likely to act as a key member in jam formation, but the presence of root wad was not a noticeable parameter in the wood jam distributions. However, the present simulation results did clarify the effect of root wad on some averaged values such as the stemwise angle and averaged position (see **Figures** 5.11(e) and 12). The simulations clearly showed that a wood piece with a root wad can deposit and settle more easily than one without a root wad.

In this study, we did not consider the difference in wood length, diameter, and root shape to reflect the experimental conditions (Bertoldi et al., 2014). To consider realistic root wad shapes, a number of small particles is required to reproduce the complicated root wad shape. Thus, we considered a simple spherical root wad particle that is larger than the stem particle diameter. However, real root wad has different characteristics in terms of density, size, and bed friction coefficient. In addition, the projection area, which is subjected to the drag force, is remarkably different from a sphere. To overcome this limitation, we can adjust the drag force coefficient (in this study, we used $C_D = 1$), but the detailed wood motion under the "hook effect" of root wad cannot be reproduced. Therefore, we should consider improved root wad shapes in future studies.

In their experiments, Welber et al. (2013) found a strong relationship between wood dispersal and bed morphology. However, another experiment by Bertoldi et al. (2014) did not find a clear relationship between the stored wood and bed morphology. In the present study, we showed the clear response of the bed morphology to wood deposition patterns using ABI and BRI; however, the present model is limited because the contact area between the wood and the bed is overestimated. This is because we assumed the contact area to be a circle with the same radius as the root wad particle. The contact area in the present model is generally larger than the real contact area, and this may lead to the bed change due to wood motions being overestimated. In future work, we should refine the present modeling of the contact area.

Our final point concerns the characteristics of the bed morphology that are affected by stored wood. In the simulation results, ABI increased when the number of pieces of stored wood increased. In addition, if the wood input supply rate increased, ABI increased while BRI decreased, as shown in the comparison between C1 and C3 (see **Figure 4.12**). This means that more pieces of wood can increase local erosion around the deposition area, and may generate several thread channels. Gurnell and Petts (2006) proposed a conceptual model to explain the interaction between vegetation (trees) and bed

morphology in the Tagliamento River, Italy (same location as the experiments by Bertoldi et al. (2014)). They illustrated that, if vegetation grows, this river becomes a braided channel and that vegetation colonization then increases under an adequate stream power. Coulthard (2005) demonstrated that a totally deposited wood piece can increase the braiding index in a sand bed through flow separation around the wood piece. Other studies have pointed out that both the motion and deposition of large wood affect the local stream flow; in particular, deposited large wood causes pool formation, fine sediment capture, and spatial territory generation for wildlife (Walter and Merritts, 2008; Merten et al., 2010). However, when the bed morphology causes dramatic changes, such as large thalwegs or meandering, the influence of wood jams becomes weak and the wood jams may themselves be driven by the bed morphology. The present model will help to clarify the relations between wood deposition and bed morphology.

4.5 SUMMARY

This chapter develops a numerical model for simulating the hydrodynamics involved in the transport of large pieces of wood in a braided river considering the root wad effect and anisotropic bed friction. The newly developed numerical model can precisely simulate the behavior of large pieces of wood using a 2-D depth-averaged Eulerian flow model that calculates the water flow and bed morphology in generalized coordinates. A Lagrange-type wood transport model is developed and combined with the flow model, and the applicability of the combined model is determined through a comparison with experimental results. From the simulation results, we quantitatively calculate the Active Braiding Index, Bed Relief Index, and mean values of wood deposition position, and deposition angle. We then analyze the relationship between the bed morphology responses and the wood deposition patterns in terms of the root wad effect and input supply. The proposed model reproduces the prominent features of the flume experiment, indicating that the present numerical approach can clarify and predict the behavior of large pieces of wood in accordance with the bed morphology.

CHAPTER 5

CONCLUSIONS AND FUTURE WORKS

Based on the computational results obtained and analyses done in the preceding chapters, some conclusions can be drawn as follows.

5.1 CONCLUSIONS

5.1.1 Part 1: Immobile Vegetation Effect (Bed Morphology with Growing Vegetation)

In the chapter 2, changes in a sharply curved river channel were simulated under two varying parameters: Peak flood discharge and non-uniform vegetation growth effect. To determine the effect of vegetation growth, the change in the channel patterns were quantified using the ABI and BRI. Using this approach, the present study successfully demonstrated that the effects of vegetation were influenced by the flood discharge. The results give basic and useful information, which is useful for river management and flood mitigation. However, some possibilities for future improvements were also highlighted; for instance, more detailed model validation and calibration for vegetation growth parameters. We plan to address such improvements in our future works.

The summary and limitations of this study are as follows.

1-1) Local erosion and global erosion

Erosion is classified as either local erosion or global erosion. Local erosion is caused by an increase in the flow velocity near an area of vegetation. This erosion may increase the number of threads in the channel as the flood event recedes. Global erosion is caused by strong secondary flow of the first kind working to erode the entire channel as the discharge reaches its peak. While local erosion increases the ABI due to the increase in thread channels, global erosion increases the BRI due to the increase in the thalweg depth. Sometimes, it was observed that global erosion swept away thread channels, resulting in a decrease in the ABI.

1-2) Moderate and Annual maximum flood event

Under a small peak discharge (690 m^3/s), vegetation works to accelerate local erosion because the flow velocity increases near the vegetation area, which increases the change in the ABI and BRI over time. If the peak discharge is high (1381 m^3/s), the strength of the secondary flow of the first kind

becomes significant, thereby activating global erosion. The vegetation effect also activates local erosion, such that the change in the BRI over time is larger than for the no-growing case for the same discharge.

1-3) Extreme flood event

However, if the peak flow discharge is extreme (2762 m^3/s), global erosion is dominant. The thalweg readily shifts toward the outer bank and the area of point bar with vegetation expansion. Under this scenario, the larger area of vegetation limits the scale of the secondary flow by reducing the flow velocity, which activates global erosion within the unvegetated areas such as the thalweg. As a result, the change in the BRI over time decreases compared to the no-growing vegetation case. This phenomenon should be further explored with more detailed field observation and experimental data.

5.1.2 Part 2: Mobile Vegetation Effect (Bed Morphology with Large Wood Dynamics)

5.1.2.1 Large wood dynamic on the fixed flat bed

This chapter developed a numerical model for simulating large wood dynamics with floating, sliding, and settling motions in shallow flows by coupling a depth-averaged 2D flow model and a Lagrange-type large wood dynamics model. In the present numerical model, we considered the change of draft for wood motion, anisotropic bed frictions, and the effects of root wad. The reproducibility of the proposed computational method is generally good, and the method produces a reasonable simulation of the different deposition patterns in relation to the changes in flow discharge and the root wad effect based on the experiment. The detailed conclusions are as follows:

2-1) Responses of the wood motion by flow discharge and channel slope

The wood piece tends to move toward the side walls after touching down on a lower water depth zone because of the small roll friction. Such motion becomes more dominant when the flow discharge decreases. The drag force and the water depth also increase when the flow discharge increases. Moreover, the wood piece easily flows away in the streamwise direction. However, the responses of the wood motion by change of the channel slope showed an unclear pattern because the employed values of channel slope were insufficient to affect the wood piece motion.

2-2) Root wad effect

In the experiments, the wood piece can become deposited more easily if it has a root section because the presence of the root wad decreases the draft for the wood motion in the wood piece, lifting the head of the wood piece by the root wad, although weight and volume in part of root wad are larger

than the stem of the wood piece. The simulation results also clearly reproduced the root effect well. However, in cases of wood without the root wad, the experiment results only showed deposited wood pieces near the wall. Through these results, we also discovered a relationship between the deposition angle of the large wood and flow discharge. The stemwise angle of the deposited wood piece becomes smaller when the flow discharge is larger. Consequently, it means that the deposited wood angle is associated with the projection area between the flow discharge and the wood piece. Thus, further study should consider additional parameters, such as the projection area of the wood piece considering the angle between stemwise and streamwise directions.

2-3) Limitations of the developed model

Both in the experimental and computational results, the wood piece with root wad tends to move toward the side walls because of the smaller rolling friction coefficient. We considered the shape of the wood piece stem to be a cylinder in the experiment. Even in the simulation, we considered the wood piece as sphere particles. Therefore, the roll friction coefficient is relatively smaller than that of natural large wood, which has branches, rough surfaces, and irregularly shaped cross-sections.

5.1.2.2 Bed morphology with large wood dynamics

In the chapter 4 has developed a computational model for simulating large wood deposition and changes in bed morphology. The model was used to reproduce the phenomena observed in experiments by Welber et al. (2013) and Bertoldi et al. (2014), allowing the applicability of the present model to be discussed. The simulation results showed some new findings in terms of the relation between wood motion and flow features. The present numerical model was demonstrated to be a useful tool for predicting and clarifying the fundamental aspects of wood motion, such as the location of wood deposition, scale of wood jams, deposited stemwise angle, and root wad effect. Although this model has some limitations, the reproduction of the experimental results was reasonably good. If we could obtain more detailed data from diverse cases of practical large wood deposition, it would be possible to improve the model by further tuning certain coefficients based on a comparison between the computational and experimental results. The main findings of this study are as follows.

3-1) Reproducibility

We neglected wood particle collision to reduce the computation time. However, the simulation results showed reasonable agreement with the experimental results (Bertoldi et al., 2014) in terms of

deposition patterns and bed morphology. If we considered wood collision, we could expect to achieve better agreement.

3-2) Root wad effect

The root wad effect is a remarkable factor in this study. We employed a root wad particle diameter some 3.3 times larger than that of the stem particle, and we considered changes in the settled height of each particle under the root wad effect. The simulation results showed that the presence of root wad decreases the wood mobility and enhances wood deposition. The same phenomenon was observed by Bertoldi et al. (2014). However, we considered simple spherical particles for the root wad, and these are insufficient for reflecting the complex behavior related to root wad, such as the hook effect and trapping of other wood pieces. This limitation can be overcome by expressing the root wad as a number of smaller particles.

3-3) Bed morphology with jam formation

In the simulation results, wood deposition and jam formation led to an increase in ABI and a decrease in BRI in comparison with the no wood case. This suggests that wood deposition can affect the bed morphology. However, when a large thalweg is generated (see C2), the influence of wood jams on bed morphology weakens. The number of stored wood pieces increases slightly when a large thalweg is created.

Through this study, we have identified some novel aspects to the relations between wood deposition and bed morphology. Thus, we believe that this approach is worth advancing to obtain more detailed information on the wood deposition and associated bed morphology phenomena. Such knowledge can be applied to disaster prevention research and the improvement of river environments.

5.2 FURTER CHALLENGES: COMBINATION OF MOBILE/IMMOBILE TYPES VEGETATION FOR HYDRODYNAMICS COMPUTATION

Growing vegetation (immobile vegetation) changes river environment by colonization. This study showed that vegetation colonies affect the water flow and the sediment. Vegetation effect increases the drag force, which decreases flow velocity and increases water depth. Thus, if growing vegetation makes a large vegetated colony, bed morphology patterns will be changed.

Large wood (mobile vegetation) also affects the water flow and sediment through its motion by dynamic force, which is interaction between the water flow and large wood. Large wood locally affects

the bed morphology through accumulating stored wood at a point that is highly spatially and temporally variable, whereas the growing vegetation effect steadily activates through expansion of its area.

In this study, we assume that growing vegetation and large wood consist of rigid bodies, which are able to neglect elastic bending moment. However, all vegetation has elastic stems. This should affect the motion of wood in being captured by obstacles, such as bridge piers and trees. Therefore, if we consider vegetation and large wood in the same computational domain, bending moment should be considered.

In this study, we did not consider the gravity effect on either vegetation or large wood, because a flat bed, which has mild slope, was employed. Thus, we could not consider the bank collapse by gravity effect due to using two types of vegetation. In addition, we did not consider the large wood going down to lower parts of the bed by rolling motion.

Figure 5.1(a) shows tentative simulation results considering vegetation growth and large wood. This case is to attempt the combination of mobile and immobile types of vegetation for hydrodynamic computation. In this simulation we should consider equivalent quantities between vegetation and large wood. For instance, we can use **Equation** (2-13), which is related to vegetation density at drag force term, to consider the large wood as a vegetation (immobile state). Here, the stem diameter of large wood is regarded as the stem of vegetation. In this case, we should consider the density of large wood. Then, when this immobile vegetation (fixed large wood on the bed) is pulled by certain conditions (bed erosion and large flow velocity), it can be converted into large wood (mobile state).

The seeding process can also be applied in this model. In the computational domain, if a seed is feuded from upstream, this seed flows downstream. Then, the seed may deposit on a lower water depth area, which is appropriate for germination. When seed deposits occur over enough time for germination, the growing vegetation model is able to be applied at this grid area (**Figure 5.1(b)**).

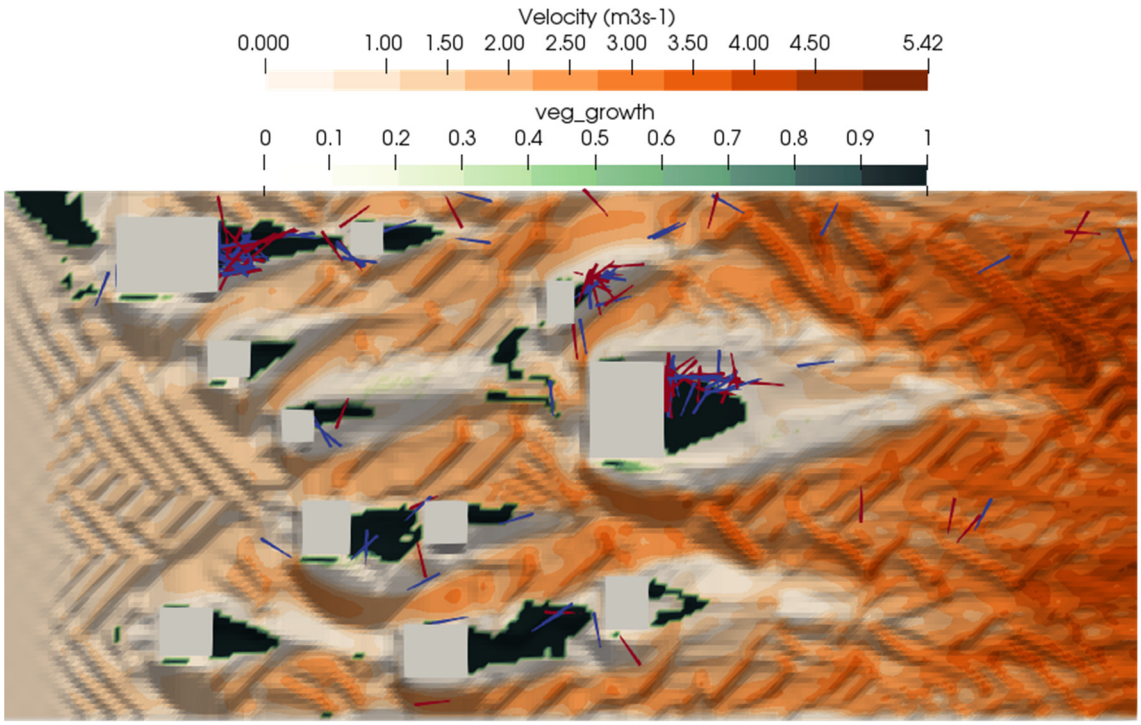

(a) tentative simulation result considering growing vegetation, large wood and bed morphology

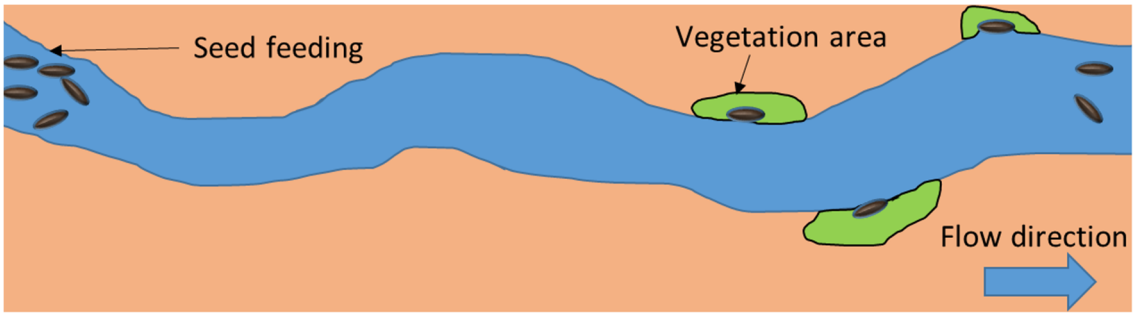

(b) seeding process

Figure 5.1 Further challenges.

REFERENCES

[1] Abbe, T.B., and Montgomery, D.R., 1996. Large woody debris jams, channel hydraulics and habitat formation in large rivers. *Regul. Rivers Res. Manage.* 12(2–3): 201–221.

[2] Abbe, T.B., and Montgomery, D.R., 2003. Patterns and processes of wood debris accumulation in the Queets river basin, Washington. *Geomorphology*. 51(1–3): 81–107.

[3] Abernethy, B., and Rutherfurd, I.D., 2001. The distribution and strength of riparian tree roots in relation to riverbank reinforcement. *Hydrol. Process*. 15: 63–79.

[4] Ambrose, J., and Tripeny, P., 2011. Building structures, John Wiley & Sons. 119-121.

[5] Andreoli, A., Comiti, F., and Lenzi, M.A., 2007. Characteristics, distribution and geomorphic role of large woody debris in a mountain stream of the Chilean Andes. *Earth Surf. Processes Landforms*. 32(11): 1675–1692.

[6] Ashida, K., and Michiue, M., 1972. Study on hydraulic friction and bedload transport rate in alluvial streams. *Trans. JSCE*. 206: 59–69.

[7] Ashmore, P., 1991. How do gravel-bed rivers braid? *Can. J. Earth Sci*. 28: 326–41, doi:10.1139/e91-030.

[8] Bennett, S.J., Pirim, T., and Barkdoll, B.D., 2002. Using simulated emergent vegetation to alter flow direction within a straight experimental channel, *Geomorphology*. 44: 115–126.

[9] Berg, N., Carlson, A., and Azuma, D., 1998. Function and dynamics of woody debris in stream reaches in the central Sierra Nevada, California, *Can. J. Fish. Aquat. Sci*. 55: 1807–1820.

[10] Bertoldi, W., 2012. Life of a bifurcation in a gravel-bed braided river. *Earth Surf. Processes Landforms*. 37(12): 1327–1336.

[11] Bertoldi, W., Drake, N.A., and Gurnell, A.M., 2011. Interactions between river flows and colonizing vegetation on a braided river: Exploring spatial and temporal dynamics in riparian vegetation cover using satellite data. *Earth Surf. Processes Landforms*. 36: 1474–1786, doi:10.1002/esp.2166.

[12] Bertoldi, W., Gurnell, A.M., and Welber, M., 2013.Wood recruitment and retention: the fate of eroded trees on a braided river explored using a combination of field and remotely-sensed data sources. *Geomorphology*. 180–181: 146–155.

[13] Bertoldi, W., Welber, M., Mao, L., Zanella, S., and Comiti, F., 2014. A flume experiment on wood storage and remobilization in braided river systems. *Earth Surf. Processes Landforms*. 39: 804-813.

[14] Bertoldi, W., Zanoni, L., and Tubino, M., 2009. Planform dynamics of braided streams Planform dynamics. *Earth Surf. Processes Landforms*. 34: 547–557.

[15] Bocchiola, D., Catalano, F., Menduni, G., and Passoni, G., 2002. An analytical–numerical approach to the hydraulics of floating debris in river channels. *J. Hydrol*. 269: 65–78.

[16] Bocchiola, D., Rulli, M.C., and Rosso, R., 2006. Flume experiments on wood entrainment in rivers. *Adv. Water Resour*. 29: 1182–1195.

[17] Braudrick, C.A, Grant, GE, Northwest, P., 2001. Transport and deposition of large woody debris in streams: a flume experiment. *Geomorphology*. 263–283.

[18] Braudrick, C.A., and Grant, G.E., 2000. When do logs move in rivers?. *Water Resour. Res*. 36: 571–583.

[19] Braudrick, C.A., Dietrich, W.E., Leverich, G.T., and Sklar, L.S., 2009. Experimental evidence for the conditions necessary to sustain meandering in coarse bedded rivers. *Proc. Natl. Acad. Sci. USA 2009*. 106: 16936–16941, doi:10.1073/pnas.0909417106.

[20] Braudrick, C.A., Grant, G.E., Ishikawa, Y., Ikeda, H., 1997. Dynamics of wood transport in streams: A flume experiment. *Earth Surf. Processes Landforms*. 22(7): 669–683.

[21] Brooks, A.P., Abbe, T., Cohen, T., Marsh, N., Mika, S., Boulton, A., Broderick, T., Borg, D., and Rutherfurd, I., 2006. Design Guidelines for the Reintroduction of Wood into Australian Streams. Land & Water, Canberra, Australia.

[22] Burge, L.M., 2006. Stability, morphology and surface grain size patterns of channel bifurcation in gravel-cobble bedded anabranching. *Earth Surf. Processes Landforms*. 31: 1211–1226.

[23] Cadol, D., and Wohl, E., 2010. Wood retention and transport in tropical, headwater streams, La Selva Biological Station, Costa Rica. *Geomorphology*. 123: 61–73. http://dx.doi.org/10.1016/j.geomorph.2010.06.015.

[24] Camporeale, C., Perucca, E., Ridolfi, L., and Gurnell, A.M., 2013. Modeling the interactions between river morphodynamics and riparian vegetation. *Rev. Geophys*. 51: 379–414, doi:10.1002/rog.20014.

[25] Collins, B.D., Montgomery, D.R., Fetherston, K.L., and Abbe, T.B., 2012. The floodplain large-wood cycle hypothesis: a mechanism for the physical and biotic structuring of temperate forested alluvial valleys in the North Pacific coastal ecoregion. *Geomorphology*. 139–140: 460–470.

[26] Comiti, F., Andreoli, A., Lenzi, M.A., and Mao, L., 2006. Spatial density and characteristics of woody debris in five mountain rivers of the Dolomites (Italian Alps). *Geomorphology*. 78(1–2): 44–63.

[27] Coulthard, T.J. 2005. Effects of vegetation on braided stream pattern and dynamics. *Water Resources Research*. 41, W04003.

[28] Courant, R., Friedrichs, K., and Lewy, H., 1928. Über die partiellen Differenzengleichungen der mathematischen Physik, *Mathematische Annalen (in German)*. 100(1): 32–74.

[29] Crosato, A., and Saleh, M.S., 2011. Numerical study on the effects of floodplain vegetation on river planform style. *Earth Surf. Processes Landforms*. 36: 711–720.

[30] Curran, J.C., 2010. Mobility of large woody debris (LWD) jams in a low gradient channel. *Geomorphology*. 116(3–4): 320–329.

[31] Davidson, S., MacKenzie, L., and Eaton, B., 2015. Large wood transport and jam formation in a series of flume experiments. *Water Resour. Res.* http://dx.doi.org/10.1002/ 2015WR017446.

[32] Dixon, S.J., and Sear, D.A., 2014. The influence of geomorphology on large wood dynamics in a low gradient headwater stream. *Water Resour. Res*. 50: 9194–9210. doi:10.1002/2012WR013085.

[33] Eaton, B.C., Millar, R.G., and Davidson, S., 2010. Channel patterns: braided, anabranching, and single-thread. *Geomorphology*, 120: 353–364.

[34] Eekhout, J.P.C., Fraaije, R.G.A., and Hoitink, A.J.F, 2014. Morphodynamic regime change in a reconstructed lowland stream. *Earth Surf. Dyn*. 2: 279–293.

[35] Egger, G., 2007. Floodplain vegetation models and application in river restoration, KICT, *The 2nd international Workshop on River Environment*. 41-66.

[36] Egozi, R., and Ashmore, P., 2008. Defining and measuring braiding intensity. *Earth Surf. Processes Landforms*. 33: 2121–2138.

[37] Engelund, F., 1974. Flow and bed topography in channel bends. *J. Hydraul. Div*. 100: 1631–1648.

[38] Everitt, B., 1968. Use of the cottonwood in an investigation of the recent history of a floodplain. *Am. J. Sci*. 266: 417–439.

[39] Garcia, X.F., Schnauder, I., and Pusch, M.T., 2012. Complex hydromorphology of meanders can support benthic invertebrate diversity in rivers. *Hydrobiologia*. 685: 49–68, doi:10.1007/s10750-011-0905-z.

[40] Google Earth. Available online: https://earth.google.com/web/ (accessed on 21 June 2018).

[41] Gran, K., and Paola, C., 2001. Riparian vegetation controls on braided stream dynamics. *Water Resour. Res*. 37: 3275–3283, doi:10.1029/ 2000WR000203.

[42] Gurnell, A.M., 2003. Wood storage and mobility. In: Gregory, S., Boyer, K., AM, G. (Eds.), The ecology and management of wood in world rivers. *American Fisheries Society Symposium*. 75–91.

[43] Gurnell, A.M., 2013. Wood in fluvial systems, in Treatise on Geomorphology. *Academic, San Diego, Calif*. edited by J. Shroder and E. Wohl, 163–188.

[44] Gurnell, A.M., and Grabowski, R.C., 2015. Vegetation–Hydrogeomorphology Interactions in a Low-Energy, Human-Impacted River. *River Res. Appl*. 32: 202–215.

[45] Gurnell, A.M., and Petts, G.E., 2002. Island-dominated landscapes of large floodplain rivers. *Freshwater Biol*. 47(4): 581–600.

[46] Gurnell, A.M., and Petts, G.E., 2006. Trees as riparian engineers: the Tagliamento River, Italy. *Earth Surf. Processes Landforms*. 31: 1558–1574.

[47] Gurnell, A.M., and Sweet, R., 1998. The distribution of large woody debris accumulations and pools in relation to woodland stream management in a small, low-gradient stream. *Earth Surf. Processes Landforms*. 23(12): 1101–1121.

[48] Gurnell, A.M., Gregory, K.J., and Petts, G.E., 1995. The role of coarse woody debris in forest aquatic habitats: Implications for management. *Aquat. Conserv. Mar. Freshwater Ecosyst*. 5(2): 143–166.

[49] Gurnell, A.M., Morrissey, I.P., Boitsidis, A.J.; Bark, T., Clifford, N.J., Petts, G.E., and Thompson, K., 2006. Initial adjustments within a new river channel: Interactions between fluvial processes, colonizing vegetation, and bank profile development. *Environ. Manag*. 38: 580–596.

[50] Gurnell, A.M., Petts, G.E., Hannah, D.M., Smith, B.P.G., Edwards, P.J., Kollmann, J., Ward, J.V., and Tockner, K., 2000b. Wood storage within the active zone of a large European gravel-bed river. *Geomorphology*. 34(1– 2): 55–72.

[51] Gurnell, A.M., Petts, G.E., Hannah, D.M., Smith, B.P.G., Edwards, P.J., Kollmann, J., Ward, J.V., and Tockner, K., 2001. Riparian vegetation and island formation along the gravel-bed Fiume Tagliamento, Italy. *Earth Surf. Processes Landforms*. 26(1): 31–62.

[52] Gurnell, A.M., Petts, G.E., Harris, N., Ward, J.V., Tockner, K., Edwards, P.J., and Kollmann, J., 2000a. Large wood retention in river channels: The case of the Fiume Tagliamento, Italy. *Earth Surf. Processes Landforms*. 25(3): 255–275.

[53] Gurnell, A.M., Piégay, H.F., Swanson, J. and Gregory, S.V., 2002. Large wood and fluvial processes. *Freshwater Biol*. 47(4): 601–619.

[54] Gurnell, A.M., Tockner, K.P., Edwards, J., and Petts, G.E., 2005. Effects of deposited wood on biocomplexity of river corridors. *Frontiers Ecol. Environ*. 3(7): 377–382.

[55] Haga, H., Kumagai, T., Otsuki, K., and Ogawa, S., 2002. Transport and retention of coarse woody debris in mountain streams: An in situ field experiment of log transport and a field survey of coarse woody debris distribution. *Water Resour. Res.* 38: 1126.

[56] Hasegawa, K., 1985. Hydraulic Study on Alluvial Meandering Channel Planes and Bedform Topography-Affected Flows; Doctoral Paper, Hokkaido University: Sapporo, Japan.

[57] Haslam, S.M., 1972. The reed, Phragmites communiss Trin. In the Reed. *Norfolk Reed Growers' Association*. Second edition, 3-48.

[58] Hicken, E.J., 1984. Vegetation and river channel cynamics, *Can. Geographer*. XXVIII(2): 111–126.

[59] Hoey, T., and Sutherland, A., 1991. Channel morphology and bedload pulses in braided rivers: A laboratory study. *Earth Surf. Processes Landforms*. 16: 447–462.

[60] Hosoda, T., Nagata, N., Kimura, I., Michibata, K., and Iwata, M., 2001. A depth averaged model of open channel flows and secondary currents in a generalized curvilinear coordinate system. *In Advances in Fluid Modeling & Turbulence Measurements*, Ninokata, H., Wada, A., Tanaka, N., Eds.; World Scientific: Singapore. 63–70.

[61] Huang, H.Q., and Nanson, G.C., 1997. Vegetation and channel variation; a case study of four small streams in southeastern Australia, *Geomorphology*. 18: 237–249.

[62] Ikeda, S., and Izumi, N., 1990. Width and depth of self-formed straight gravel rivers with bank vegetation. *Water Resour. Res*. 26(10): 2353-2364.

[63] International River Interface Cooperative (iRIC). 2018. Available Online: http://i-ric.org/en.

[64] Iroumé, A., Andreoli, A., Comiti, F., Ulloa, H., and Huber, A., 2010. Large wood abundance, distribution and mobilization in a third order coastal mountain range river system, southern Chile. For. *Ecol. Manag*. 260: 480–490. http://dx.doi.org/10.1016/j.foreco. 2010.05.004.

[65] Iwagaki, Y., 1956. Hydrodynamical study on critical tractive force. *Trans. Jpn. Soc. Civil. Eng*. 41: 1–21.

[66] Iwasaki, T., Shimizu, Y., and Kimura, I., 2012. Numerical simulation on bed evolution and channel migration in rivers. *Proc. of the River Flow 2012-Murillo (eds.)*, 673-679.

[67] Iwasaki, T., Shimizu, Y., and Kimura, I., 2016a, Numerical simulation of bar and bank erosion in a vegetated floodplain: A case study in the Otofuke River. *Adv. Water Resour*. 93: 118–134.

[68] Iwasaki, T., Shimizu, Y., and Kimura, I., 2016b. Sensitivity of free bar morphology in rivers to secondary flow modeling: Linear stability analysis and numerical simulation. *Adv. Water Resour*. 92: 57–72.

[69] Jang, C., and Shimizu, Y., 2005. Numerical simulations of the behavior of alternate bars with different bank strengths. *J. Hydraul. Res*. 43: 595–611.

[70] Jang, C., and Shimizu, Y., 2007. Vegetation effects on the morphological behavior of alluvial channels. *J. Hydraul. Res*. 45: 763–772.

[71] Kalkwijk, J.P., and De Vriend, H.J., 1980. Computational of the flow in shallow river bends. *J. Hydraul. Res*. 18: 327–342.

[72] Kang T., Kimura, I., Shimizu, Y., 2018. Study on advection and deposition of driftwood affected by root in shallow flows. *Journal of Japan Society of Civil Engineers, Ser., B1 (Hydraulic Engineering)*. 74(4): I_757-I_762.

[73] Kang, T., Kimura, I., and Shimizu, Y., 2018. Responses of bed morphology to vegetation growth and flood discharge at a sharp river bend. *Water*. 10(223): 1-25.

[74] Kaufmann, P.R., Levine, P., Robinson, E.G., Seeliger, C., and Peck, D.V., 1999. Surface waters: Quantifying physical habitat in wadeable streams, EPA/620/R-99/003, U.S. EPA Office of Research and Development, Environmental Monitoring and Assessment Program (EMAP), Washington, DC.

[75] Keller, E.A., and Swanson, F.J., 1979. Effects of large organic material on channel form and fluvial processes. *Earth Surf. Processes Landforms*. 4(4): 361– 380.

[76] Kim, H., Kimura, I., and Shimizu, Y., 2012. Characteristics of local erosion and deposition with a patch of vegetation. *Proc. River Flow 2012*, 1: 287–293.

[77] Kimura, I., 2012. NaysCUBE solver manual. Available Online: http://i-ric.org/en.

[78] Kimura, I., and Kitazono, K., 2017. Studies on driftwood motions in curved channel with obstacles using hydraulic experiments and CFD models. *Proceeding of 4th International Symposium of Shallow Flows, Eindhoven*, Netherlands, June.

[79] Kimura, I., Hosoda, T., and Onda, S., 2007. Fundamental properties of suspended sediment transport in open channel flows with a side cavity. *In Proceedings of the RCEM 2007, Enschede, The Netherlands, 17–21 September 2007; Balkema Pblishers: Enschede, The Netherlands, 2007*: 1203–1210.

[80] Kitazono, K., Kimura, I., and Shimizu, Y., and Kyuka, T., 2016. Computations on driftwood motions around obstacles coupling with a three-dimensional flow model. *Proceeding of IAHR-APD 2016*.

[81] Kollmann, J., Vieli, M., Edwards, P.J., Tockner, K., and Ward, J.V., 1999. Interactions between vegetation development and island formation in the Alpine river Tagliamento. *Appl. Veg. Sci*. 2: 25–36.

[82] Korea Institute of Construction Technology (KICT)., 2015. Analysis of Change in River Morphology and Vegetation due to Artificial Structure. Internal Research Project Report, Available online: http://www.nl.go.kr/nl/ (accessed on 21 February 2018). (In Korean)

[83] Kramer, N., and Wohl, E., 2017. Rules of the road: A qualitative and quantitative synthesis of large wood transport through drainage networks. *Geomorphology*, 279: 74-97.

[84] Lassettre, N.S., Piégay, H., Dufour, S., and Rollet, A.J., 2008. Decadal changes in distribution and frequency of wood in a free meandering river, the Ain River, France. *Earth Surf. Processes Landforms*. 33(7): 1098-1112.

[85] Latterell, J.J., and Naiman, R.J., 2007. Sources and dynamics of large logs in a temperate floodplain river. *Ecological Applications*. 17: 1127–1141.

[86] MacVicar, B.J., and Piégay, H., 2012. Implementation and validation of video monitoring for wood budgeting in a wandering piedmont river, the Ain River (France). *Earth Surf. Processes Landforms*. 37(12): 1272– 1289.

[87] MacVicar, B.J., and Piégay, H., Henderson, A., Comiti, F., Oberlin, C., and Pecorari, E., 2009. Quantifying the temporal dynamics of wood in large rivers: Field trials of wood surveying,

dating, tracking, and monitoring techniques. *Earth Surf. Processes Landforms*. 34(15): 2031–2046.

[88] Manners, R.B., Doyle, M.W., 2008. A mechanistic model of woody debris jam evolution and its application to wood-based restoration and management. *River Res. Appl*. 24: 1104–1123.

[89] Manners, R.B., Doyle, M.W., and Small, M.J., 2007. Structure and hydraulics of natural woody debris jams. *Water Resour. Res*. 43: 1–17.

[90] Mao, L., Andreoli, A., Iroumé, A., Comiti, F., and Lenzi, M., 2013. Dynamics and management alternatives of in-channel large wood in mountain basins of the southern Andes. *Bosque (Valdivia)*. 34: 319–330.

[91] Mao, L., Ravazzolo, D., Picco, L., Rigon, E., and Lenzi, M., 2012. Types and volumes of in-channel wood in three Italian gravel-bed rivers suffering from different degrees of human disturbances. *Proceedings, first international conference on Integrative Sciences and Sustainable Development of Rivers, 26–28 June 2012, Lyon, France*.

[92] Marcus, W.A., Marston, R.A., Colvard, C.R.J., Gray, and R.D., 2002. Mapping the spatial and temporal distributions of woody debris in streams of the Greater Yellowstone Ecosystem, USA. *Geomorphology*. 44: 323–335. http://dx.doi.org/10.1016/S0169-555X(01)00181-7.

[93] McKenney, R., Jacobson, R.B., and Wertheimer, R.C., 1995. Woody vegetation and channel morphogenesis in low-gradient, gravel-bed streams in the Ozark Plateaus, Missouri and Arkansas. *Geomorphology*. 13: 175–198.

[94] Merten, E., Finlay, J., Johnson, L., Newman, R., Stefan, H., and Vondracek, B., 2010. Factors influencing wood mobilization in streams. *Water Resour. Res*. 46. W10514, doi:10.1029/2009WR008772.

[95] Millar, R.G., 2000. Influence of bank vegetation, on alluvial channel patterns. *Water Resour. Res*. 36: 1109–1118.

[96] Millar, R.G., and Qucik, M.C., 1993. Effect of bank stability on geometry of gravel rivers. *J. Hydraul. Eng*. 119: 1343–1363.

[97] Montgomery, D.R., and Piégay, H., 2003. Wood in rivers: Interactions with channel morphology and processes. *Geomorphology*. 51(1–3): 1–5.

[98] Moulin, B., Piégay, H., 2004. Characteristics and temporal variability of large woody debris trapped in a reservoir on the River Rhone: Implications for river basin management. *River Research and Applications*. 20(1): 79–97.

[99] Moulin, B., Schenk, E.R., and Hupp, C.R., 2011. Distribution and characterization of in-channel large wood in relation to geomorphic patterns on a low-gradient river. *Earth Surf. Processes Landforms*. 36(9): 1137–1151.

[100] Murray, A.B. and Paola, C., 2003. Modelling the effect of vegetation on channel pattern in bedload rivers, *Earth Surf. Processes Landforms*. 28: 131–143.

[101] Nakamura, F., and Swanson, F.J., 1993. Effects of coarse woody debris on morphology and sediment storage of a mountain stream system in western Oregon. *Earth Surf. Processes Landforms*. 18(1): 43–61.

[102] Nanson, G.C., and Beach, H.F., 1977. Forest succession and sedimentation on a meandering-river floodplain. Northeast British Columbia, *Canada. J. Biogeogr*. 4: 229–251.

[103] Nanson, G.C., and Knighton, A.D., 1996. Anabranching rivers: Their cause, character, and classification, *Earth Surf. Processes Landforms*. 21: 217 – 239.

[104] National Typhoon Center, Typhoon White Book (in Korean), 2010. Available online: http://typ.kma.go.kr (accessed on 21 June 2018).

[105] National Wetlands Center. Available online: http://wetlandkorea.blog.me (accessed on 21 June 2018).

[106] Onda, S., Hosoda, T., and Kimura, I., 2006. Refinement of a depth-averaged model in curved channel in generalized curvilinear coordinate system and its verification. *Ann. J. Hydrau. Eng*. 50: 769–774.

[107] Perona, P., Molnar, P., Crouzy, B., Perucca, E., Jiang, Z., McLelland, S., Wüthrich, D., Edmaier, K., Francis, R., and Camporeale, C., 2012. Biomass selection by floods and related timescales: Part 1. Experimental observations. *Adv. Water Resour*. 39: 85–96, doi:10.1016/j.advwatres.2011.09.016.

[108] Persson, B.N.J., 1999. Sliding friction, *Surface Science Reports*. 33(3): 83-119.

[109] Perucca, E., Camporeale, C., and Ridolfi, L., 2007. Significance of the riparian vegetation dynamics on meandering river morphodynamics. *Water Resour. Res. 43*: W03430, doi:10.1029/2006WR005234.

[110] Piegay, H., and Gurnell, A.M., 1997. Large woody debris and river geomorphological pattern: Examples from SE France and S England. *Geomorphology*. 19(1–2): 99–116.

[111] Piegay, H., Thevenet, A., and Citterio, A., 1999. Input, storage and distribution of large woody debris along a mountain river continuum, the Drome River, France. *Catena*, 35(1): 19–39.

[112] Richmond, D., and Fausch, K.D., 1995. Characteristics and function of large woody debris in subalpine Rocky Mountain streams in northern Colorado, *Can. J. Fish. Aquat. Sci*. 52: 1789–1802.

[113] Robert, M.V.T., 2004. Flow dynamics at open channel confluent-meander bends. Ph.D. Thesis, University of Leeds, UK.

[114] Robertson, K.M., and Augspurger, C.K., 1999. Geomorphic processes and spatial patterns of primary forest succession on the Bogue Chitto River, USA. *J. Ecol*. 87: 1052–1063.

[115] Rood, S.B., and Mahoney, J.M., 1990. Collapse of riparian poplar forests downstream from dams in western prairies: Probable causes and prospects for mitigation. *Environ. Manag*. 14: 451–464.

[116] Ruiz-Villanueva, V., Bladé, E., and Sánchez-Juny, M., 2014b. Two-dimensional numerical modeling of wood transport. *J. Hydroinformatics*. 16(5): 1077-1096.

[117] Ruiz-Villanueva, V., Bodoque, J., Dez-Herrero, A., and Bladé, E., 2014a. Large wood transport as significant influence on flood risk in a mountain village. *Nat. Hazards*. 74: 967–987.

[118] Ruiz-Villanueva, V., Wyżga, B., Zawiejska, J., Hajdukiewicz, M., and Stoffel, M., 2016. Factors controlling large-wood transport in a mountain river. *Geomorphology*. 272: 21–31.

[119] Sawyer, A.H., and Cardenas, M.B., 2012. Effect of experimental wood addition on hyporheic exchange and thermal dynamics in a losing meadow stream. *Water Resour. Res*. 48.

[120] Schenk, E.R., Moulin, B., Hupp, C.R., and Richter, J.M., 2014. Large wood budget and transport dynamics on a large river using radio telemetry. Earth Surf. Processes Landforms, 39: 487–498. doi:10.1002/esp.3463.

[121] Schnauder, I., and Sukhodolov, A.N., 2012. Flow in a tightly curving meander bend: Effects of seasonal changes in aquatic macrophyte cover. *Earth Surf. Processes Landforms*. 37: 1142–1157, doi:10.1002/esp.3234.

[122] Seo, J.I., and Nakamura, F., 2009. Scale-dependent controls upon the fluvial export of large wood from river catchments. *Rivers*. 80: 786–800.

[123] Shields, F.D., and Alonso, C.V., 2012. Assessment of flow forces on large wood in rivers. *Water Resour. Res*. 48. W04516, doi:10.1029/2011WR011547.

[124] Shimizu, Y., Kobatake, S., and Arafune, T., 2000. Numerical study on the flood-flow stage in gravel-bed river with the excessive riverine trees, *Annual J. Hydr. Eng*. 44: 819-824.

[125] Shimizu, Y., Takebayashi, H., Inoue, T., Hamaki, M., Iwasaki, T., and Nabi, M., 2014. Nays2DH solver manual. Available Online: http://i-ric.org/en.

[126] Smith, D.G., 1976. Effect of vegetation on lateral migration of anastomosed channels of a glacier Meltwater river. *Geol. Soc. Am. Bull*. 87: 857–860.

[127] Song, X., and Bai, Y., 2015. A new empirical river pattern discriminant method based on flow resistance characteristics. *Catena*. 135: 163–172.

[128] Swanson, F.J., 2003. Wood in rivers: a landscape perspective, in ecology and management of wood in world rivers. edited by Gregory, S.V., Boyer, K.L., and Gurnell, A.M., *Fish. Soc*. 299–313, Bethesda, Md.

[129] Tal, M., and Paola, C., 2010. Effects of vegetation on channel morphodynamics: results and insights from laboratory experiments, *Earth Surf. Processes Landforms*. 35(9): 1014-1028.

[130] Thévenet, A., Citterio, A., and Piégay, H., 1998. A new methodology for the assessment of large woody debris accumulations on highly modified rivers (example of two French piedmont rivers). *Regul. Rivers Res. Manage*., 14(6): 467–483.

[131] Tsujimoto, T., 1999. Fluvial processes in streams with vegetation, *J. Hydraul. Res*. 37(6): 789–803.

[132] Van De Wiel, M., and Darby, S.E., 2004. Numerical modelling of bed topography and bankerosion along tree- lined meandering rivers. In Riparian Vegetation and Fluvial Geomorphology; Bennet, S., Simon, A.; Eds; AGU: Washington, WA, USA.

[133] van der Nat, D., Tockner, K., Edwards, P.J., and Ward, J.V., 2003. Large wood dynamics of complex alpine river floodplains. *J. North Am. Benthol. Soc*. 22(1): 35–50.

[134] van Dijk, W.M., Teske, R., van de Lageweg, W.I., and Kleinhans, M.G., 2013. Effects of vegetation distribution on experimental river channel dynamics. *Water Resour. Res*. 49: 7558–7574, doi:10.1002/2013WR013574.

[135] Vargas-Luna, A., Crosato, A., and Uijttewaal, W., 2015. Effects of vegetation on flow and sediment transport: Comparative analyses and validation of predicting models. *Earth Surf. Processes Landforms*. 40: 157–176.

[136] Wallerstein, N.P., Alonso, C.V., Bennett, S.J., and Thorne, C.R., 2001. Distorted Froude-scaled flume analysis of large woody debris. *Earth Surf. Processes Landforms*. 26: 1265–1283.

[137] Walter RC, Merritts Dj. 2008. Natural streams and the legacy of water-powered mills. *Science* 319(5861):299-304. doi: 10.1126/science.1151716.

[138] Water Resources Management Information System. Ministry of Land, Infrastructure and Transport in Korea. Available online: http://www.wamis.go.kr/ (accessed on 21 February 2018).

[139] Welber, M., Bertoldi, W., and Tubino, M. (2013), Wood dispersal in braided streams: Results from physical modeling. *Water Resour. Res*. 49, 7388–7400, doi:10.1002/2013WR014046

[140] Williams, G.P.; Wolman, M.G. Downstream Effects of Dams on Alluvial Rivers; United States Government Printing Office: Washington, WA, USA, 1984, pp. 1–83.

[141] Wohl E, Goode JR. 2008. Wood dynamics in headwater streams of the Colorado Rocky Mountains. *Water Resour. Res*. 44. http://dx.doi.org/10.1029/2007WR006522.

[142] Wolfert, H.P. Geomorphological Change and River Rehabilitation, Ph.D. Thesis, University Utrecht, Utrecht, The Netherlands, 2001.

[143] Woo, H., Chung, S., Cho, H., A Field Survey and Analysis of Ground Water Level and Soil Moisture in A Riparian Vegetation Zone. *J. Korea Water Resour. Associ*. 44(10), 797-807, 2011.

[144] Wu, W.; Shields, F.D., Jr.; Bennet, S.J.; Wang, S.S.Y. A depth averaged two dimensional model for flow, sediment transport, and bed topography in curved channels with riparian vegetation. *Water Resour. Res*. 2005, 41, W03015, doi:10.1029/2004WR003730.

[145] Wyzga B, Zawiejska J. 2005. Wood storage in a wide mountain river: case study of the Czarny Dunajec, Polish Carpathians Wyżga B, Zawiejska J. *Earth Surf. Processes Landforms*. 30(12): 1475-1494.

[146] Yabe, T., Ishikawa, T., A numerical Cubic-Interpolated Pseudoparticle (CIP) method without time splitting technique for hyperbolic equations, *J. the Physical Society of Japan*. 59(7), 2301-2304, 1990.

[147] Ye, F., Chen, Q., Blanckaert, K., and Ma, J., 2013. Riparian vegetation dynamics: Insight provided by a process-based model, a statistical model and field data. *Ecohydrology*. 6: 567–585.